POLITECNICO DI TORINO

Master's Degree
in Nanotechnologies for ICTs

Master's Degree Thesis

Spatiotemporal Study of Electronic and Thermal Transport in Low-Dimensional Semiconductors Using Transient Reflection Microscopy

Supervisors
Dr. James K. Utterback
Prof. Francesco Bertazzi

Candidate
Francesco De Bellis

Academic Year 2024-2025

Table of contents

Thesis overview

This manuscript aims to show how stroboSCAT microscopy can be used as a high-spatiotemporal resolution and label-free tool to observe electronic and thermal energy transport in the next generation of optoelectronic materials research.

With this goal in mind, the thesis is structured in four parts: an introduction to semiconductor theory and nanomaterials, state-of-the-art transient microscopy techniques and an introduction to stroboSCAT, its application to colloidal nanocrystal films (NCs), and its application to two-dimensional transition metal dichalcogenides (TMDs).

Chapter 1 provides the motivation and foundation for studying energy transport in nanomaterials. The chapter contrasts bulk semiconductors like silicon—efficient but limited by scaling, indirect band gaps and processing costs—with nanocrystals (NCs) and 2D materials (TMDCs), which are cheaper and easier to process, offer tunable optical properties but come with challenges due to reduced dimensionality and disorder.
The chapter provides some basics of semiconductor physics, followed by an introduction to the unique features of quantum materials. We explain how a central issue is distinguishing electronic and thermal transport in pump–probe microscopy.

Chapter 2 will lay out the theoretical foundations and implementation of stroboSCAT. We will revisit the principles of optical interference and scattering, explaining how small refractive index perturbations–due to photoexcited charge carriers or heat–can be translated into measurable changes in probe intensity. We then describe in detail the custom stroboSCAT experimental setup used for these investigations together with its spectrally-resolved variant. We demonstrate how stroboSCAT can be tuned to sense local diffusivity and relaxation of charges, excitons and heat through some representative experiments. We show examples of how the experimental data are preprocessed, analysed and fitted.

In Chapter 3, we apply stroboSCAT to colloidal nanocrystal (NC) films. The main challenge here is learning how to disentangle electronic and thermal contributions in pump-probe energy transport measurements. Specifically, we leverage wavelength-dependent, fluence-dependent, and thickness-dependent stroboSCAT experiments (supported by AFM profiling) to distinguish each. To this purpose, there will be a small overview over CdSe and PbS NC film preparation and the theoretical models of energy transport in disordered NC solids will be discussed. With the same goal, transient pump-probe spectroscopy and temperature-dependent steady-state measurements are used to cross-check the results. Synthetic data are then used furtherly validate the analysis. The result of this work is the demonstration of how both charge carrier and transient heating relaxation and transport can be measured with one technique.

Chapter 4 extends stroboSCAT investigations to the study of energy transport in two-dimensional transition metal dichalcogenides (TMDs) such as WSe_2. It begins by introducing TMDCs for optoelectronics, highlighting how their tunable band gaps and atomically thin nature makes them promising for light-emitting devices and photodetectors. We first discuss TMDCs crystal structure, chemistry and preparation methods (mechanical exfoliation, viscoelastic transfer, annealing), along with their thickness-dependent band structure and excitonic properties. Particular attention is given to the indirect-to-direct band gap transition in monolayers and the role of the different excitonic resonances for transport and spectroscopy. The chapter then focuses on thermal transport: stroboSCAT experiments reveal that above-band gap or high-fluence excitation induces heat-dominated signals, which is confirmed from COMSOL finite element simulations. The thickness dependence of relaxation and the role of substrate interactions are analyzed , showing how lattice heating and Auger-mediated recombination processes dominate under certain conditions. Finally, electronic transport is addressed under low-fluence, near-gap conditions, where we assume excitons and free carriers to be dominating. Probe wavelength-dependent measurements reveal diffusivities consistent with electronic carriers. This thesis aims to illustrate the advantages of using spatiotemporally resolved transient reflectance microscopy to probe energy carrier dynamics and kinetics in two different low-dimensional nanostructures. The idea behind this work is to show the energy carrier transport properties of both NCs and 2D materials through a technique capable of resolving with high resolution both charge and thermal properties. The comprehension of the energy transport mechanisms at the nanoscale are of fundamental interest in the optimization of NC/TMDs based optoelectronic devices.

Chapter 1

Introduction

1.1 Background and Motivation: Nanomaterials in Optoelectronics

Bulk semiconductors are three-dimensional (3D) macroscopic pieces of a semiconductor material, used in a variety of optoelectronic devices such as transistors, sensors, light emitting diodes, solar cells and quantum devices. Conventional semiconductors are mostly represented by silicon, and it has propelled the development of modern optoelectronic devices and nanoelectronics for decades. Even if the efficiency of silicon-based optoelectronic devices has greatly improved due to the growing knowledge of this material, the escalation of device miniaturization and the increasing performance demand is pushing research towards its fundamental physical limits.

3D bulk semiconductors are naturally abundant in nature and they are cheap, but their application in optoelectronics and electronics requires a high level of control over structure, doping and defects This makes their processing intensive, for example with high temperatures and huge energetic consumption required for high purification. The increase in environmental concerns and their yearly growing demand, represents a serious limiting factor to the viability of these technologies [1].

In addition to that, Silicon's indirect band gap makes it inefficient for light emission and limited for detection, which further complicates its use in photonic devices. While it is the most widely used semiconductor for photovoltaics, progress for single-junction cells has nearly stagnated. Emerging materials such as organic polymers, perovskites or nanocrystals offer new prospects as they tend to exhibit higher absorption coefficients and usually direct bandgap, allowing thinner films in active layers[2].

Traditional bulk semiconductors usually have good charge carrier mobility, yet the advances in optoelectronic device technology is pushing them towards their physical scaling limits. As these materials are miniaturized to nanometer thicknesses, dangling bonds, surface states and interfacial defects contribute to the degradation of carrier mobility. Additionally, the transport and recombination rates of photoexcited carriers affect device operation speed and efficiency. At such reduced dimensions, thermal management also becomes a significant challenge.

With the advancements in colloidal synthesis techniques, exfoliation of layer materials, and the adoption of top-down fabrication methods such as Molecular Beam Epitaxy (MBE) and Chemical Vapor Deposition (CVD), nanomaterials have become a promising alternative to overcoming the challenges of traditional bulk semiconductors. Nanomaterials offer opportunities for precise tuning over their optoelectronic properties, including the energetic and spatial disorder, redefining the device capabilities.

Nanomaterials such as colloidal semiconductor nanocrystals and 2D materials, show unique electronic, optical and thermal properties compared to their bulk semiconductor counterparts which makes them appealing also in fundamental research. Due to their low-dimensionality and high surface-to-volume ratio, they tend to emphasize physical phenomena that would be hard if not impossible to observe in other conventional systems. The mechanisms governing charge transport and heat dissipation operate differently from bulk materials and the idea is to leverage them to make the next generation of optoelectronic devices. Nanomaterials in fact represent a promising opportunity for cost-effective, environment friendly and high performance technologies.

The adoption of nanomaterials in optoelectronics devices, undoubtedly comes with its own challenges with the comprehension of electronic and thermal transport mechanisms at the nanoscale being one of them. While it is true that these mechanisms can be leveraged for performance enhancements, they also introduce a variety of effects such as performance instability and degradation that are more pronounced than in bulk materials and can be detrimental.

Investigating the underlying principles of photogeneration, charge transport and charge collection is essential for efficiency improvement. Also interfaces between different materials and local defects require careful control to optimize device performance.

The objective of this thesis is to explore the properties of selected nanomaterials to understand their energy transport mechanisms and determine the factors that significantly influence their behaviour. An emphasis is placed on measurements that give access to both charge carriers and transient heating that result from photoexcitation.

1.2 Nanomaterials in Optoelectronics

1.2.1 The Basics of Semiconductors Physics

All solid state materials are characterized by an *energy gap* E_g, also referred to as *bandgap*, which represents the energy difference between the top of the highest filled bands–the valence band–and the bottom of the lowest empty bands–the conduction band. At T = 0 (absolute zero), a solid with a finite energy gap between the valence and conduction bands will be insulating if it has all its valence band states filled and conduction band states empty—ideally it also has no mid-gap states due to impurities [3].

Based on the magnitude of this energy gap we can define **insulators**, **conductors** and **semiconductors.** The first class of materials has a high bandgap (typically over 4 eV) which separates its filled valence band from the empty conduction band. This means insulators do not conduct any current and even at higher temperatures the probability of thermally exciting electrons from valence band to conduction band is extremely low.

Conducting materials like metals have overlapping valence and conduction bands, so there is no bandgap—there are thermal carriers even at T = 0.

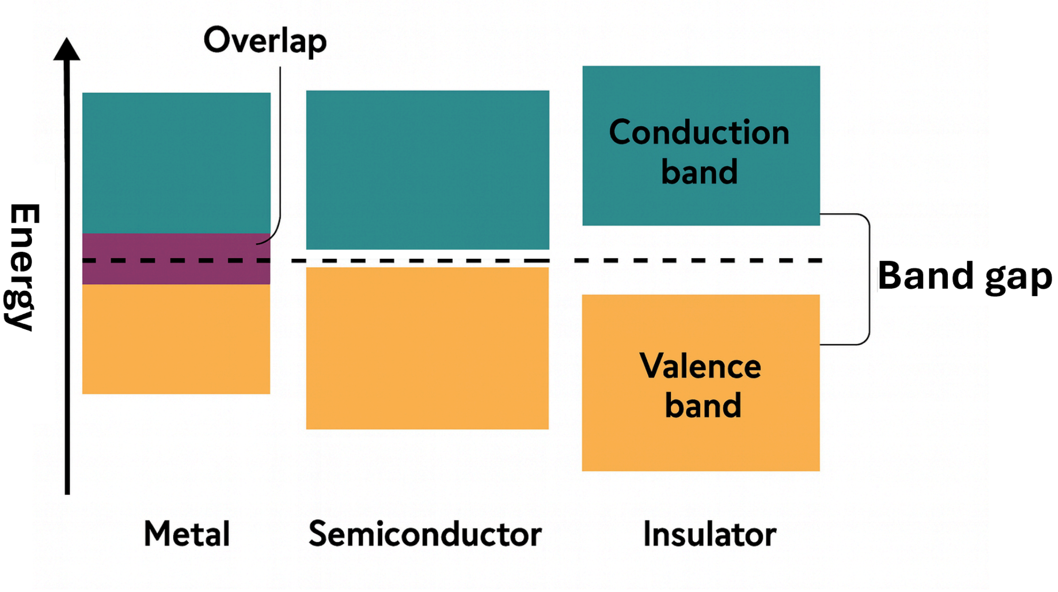

Figure 1. Schematic comparison of the energy band diagrams of metals, semiconductors and insulators

In this thesis we are focusing our attention on the semiconductor class of materials, which lies in the middle. Semiconductors have a fairly small bandgap, usually smaller than 3 eV. At $T = 0$ they behave as insulators but as the temperature increases they start behaving like conductors with an electrical conductivity that increases with the temperature, distinguishing them from metals.

Photoconductivity is a consequence of semiconductors' small bandgap. Across this thesis we will see that visible light can be used to excite charges across the gap into the conduction band, making the material behave like a conductor.

The bandgap is one of the most important sources of optical information of a material. If the semiconductor has a “direct bandgap”, the top of valence band and bottom of conduction band occur at the same crystal momentum k in the $E(k)$ diagram. If an incident photon carries the same energy as the direct band gap of the semiconductor, its absorption manifests as a sharp absorption peak. If the transition is “indirect” — as in the case of silicon— a phonon participates to the transition, providing an extra momentum contribution $\hbar\omega(k)$ so that the transition can happen even if the absorbed photon carries smaller energy than the gap

In typical bulk semiconductors the energy gaps are linearly dependent on temperature at room temperature and have quadratic dependence at low temperature as stated by Varshni empirical relation. Usually this temperature dependence is associated with thermal expansion–acting on the periodic potential experienced by electrons, thus on the band structure–and to the effect of lattice vibrations on the band structure and energy gap [3]. Both types of semiconductors are schematically represented in Fig 2.

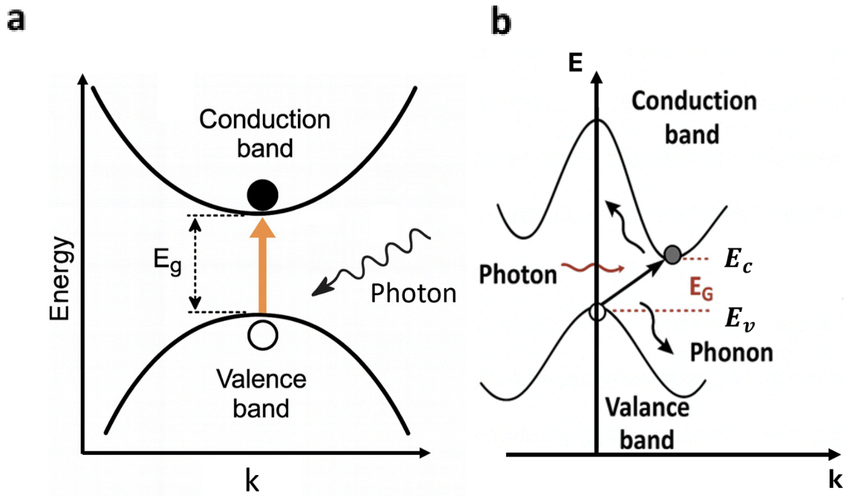

Figure 2. Energy band diagrams schematics under photoexcitation. (a) Direct band gap. (b) Indirect band gap

The electronic band structure is composed by all allowed energies as a function of the crystal wavevector *k*. Typically these band diagrams have labeled symmetry points which represent k-points in the reciprocal space, mapped to specific points in the real-space primitive cell.

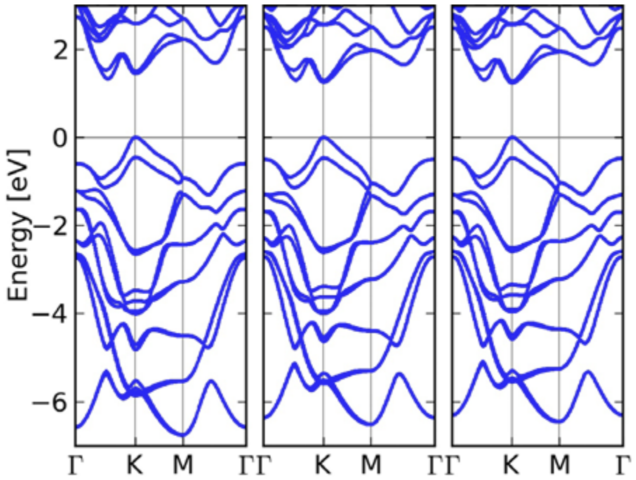

Figure 3. Computed band structure of a WSe_2 monolayer [4]

The electrons in the conduction bands of a semiconductor can be seen as quasiparticles moving in a free space with a modified mass called *effective mass (m*)*, which is related to the electrons' interaction with the surrounding.

One way to effectively change the effective mass of charge carriers is through the *doping* of the semiconductor. When the introduced impurities supply electrons to the charge density of the semiconductor, it is called *donor.* If the impurity contributes with additional holes electrons, it is called an acceptor. The former are called n-doped semiconductors, the latter are p-doped semiconductors. Free electrons which move through an n-doped semiconductor experience an effective mass given by the electrostatic interactions with the donor atoms, which have lost their electrons becoming holes [3].

The donor impurities will modify the electronic band structure of the semiconductor, by introducing additional electronic levels right below the bottom of the lowest conduction bands. The acceptor impurities will manifest through additional allowed energy levels right above the maximum valence band. Impurities are very important as they introduce new scattering centers and shallow states. They are sources of free carriers and allow electronic transitions over a smaller energy gap, due to the additional allowed states.

Every time an electronic transition is stimulated through the photon absorption the resulting excitation products–as free charges, excitons, polarons, and heat–will be transported through the material.

1.2.2 Nanocrystal Semiconductors

Colloidal nanocrystals (NCs) are a class of semiconductor nanostructures that allow a more effective manipulation of light-matter interactions. We can define these nanoparticles as fractions of bulk semiconductors, with sizes typically ranging from few to tens of nanometers in diameter, suspended in a colloidal solution. They have been studied for decades because of their size-dependent optical, electronic and thermal properties [5]. NCs can be prepared by epitaxy or sputtering, but chemical synthesis allows the finest control of their shape and sizes, offering ways to engineer their bandgap. QDs can be prepared so that they can emit and absorb light at over a wide range of frequencies.

Nanocrystals show charge quantum confinement due to their small sizes, giving rise to discrete electronic energy levels instead of continuous bands of conventional bulk semiconductors [6]. Excitons are the typically photogenerated electronic carriers in NCs, which are bound electron-hole pairs. Unlike bulk semiconductors where excitons are bound Coulombically, in NCs if the two charge carriers are present then they are spatially forced to overlap.

NCs exhibit strong light absorption due to quantum confinement. They can achieve very high photoluminescence quantum yields and serve as efficient sources of excitons and charge carriers under optical excitation [7].

Organic ligands are bonded to the surface of the nanocrystals to keep them stable in colloidal solution and are an important part of their synthesis mechanism. They can also be changed post-synthesis for improving the electronic coupling to charge acceptors or the electrical conductivity of NC films.

In the experiments discussed through the next sections, the nanocrystal-based solution is spin coated to form thin films on glass substrates, constituting a positionally disordered system. In different preparation conditions, NCs can self-assemble into ordered crystal structures called “superlattices” as shown in Fig. 4a, where the electronic coupling between NCs is much stronger. In chapter 3 of this thesis we will deal only with NC colloidal film, which are typically disordered (example shown in Fig. 4b)

The charge transport in such films is fundamentally different from the band-like transport observed in bulk semiconductors, as NCs behave like quantum confined systems with localized charge carriers and discrete locations where the charge carriers can be found. The charges move through the nanocrystal film hopping from a NC to its neighbors, with the organic ligands acting as a tunneling barrier [8]. Their transport dynamics and kinetics have been deeply investigated through time-resolved photoluminescence and kinetic Monte Carlo simulations.

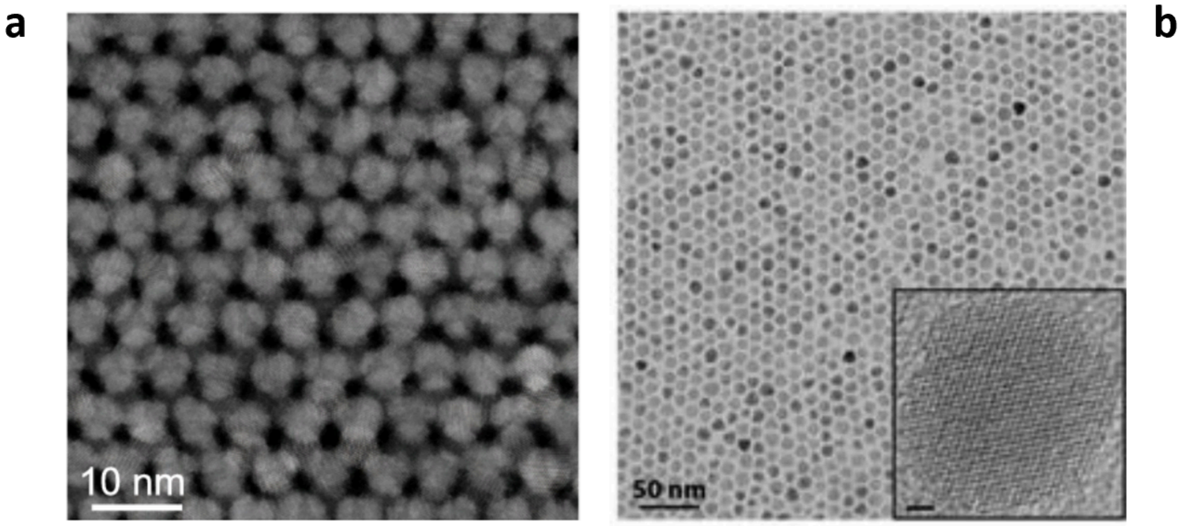

Figure 4. (a) Example of PbS monolayer superlattice [9]. (b) Example of CdSe nanocrystal film; inset is a TEM image of a single nanocrystal [10]

1.2.3 2D Semiconductors

Transition Metal Dichalcogenides (TMDs) like WSe_2 and MoS_2 were first isolated around 15 years ago by Heinz and coworkers [11]. TMDs are layered structures composed of 2D sheets kept together by weak van der Waals interactions.

Each structure is formed by transition metal atoms (i.e., tungsten or molybdenum atoms), sandwiched between two chalcogen layers (i.e., selenium or sulfur atoms), as shown in Figure 5. Like the prototypical 2D material graphene, TMDs can be exfoliated to make atomically thin layers [6].

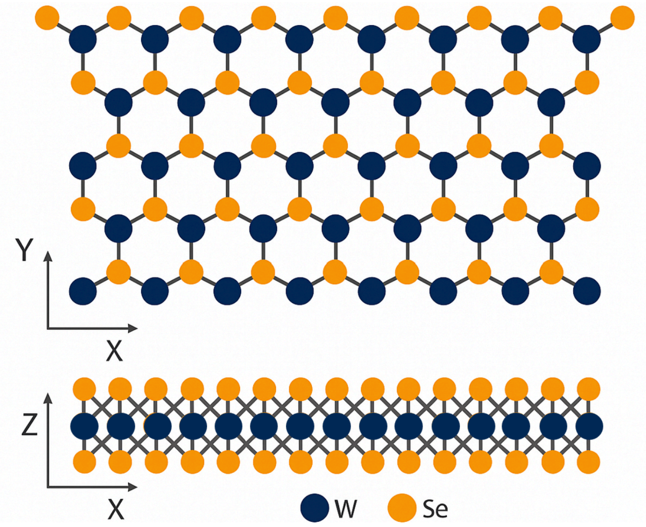

Figure 5. Crystal structure representation of a WSe_2 monolayer. Tungsten atoms in blue, selenium atoms in yellow.

Since the discovery of graphene in 2004[12], 2D material-based optoelectronic devices have shown great performance improvements in comparison to traditional bulk semiconductor materials. This is partly due to their high photodetection performance and carrier mobilities. Even though it is widely used in optoelectronic devices, graphene's big disadvantage for many photonic applications is its zero bandgap.

TMDs instead, do not suffer from this limitation as their band gap ranges between 1 eV to beyond 2.5 eV. Due to their unique physical properties and tunability they offer great potential in light-emitting devices, lasers and optical detectors. Even TMDs valley degeneracy is investigated for optical computing applications [13].

When exfoliated and reduced to atomic thicknesses these materials show enhanced Coulomb interactions due to the increased quantum confinement, giving large binding energies in the range of hundred meV. For this reason, excitons usually dominate the optical and optoelectronic properties of TMDs even at room temperature[14]. The strong light-matter interactions and rich population of excitonic species make 2D materials promising candidates for next-generation optoelectronics devices.

Depending on the exfoliation process adopted, TMD-based devices can be fabricated using flakes of thicknesses spanning from monolayers–between 0.5 and 1.5 nm–to a few layers–tens of nm thick–and bulk. The electronic band structure is severely affected by the thickness, which means that some of the optical properties of TMDs can be tuned by choosing flakes of adequate thickness, similar to size tunability. Strikingly, with decreasing thicknesses these materials undergo a transition from indirect to direct gap, allowing strong photoluminescence and light absorption in the case of monolayers[15].

These materials show fascinating properties which also bring unique challenges when it comes to the understanding of how energy carriers flow after photoexcitation. Both NCs and 2D materials are very sensitive to external perturbations–surface-bound species, mechanical strain and domain interfaces. In NC films the energetic and structural disorder strongly impact the charge hopping and thermal dissipation[16]. In TMDs the transport behaviour can be heavily affected by substrate interactions, interlayer coupling, surface trapping and defect scattering. Partly due to the high quantum confinement, they also exhibit non-radiative decay channels.

When nanomaterials get photoexcited through optical injection, the carriers can rapidly thermalize causing lattice heating or recombine in several ways. In the following sections we will explore how important and challenging it can be distinguishing the thermal and electronic signatures when doing optical spectroscopy on nanocrystals and 2D materials.

1.2.4 Challenges in Studying Energy Transport in Nanomaterials

A key challenge in the design of high-performance optoelectronic devices based on nanomaterial semiconductors is understanding how energy carriers move through them in different environment conditions and different excitations. Energy carrier transport is a key process for the efficiency of a device.

The absorption of the incident light leads to the formation of various excitation products–electrons, holes, excitons, heat–each with peculiar transport dynamics and relaxation mechanisms. Electrons and holes can undergo recombination, they can undergo various nonradiative relaxation pathways such as trapping at defect states, Auger recombination, and transition to electronic states other than the band edge. These processes compete with charge carrier extraction at electrodes in optoelectronic devices.

An important challenge in the study of these materials comes from structural and energetic disorder. NC films and organic semiconductors are inherently heterogeneous and disordered as nanoparticles can show size and shape polydispersity[17]. Impurities, defects and grain boundaries in the NC films all contribute to changing the efficiency, timescales and length scales of energy carrier transport.

In 2D materials, disorder can originate from lattice strain, grain boundaries, chemical doping, interlayer twisting, or substrate-induced perturbations [6]. Probing each type of excited energy carrier moving through the semiconductor can be challenging; while signals in pump–probe measurements are traditionally interpreted as originating from charge carrier populations, there is increasing recognition that photoinduced heating can also generate spectral features. As a consequence, disentangling all these contributions and assigning the signal to a specific energy carrier can be quite hard to do.

In NCs and 2D materials, the above processes may happen over short timescales and lengths. To spatiotemporally capture this complex phenomena, both time and space resolutions must be pushed to the limits. To accurately interpret these relaxation processes, experimental techniques must be performed at various fluences, material thicknesses and temperatures. In this thesis we will be tackling these challenges through an approach that bridges spatial and temporal domains still being sensitive to a wide range of physical phenomena.

Chapter 2

Theory and Working Principle of Stroboscopic Optical Scattering Microscopy (stroboSCAT)

In section 2.1 of this second chapter on stroboscopic scattering optical microscopy, we will provide some theoretical background on the experimental technique which will be adopted across the manuscript. Specifically, it will contain a brief discussion about the fundamental light-matter interactions which optical scattering microscopy is funded on; we will also focus on systems on multiple nanoparticles acting as light scatterers.

In section 2.2 interferometric scattering microscopy–the steady state predecessor of strobosCAT–will be introduced to the reader and some general basics on optical microscopy will be provided. In section 2.4 and 2.5 of this chapter, we will discuss the optical properties of materials and specifically the complex refractive index will be introduced. The idea is to provide a theoretical approach to explain how stroboSCAT microscopy can be sensitive to changes of refractive index when the material is in an excited state.

From section 2.6 to 2.8 we will provide a detailed description of the experimental setup adopted for the pump–probe experiments that are the basis of this thesis. Details will be provided on the optical layout of the microscope, the laser sources, the electronic control systems, the imaging-based detection as well as the spectrometer.
We will describe how stroboSCAT allows for local microscopic diffusivity and lifetime measurements of the different photoexcited energy carriers in their respective timescales and length scales.

The last section of this chapter will also describe the analysis of the acquired experimental data. I consider this final section as a toolkit useful to those who want to do spatiotemporal transient reflection microscopy. We will discuss data pre-processing, fitting models, python code overview and error management workflows.

2.1 Light Scattering from Small Particles

Natural phenomena like rainbows at the end of a rainfall can be explained as macroscopic manifestations of scattering and absorption of light. Consider scattering and absorption by individual or aggregated small particles. In first approximation, the tools provided by classical electromagnetic theory and linear optics are sufficient for our purpose. Scattering and absorption are due to the presence of heterogeneity in every system, regardless of the scale. At the origin of these optical phenomena there's an electromagnetic wave interacting with the electrons and protons that matter is made of.

If a system–which could be solid, liquid or made by just a single atom–is irradiated with an incident electromagnetic wave, those electric charges will oscillate with the electric field due to the incident light. The oscillating charges emit electromagnetic radiation, thus behaving as secondary sources of radiation themselves. The superposition of the fields by each charge constitutes the secondary radiation, the scattered light (Fig. 7).

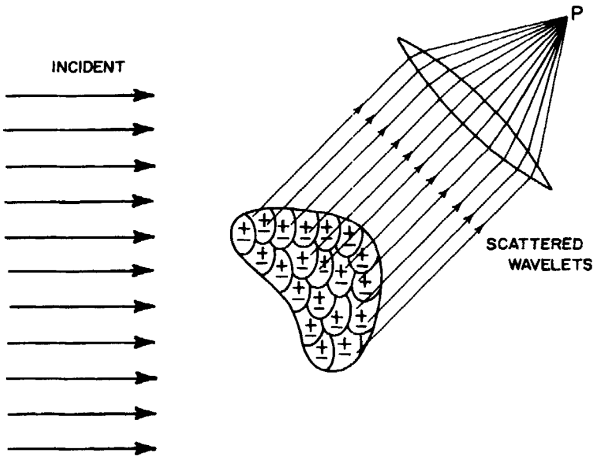

Figure 6. Schematic representation of light scattering on a small particle [18]

In this work we study systems of excited energy carriers which behave as collections of particles, each acting like a secondary light emitter. Due to its complexity, physicists usually deal with this electromagnetic problem as if it is a many-body problem where every particle is subject to the incident field but also to the other particles' secondary fields. If the particles in the material are small and close enough, the secondary waves can all be approximately overlapping each other and the incident wave. This produces a refracted *wave* with a propagation velocity *c/n*, where *c* is the speed of light in vacuum and *n* is the refractive index.

The *n* index, which we will discuss more on later, stresses the idea that we always deal with a macroscopic picture of light scattering problems. The index depends on the number of molecules per unit volume and their polarizability. This is very important, because optically smooth samples still scatter light due to density fluctuations. Scattering is affected by these time-related density fluctuations, making Snell's law an approximation.

We ignore scattering fluctuations when we assume that the heterogeneities in the material are small compared with the wavelength of the incident light.

Another aspect that complicates the picture is that light scattering can be *elastic* or *inelastic*. In inelastic scattering a fraction of the energy carried by the incident light beam is absorbed by the scatterers and re-emitted at a different frequency or converted to heat, which is the case of *Raman scattering*. This doesn't happen in elastic scattering, which is also called *Rayleigh scattering* .

In the classical "*extinction theorem*" or "*Ewald-Oseen theorem*" if the secondary emissions add up constructively, the new field cancels out the incident wave in the medium and a new wave propagates forward through the material. On the other hand, if they interfere destructively with the incident light inside the material, the forward-propagating wave will lose energy passing through the medium, contributing to the overall absorption of the incident light. The Lambert-Beer law below, describes the light intensity (or irradiance) as exponentially attenuated through the semiconductor as a function of the absorption coefficient α.

$$I = I_0 exp(- \ \alpha L) \tag{1.0}$$

where I_0 is the intensity of the incident radiation, L is the penetration depth into the material.

There are several models used to solve the problem of scattering and absorption in collections of small particles. Gustav Mie provided the only one which exactly solves Maxwell's equations and its boundary conditions for small spheres of arbitrary radius and refractive index.

Scattering happens because of the particle-medium dielectric mismatch, so for a particle to be visible we need to have the ratio $n_{part} / n_{medium} \neq 1$, where n_{medium} and n_{part} are the refractive indexes of the medium and the particle respectively. Without index contrast, no scattering occurs.

Mie Theory is used when the particle size approaches the wavelength of the incident wave ($d \sim \lambda$). The theoretical model allows precise calculation of scattering intensity, extinction, backscattering and absorption cross sections based on particle size, wavelength and beam polarization.

This approach works well when we study spheres and it provides an exact result, but it can be computationally demanding. In addition, Mie Theory holds if the number of scatterers is sufficiently small and their separation is large enough. We can use Rayleigh scattering regime theory when the size of the particles is much smaller than the wavelength of the incident light $d << \lambda$. In the case of pump–probe microscopy, the pump light pulse induces small permittivity perturbations due to photoexcited charge and heat distributions. Mie theory may be needed for a complete description of the resulting light scattering, but we can use the framework of Rayleigh scattering as an approximation to gain some intuition for the problem.

In this limit the scattered intensity I_s is given below:

$$I_s = I_0 \frac{8\pi^4 N a^6}{\lambda^4 r^2} \left| \frac{m^2 - 1}{m^2 + 2} \right|^2 (1 + cos^2 \theta)$$

(1.1)

where I_0 is the incident intensity, N indicates the number of scattering particles, r is the distance between the scatterer and the observation point, and m is the ratio of the particle and medium refractive indices. What the equation 1.1 tells us, is that in Rayleigh regime each particle acts as a small dipole whose field intensity profile follows a $cos^2 \theta$ relation. Averaging the expression (1.1) over θ we can get the Rayleigh scattering and absorption cross sections:

$$\sigma_s = \frac{8}{3} \left(\frac{2\pi a n_{med}}{\lambda} \right) \frac{a^6}{\lambda^4} \left| \frac{\epsilon_{part} - \epsilon_{med}}{\epsilon_{part} + 2\epsilon_{med}} \right|^2$$

(1.2)

$$\sigma_a = \frac{8a\pi n_{med}}{\lambda} Im\left[\frac{\epsilon_{part} - \epsilon_{med}}{\epsilon_{part} + 2\epsilon_{med}}\right]$$

(1.3)

where ϵ_{part} and ϵ_{med} the permittivities of the particle and medium. These cross sections are used to predict and interpret how small particles or fluctuations in the refractive index scatter light. Rayleigh scattering model predicts a symmetric angular distribution of the intensity of the scattered radiation. In contrast, Mie scattering theory predicts that larger particles produce angular anisotropies, characterized by forward scattering lobe and reduced backscattering, effects that the Rayleigh model cannot capture.

2.2 Optical Properties of Materials: From Polarizability to the Complex Refractive Index

This section introduces the optical constants which play a role in light-matter interaction phenomena. Our perception of reality is closely related to light-matter interactions. stroboSCAT is used to detect transient changes in the optical properties of a material, so we review the classical principles of light-matter interaction.

As mentioned in the previous section, when an incident electromagnetic wave propagates through a dielectric medium, the oscillating electric field E forces an oscillation in each atom or molecule. This response is defined as a dipole moment , which is defined as follows:

$$p = \alpha(\omega)E$$

(1.4)

where α is the microscopic *polarizability,* which depends on the class of materials. E is the electric field causing it. In a solid material, if the field is strong enough, it can produce a macroscopic polarization P (equation 1.5), which represents the dipole moment per unit volume as shown below:

$$P = N\alpha(\omega)E = \epsilon_o\chi_e E$$

(1.5)

Here χ_e is the susceptibility. The total electric field is due to the free charges already present in the material, and to the polarization itself. Thus, a new quantity called *electric displacement D* , is introduced:

$$D = \epsilon_o E + P = \epsilon_0(1 + \chi)E = \epsilon E$$

(1.6)

where ϵ is a new proportionality constant which divided by ϵ_0 gives the relative permittivity $\epsilon_r = \epsilon/\epsilon_0$. Maxwell's equation gives the velocity of light travelling through a media as:

$$v = \frac{1}{\sqrt{\epsilon\mu}} = \frac{c}{n}$$

(1.7)

where *n* is the refractive index of the material, μ_0 is the magnetic permeability and *c* is the speed of light in vacuum $c = (\epsilon_0\mu_0)^{-1/2} = 3 \cdot 10^8\, m/s$. The refractive index quantifies how an electromagnetic wave interacts with the medium and travels through it. In general the denser the material, the higher will be its refractive index due to the high number of interactions between the radiation and the charges in the medium. It is mostly used as a set of complex optical parameters as shown in equation 1.8. Light-medium interactions will change depending on the frequency of the incident field which is forcing the oscillation.

$$\tilde{n}(\omega) = n(\omega) + ik(\omega) = \sqrt{\epsilon_r}$$

(1.8)

The values of *n* and *k*, which are reformulated in equations 1.9 and 2.0, determine the phase velocity and attenuation of the electromagnetic wave.

$$n = \sqrt{\frac{\epsilon' + \sqrt{\epsilon'^2 + \epsilon''^2}}{2}}$$

(1.9)

$$k = \sqrt{\frac{\sqrt{\epsilon'^2 + \epsilon''^2} - \epsilon'}{2}}$$

(2.0)

These two components of the refractive index are related by Kramers-Kronig relations, which ensure that absorption features in the $k(\omega)$ spectrum are always correlated to dispersive features in $n(\omega)$.

Another set of optical parameters often used to describe microscopic behaviour of light in media, is the *complex dielectric function*:

$$\epsilon = \epsilon' + i\epsilon''$$

(2.1)

These dielectric functions directly relate to *n* and *k* for small-particle scattering.

A material's optical response to the electromagnetic radiation is not simple to treat analytically, especially because the polarization induces many secondary sources active at different frequencies. The first theoretical description of materials optical properties was provided by Lorentz. He treated each bound electron or ion as a damped harmonic oscillator driven by an external field (shown in Fig. 8). Analogously a collection of identical and independent particles, could be treated classically as a simple isotropic harmonic oscillator to define the optical properties of the materials.

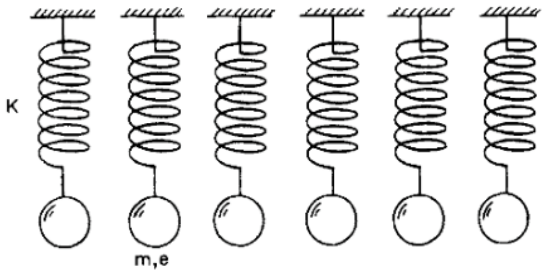

Figure 7. Schematic representation of Lorentz harmonic oscillator model [19]

If compared to the quantum-mechanical interpretation of light-matter interactions, Lorentz's theory is more intuitive. Though simpler, it still allows quantitative fit of the experimental data just as those of quantum mechanical treatments.

$$m\frac{d^2x}{dt^2} + m\gamma\frac{dx}{dt} + m\omega_0^{\ 2}x = -qE_0e^{-i\omega t}$$

(2.2)

Relation 2.2 describes the dynamics of a simple oscillator of mass m and charge e, x represents the displacement from the equilibrium position, γ is a damping factor which limits the free oscillation of the mass, and $qE_0e^{-i\omega t}$ is the analytical expression of the incident radiation which drives the oscillation of the system.

As already mentioned, the classical and quantum models both manage to describe the physical phenomena, but the quantum mechanical interpretation of the harmonic oscillator model can be quite different from the classical one.

Due to the quantization of light, the interactions of photons with matter must be treated as discrete–each absorbed photon transfers a fixed energy and momentum. The material response–analogously to multiple oscillators–will be resonating when the incident wave has the proper frequency. Indeed, depending on the excitation frequency the polarization of the material causes multiple oscillators to be "active" at different frequencies. In quantum mechanical words, the absorbed photon will excite different quasiparticles and processes by giving away its energy and momentum. Through Lorentz model the total induced polarization in the material will be:

$$P = \frac{\omega_p^{\ 2}}{\omega_0^{\ 2} - \omega^2 - i\gamma\omega}\epsilon_0 E$$

(2.3)

where ω_p is called *plasma frequency*. From this, the dielectric function for the system of simple harmonic oscillators is:

$$\epsilon = 1 + \chi = 1 + \frac{\omega_p^2}{\omega_0^2 - \omega^2 - i\gamma\omega}$$

(2.4)

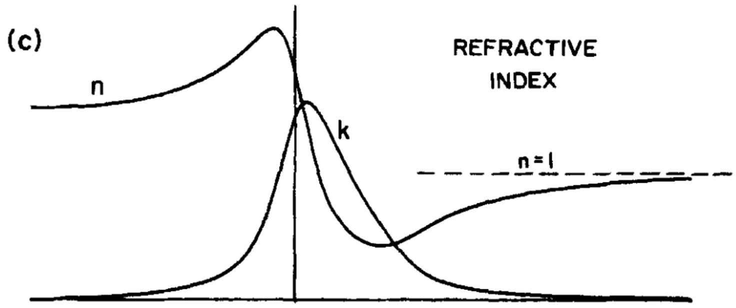

Figure 8. Characteristics of one-oscillator (Lorentz) model: real and imaginary part of the refractive index as a function of the frequency [19]

As shown by equation 2.4 and visualized in Fig. 9, at frequencies well below resonance ($\omega << \omega_0$), the polarization of the material is nearly in phase with the driving field, resulting in a small phase lag. As ω increases toward the natural resonance ω_0, the real part of the refractive index $n(\omega)$ rises–phenomena known as *normal dispersion*. Near ω_0, energy absorption (the damping) peaks, maximizing the imaginary component $k(\omega)$. For $\omega > \omega_0$, the induced polarization lags by more than 90°, and $n(\omega)$ falls with increasing frequency, which is the *anomalous dispersion.* [20]

2.3 Excited-State Phenomena in Semiconductors: Changes in the Refractive Index

When a bulk semiconductor is photoexcited, it can show several microscopic processes that alter its optical response, and its complex refractive index. In stroboSCAT, these pump-induced variations constitute the source of what is measured.

Some of these effects are respectively the *Pauli blocking*, *band filling* or *Burnstein-Moss effect.* [21] When electrons are promoted into the conduction band of the semiconductor upon photon absorption, they fill available states near the band edge preventing further charge excitation–due to spin selection stated by Pauli exclusion principle. This state blocking reduces the imaginary part of the permittivity near the band edge; if the lowest energy states in the conduction band are occupied, the energy required for charge excitation needs to be higher than the nominal band gap. If we assume parabolic bands, the interband absorption coefficient is given by:

$$\alpha_0(E) = 0 \ for \ E < E_g \tag{2.5}$$

$$\alpha_0(E) \propto \frac{1}{E}\sqrt{E - E_G}, \ \Delta k(\omega) < 0 \ for \ E \geq E_g \tag{2.6}$$

Table 16.

where $E = \hbar\omega$ and E_G is the bandgap energy.

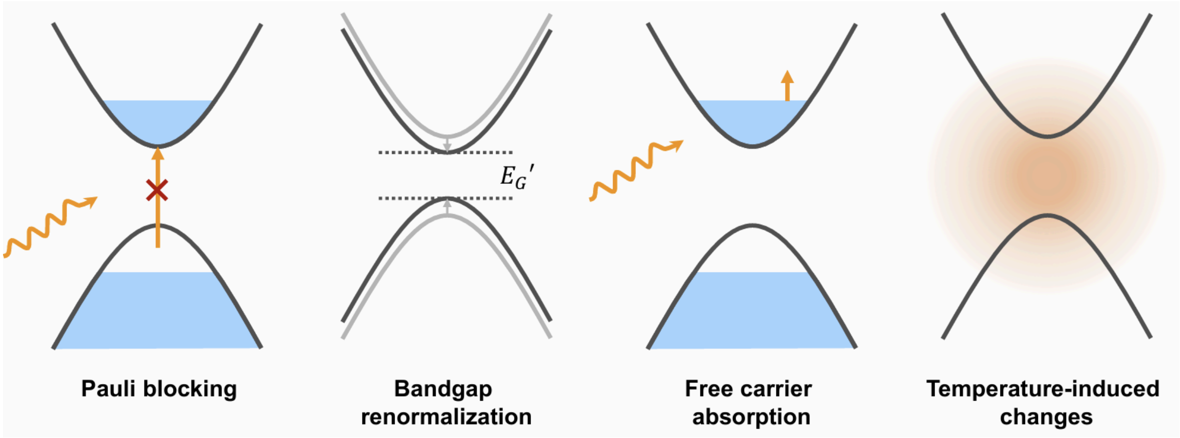

Figure 9. Cartoons showing the main excited state mechanisms influencing absorption: Pauli blocking, Band gap renormalization, free carrier absorption and temperature [22]

The second phenomena that can induce changes in the optical response of the material, is *bandgap renormalization.* When many electrons get injected into the conduction band of the semiconductor, their wave functions overlap because of the high density of carriers and repelling each other they reduce the overall Coulomb interactions with the holes in the valence band, screening the electrostatic interactions. The result of this process is the shrinkage of the bandgap. In terms of spectrum changes, or Lorentzian oscillator models, this process introduces a redshift in the resonance frequency of the material. In many cases the renormalization competes with Pauli blocking.

Another mechanism that can influence the optical properties of the material under excitation, is the free carrier absorption. It is due to intraband transitions of electrons in the conduction band (or holes in the valence band) that happen when incident photons are absorbed. This intraband processes are described through the classical Drude model, which states that the free carrier contribution to the permittivity of the material is:

$$\Delta\epsilon_D(\omega) = -\frac{\omega_p^2}{\omega^2 + i\gamma\omega}, \quad \omega_p^2 = \frac{N_{fc}e^2}{\epsilon_0 m^*} \tag{2.7}$$

where N_{fc} is the free carrier density, m^* is their effective mass and γ is the carrier-scattering rate. The real part of the complex permittivity is negative and produces a reduction in the refractive index; the imaginary part instead makes the absorption grow. In the Drude model the conducting electrons are treated as particles on a damped oscillator driven by the optical field. Because of the $1/\omega^2$ dependence, the free carrier absorption increases as the photon energy decreases, which produces a broad absorption spectrum while the effects of Pauli blocking and bandgap renormalization are largest approaching the bandgap.

The last process we want to take into account when studying photoexcitation of semiconductors is the temperature-induced effect. The change in temperature arises from non-radiative recombinations or lattice heating, and most of the semiconductors show a *thermo-optic coefficient* $dn/dT > 0$ due to many phenomena such as thermal expansion and electron-phonon interactions. The Varshni relation (equation 2.8) is used to empirically determine how much the bandgap changes upon temperature variation. [23]

$$E_G(T) = E_0 - \frac{\beta T^2}{T + \alpha} \tag{2.8}$$

where β and α are material specific fitting parameters. Thermal broadening due to electron-phonon coupling and resonance redshift due to lattice expansion are the most common temperature induced changes in the optical response of semiconductors.

By studying the optical properties of the semiconductor in its excited state, it is possible to get some insights on the mechanisms causing those changes. If we want to experimentally measure the changes in the absorption coefficient or in the refractive index, we can measure the change in reflectivity or transmittance through the sample (see equations 2.9 and 3.0).

$$\Delta R/R = (R_{ES} - R_{GS})/R_{GS}$$

(2.9)

$$\Delta T/T = (T_{ES} - T_{GS})/T_{GS}$$

(3.0)

where ES denotes excited state and GS denotes ground state. In section 2.1 we have given a picture of how light scattering on small particles can be used to describe light-matter interactions. The case of light interacting with solid materials is generally understood by means of light scattering theory, as the solid can be seen as a collection of very dense and close-packed scatterers. But also geometric optics–i.e *Fresnel equations*–can be used to describe with good precision the normal reflection of light at an interface under refractive index mismatch.

$$R = \left|\frac{\tilde{n}_i - \tilde{n}_t}{\tilde{n}_i + \tilde{n}_t}\right|^2 = \left(\frac{\tilde{n}_i - \tilde{n}_t}{\tilde{n}_i + \tilde{n}_t}\right)\left(\frac{\tilde{n}_i - \tilde{n}_t}{\tilde{n}_i + \tilde{n}_t}\right)^*$$

(3.1)

Where $\tilde{n}_i = n_i + ik_i$ and $\tilde{n}_t = n_t + ik_t$ are the transmission and reflection complex refractive indices. If a pump pulse induces a small change in *n* ($\Delta\tilde{n} << \tilde{n}$), the change in reflection coefficient can be approximated by:

$$\frac{\Delta R}{R} \simeq \frac{1}{R}\left[\left(\frac{\partial R}{\partial n_t}\right)\Delta n_t + \left(\frac{\partial R}{\partial k_t}\right)\Delta k_t\right]$$

(3.2)

A different approach is needed to measure the transient transmittance $\Delta T/T$ because Fresnel relations only provide the reflected and transmitted field amplitudes at the interfaces of the optical system. Instead, to take into account the attenuations and multiple reflections inside the medium one can use Lambert-Beer's law (equation 1.0) and measure the change in optical density. Or otherwise the transient absorption and transient reflection spectra can be obtained from Kramers-Kronig relations, but this is beyond the scope of this thesis.

2.4 From Diffraction Limit to Nanometer-scale Contrast

In the previous section we have introduced the mechanisms that can produce changes in the optical properties that will be studied across the whole manuscript. The resolution of energy transport not only requires a big effort in terms of ultrafast time scale resolution, but also the ability of distinguishing sub-micron features, thus a high *spatial resolution*.

Optical microscopy's spatial resolution is fundamentally limited by the *diffraction.* Abbe's diffraction limit sets the minimum resolvable distance at approximately half the imaging wavelength. This limitation arises from the wave nature of light and the fact that any optical lens has a finite angular aperture or *numerical aperture* (NA).

The numerical aperture defines the maximum angle at which scattered light is collected by the objective. Higher collection angle means higher spatial frequencies and ultimately higher resolution.

What this means is that, when light with wavelength λ passes through a numerical aperture NA it gets refracted with different angles such that:

$$sin\theta_{max} = NA$$

(3.3)

If the wave has wave vector $k_0 = 2\pi/\lambda$ and its projection on the sample plane is $k_x = k_0 sin\theta$, then the maximum spatial frequency that satisfies the diffraction limit is

$$k_{max} = k_0 sin\theta_{max} = (2\pi/\lambda)NA$$

(3.4)

The optical diffraction limit can be expressed more rigorously according to Abbe’s and Rayleigh’s criterions in expressions 3.5 and 3.6

$$d_{Abbe} = \frac{\lambda}{2NA}$$

(3.5)

$$d_{Rayleigh} = \frac{0.61\lambda}{NA}$$

(3.6)

Abbe’s limit holds when object separation equals the Airy disk radius–the diffraction pattern from a circular aperture.Rayleigh’s criterion resolves objects when one’s central maximum falls on the first minimum of the other.

2.5 Interferometric Scattering Microscopy (iSCAT)

One of the most important features of stroboSCAT microscopy is that it allows detection of very small changes in the optical properties like the refractive index upon proper photoexcitation of the semiconductor. Detecting such small changes requires ultrasensitive, label-free probes with a high signal-to-noise ratio. The diffraction limit can hide these small signals.

stroboSCAT in its current inverted microscope configuration, leverages interferometric scattering to enhance contrast. *Interferometric scattering microscopy (iSCAT)* is the steady-state analog to stroboSCAT. In iSCAT, the imaging originates from a laser beam that scatters from small objects (e.g., nanoparticles, proteins) and reflects from the substrate, providing both signal and background reference[24]. The weak scattered field interferes with the reference beam so that the detected light intensity reaching the imaging sensor takes the form:

$$I_{iSCAT} = \propto \left|E_r + E_s\right|^2 = \left|E_i\right|^2 [r^2 + s^2 + 2rs(cos\phi)]$$

(3.7)

Here E_i is the incident field, *r* and *s* are the reflection and scattering coefficients, $E_r = E_i r e^{i\phi_r}$ and $E_s = E_i s e^{i\phi_s}$, the phase term $\phi = \phi_r - \phi_s$. Equation 3.7 shows that iSCAT intensity depends $|E_r|^2$, $|E_s|^2$ and the cross-term $2Re[E_r E_s^*]$which encodes the phase difference. The Clausius-Mossotti relation indicates that

$$s \propto \alpha = \epsilon_{med} \frac{\pi D^3}{2} \frac{\epsilon_{particle} - \epsilon_{medium}}{\epsilon_{particle} + 2\epsilon_{medium}}$$

(3.8)

Here *D* is the particle diameter. This expression assumes Raleigh scattering of the point object. Since $s \propto D^3$, the interference term–proportional to the product *rs*–dominates over $|s|^2$, boosting sensitivity. By collecting both the reference and the scattered waves with a widefield probe, iSCAT exploits the cross term to enhance weak scattering signals. The cross-term dominates for small particles, then it linearly scales with the scattered field and it gets amplified by the reflected field. Increasing the incident field, the sensitivity increases. This cross-term additionally brings itself information on the phase changes of the scattered field.

2.5 From iSCAT to stroboSCAT

In iSCAT, one detects the scattered field from a small object by interfering it with a reference beam reflected from a non-perturbed region of the sample. The interference amplifies the contrast signal that arises from an object's local change in polarizability.

In analogy, in stroboSCAT, a diffraction limited pump pulse is used to photexcite the material with sub-micron resolution[25,26]. This excited state profile acts like the scattering object in iSCAT. The photoexcited species–bound excitons, free charges, ions, heat–act as point scatterers which modify the dielectric function[22].

First a pump-off reference interferogram I_{OFF} is recorded, then the pump is introduced and the delayed probe records the I_{ON} in an excited state. The tuning of the delay allows to resolve the changes in the scattering profile of the material, imaging the diffusion and recombination of the energy carriers. The normalized differential contrast is:

$$I_{strobo} = \frac{I_{ON}-I_{OFF}}{I_{ON}} \simeq \frac{2\Delta s cos\phi}{r}$$

(3.9)

where the intensity of the stroboSCAT signal is proportional to the amplitude change in the scattered field (Δs), and the changes in polarizability and refractive index. ϕ is the phase difference between E_r and E_s.

In principle, this technique is capable of imaging any photoexcitation, without the need of a strong light absorption at the probe wavelength or emission. The phase term in equation 3.9 also determines the magnitude of the contrast.This phase is given by the difference in the reflected and scattered phases and it results from three components as shown below.

$$\phi = \phi_G + \phi_s + (4\pi nz)/\lambda$$

(4.1)

The term $(4\pi nz)/\lambda$ represents the wave's propagation in space. The ϕ_s is the term introduced by the scattering from the object and the ϕ_G is called *Gouy phase shift.*

It was experimentally observed that a Gaussian focused beam accumulates an extra phase shift of 180° going through the focal region. This optical effect is due to the tight focus confining the field, curving its wavefronts and forcing off-axis rays to longer geometric paths and carrying different wave vectors than the on-axis rays.

The Gouy phase shift behaviour is shown in Fig. 11 and can be computed as $\phi_{Gouy} = arctan(\frac{z}{z_R})$ where z_R is the Rayleigh range.

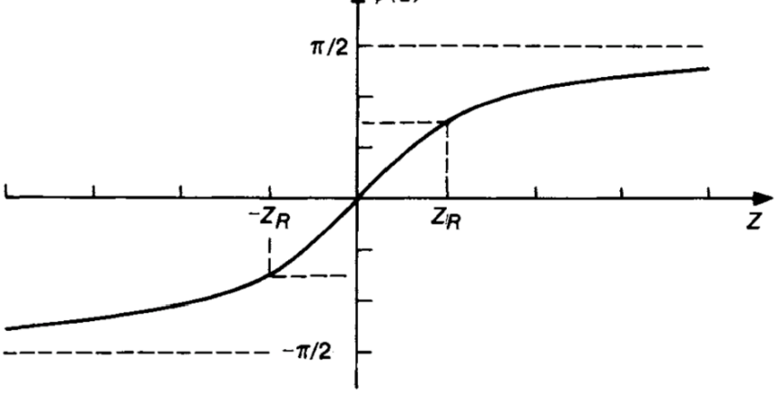

Figure 10. Gouy phase shift as a function of the position in space [27]

Each point at the beam wavefront will have a different phase, so the extra shift allows the compensation of all the different geometrical paths. [27] The $\phi(z)$ varies with the depth and because of that, $cos\phi$ crosses the zero at a specific z, allowing the use of the stroboSCAT contrast sign-flip, to resolve vertical carrier motion. troboSCAT is sensitive to whatever photo-induced carrier acting on the intensity or phase of the differential contrast, using a widefield probe to image micron-scale fields in a single exposition. Being a pump-probe technique it also adds up the temporal resolution, effectively providing a 4D excitation mapping of the material [22].

2.6 Optical Model of Pump–Probe Microscopy Signal

The above description of pump–probe microscopy in a reflection geometry in terms of interferometric scattering microscopy has proven to be a useful framework for understanding the sign and amplitude of the signal. However, a separate formalism is emerging that starts from the wave optics and solves the propagation of waves through the material, accounting for the modified refractive index profile in-plane and out-of-plane. [28]This model gives excellent agreement with data, even reproducing the full differential profile and interference pattern. The model allows for accounting for the seperate impacts of Δn, Δk, the underlying profile width, and depth and shape of the excited distribution. We do not elaborate on this model further as it is not directly used here.

2.7 State-of-the-Art Techniques for Probing Energy Transport

Over the years, many optical techniques have been developed capable of tracking energy flow in nanomaterials at ultrafast timescales and nanoscale distances. These approaches are crucial for understanding electronic and thermal transport in emerging semiconductors especially when structural and energetic inhomogeneities significantly influence the transport properties.

Transient microscopies are used to directly resolve the spatiotemporal evolution of initially localized photoexcitation products. These methods are based on the repeated photoexcitation of the sample using short laser pulses with subsequent imaging of the changes in the spatial distribution of energy carriers. This provides insights into energy relaxation pathways, carrier lifetimes, diffusion constants, and recombination mechanisms in semiconductors. This is particularly useful in the study of emerging low-dimensional systems as colloidal nanocrystal and 2D materials. In this section, we briefly discuss the capabilities of the most commonly used time-resolved methods and their intrinsic limitations.

Pump–probe spectroscopy consists of exciting a material with short laser pulses called “pump” and probing the excited energy carriers with laser pulses called “probe”. By varying the time delay between pump and probe pulses it is possible to reconstruct both the diffusion and relaxation of the excited-state populations in time. As mentioned before these methods give access to the observation of carrier lifetimes, hot electron cooling and trap states study in NCs. The signal used for detection and imaging can be obtained in three ways mainly: transient absorption, transient photoluminescence, and transient scattering all shown in Fig. 6.

In **pump-probe microscopy**, the sample is excited with a focused laser pulse, changing the sample’s local optical polarizability. After each pulse the region of interest (ROI) is imaged by a probe laser pulse, either with a scanning focus or a wide-field probe beam. This can either be done in a transmission geometry to measure transient absorption, or in reflection to measure transient reflection. The differential absorption changes are measured as a function of time and space, sometimes with spectral resolution or otherwise with a narrow band to image carrier diffusion. The advantage of this technique is that it can independently target different excited species by tuning the probe wavelength to resonate with specific transitions e. Due to its sensitivity to depopulation of the ground state, it can be used to study even non-luminescent materials. Being a pump-probe technique, it can offer ultrafast time resolution [6]. The particular configuration of reflectance imaging with a wide-field probe pulse, this transient reflection microscopy technique is known as **stroboscopic optical scattering**

microscopy (stroboSCAT). This latter technique is the main focus of this thesis. This interferometric optical scattering microscopy technique that can be used to track electronic and thermal energy flow at the nanoscale. These images are collected by a CMOS camera and compared with the reference image taken in the absence of a pump pulse. The measurement is repeated with progressively longer pump-probe delays, thus visualizing the spatiotemporal evolution of the diffusing excited population.

Transient photoluminescence microscopy is also used to measure the distribution of photoexcited states in space and time. It differs from the previous mechanism because after the photoexcitation a photodiode is rastered across the ROI to collect a photoluminescence map. This technique provides information on the evolution of the excited population distribution from the initial excited spot by measuring the decay rate of the emissive state. It relies on the detection of spontaneous radiative emission, so the signal analyzed has almost no background noise if compared to transient absorption. The drawback of transient photoluminescence is that its imaging signal is useful if the transport is dominated by excitons, whereas free carrier dynamics are much more difficult to interpret [6].

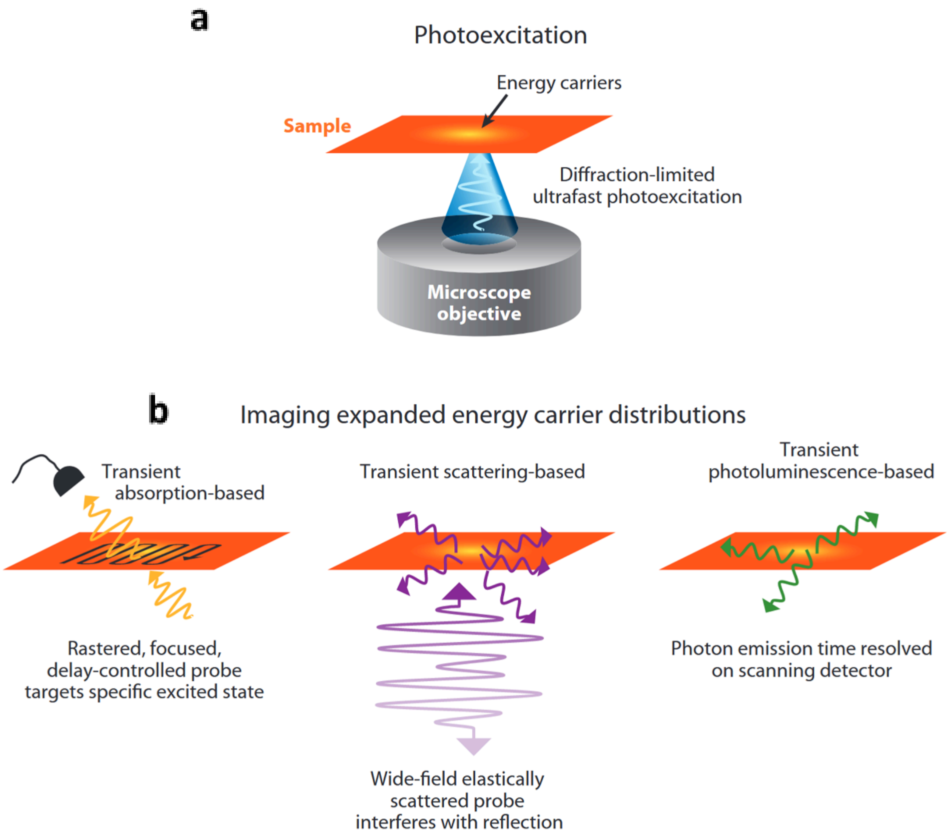

Figure 11. (a) a focused and ultra-short laser pulse excites the sample. (b) Transient absorption, transient scattering and transient photoluminescence techniques [6].

Optical transient microscopy methods are ideal for capturing the earliest stages of photoexcited dynamics because of their exceptionally high temporal resolution. Additionally, they don't require any physical contact with the sample and being optical, they allow studies in both ambient and controlled environments. These techniques can be spectrally tuned to work from UV to mid-IR, at variable pressures and temperatures–if combined with cryostats and vacuum systems.

Most pump–probe setups rely on overlapping focused beams with resulting spot sizes in the 0.5-few microns range. This scale is often larger than the characteristic sizes of defect features in NCs or TMDs films and as a result there is an intrinsic limit to the local variations in transport due to structural disorder, grain boundaries or strain fields that can be measured.

Another important limitation is that the optical signatures of different energy carriers often overlap in time and spectral response. Disentangling the electronic and thermal transport can be challenging, because both arise from changes in refractive index or band filling. This means that both charge carriers and transient heating have peaks in differential spectra near the ground state absorption peaks in general. In heterogeneous systems, like the ones under analysis in this work, the comparison with simulated dynamics together with spectral deconvolution and fitting models, can be effective to understand complex processes happening at the same timescale and spatial distributions.

As we will see more in detail in the next chapter, stroboSCAT microscopy lets us overcome many of the above discussed limitations by combining scattering-based detection with wide-field imaging at nanosecond-scale temporal resolution. With stroboSCAT we can record images at each time delay instead of rastering the probe pulse across the sample, which allows us to visualize energy carriers propagating through the material after excitation. This technique (which will be better described in Chapter 2) gives access to submicron spatial resolution and nanosecond time resolution. It is sensitive to all the phenomena that can cause changes in the complex refractive index of the material, including thermal and electronic carrier diffusion regardless of their emissivity. Due to spatially resolved output data, comparison with synthetic data obtained through simulation is quite straightforward.

2.8 StroboSCAT Experimental Setup

This section explains how a stroboSCAT microscope is built and how its high spatio-temporal resolution along with its sensitivity to different energy carriers is used to study microscopic carrier transport in semiconductors. To perform all the experiments described in this work, I used the custom stroboSCAT implementation from Dr. James Utterback at the Institute of NanoSciences of Paris (Fig. 12 shows a schematic representation). Below we will cover each section of the experimental setup, (1) the optical layout, (2) the light sources and electronic control for timing, (3) the detection and imaging system and (4) the time-resolved pump-probe spectrometer configuration, and in the end (5) some data analysis workflow.

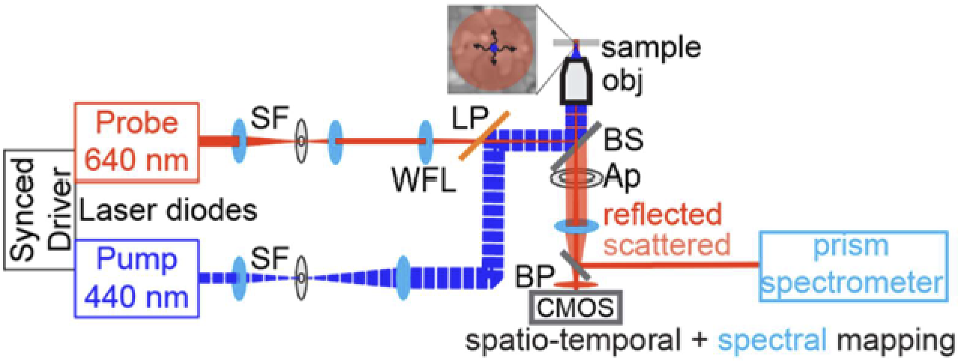

Figure 12. StroboSCAT optical layout representation as implemented by Delor et al. [29]

2.8.1 Laser Sources and Beam Paths

The pump and probe beams are spatially filtered through 25 μm pinholes. The pump is telescoped to get a ~6 mm diameter collimated beam, while the probe beam is reduced to ~1 mm and focused into the back focal plane of the objective lens using an *f* = 300 mm wide-field lens before entering the microscope. Both beams are overlapped passing through a long pass dichroic mirror which was chosen according to the pump wavelength selected. The small amplitude of the pump beam is obtained from a partial reflector to follow an alternative path going directly to the CMOS camera as a reference for pump-probe phase locking purposes (see next sections) without entering the microscope. The combined beam is later projected on a 50/50 beam splitter (BS).

The pump arrives collimated into the objective, while the probe is focused at the back focal plane of the objective to get the confocal excitation and widefield probe spots, respectively. The beam reflected from the sample-substrate interface serves as the reference field E_R, while scattering from pump‑induced refractive‑index changes constitutes the signal field E_S, both are sent to the CMOS camera for imaging, passing through a band pass filter to prevent the reflected pump beam entering the camera. For power dependence experiments (discussed later), neutral density filters (OD) were added to the pump beam path to change the pump beam optical power between each run of the experiment.

2.8.2 Focusing Through the Objective

A Leica HC PL APO 63x/1.40‑NA oil‑immersion objective focuses the pump to a near‑diffraction‑limited spot (with measured FWHM 300–540 nm, depending on wavelength: 300 nm FWHM for a 405 nm wavelength pump, 460 nm FWHM for 635 nm wavelength pump, and 540 nm FWHM for 775 nm wavelength pump). The probe typically has a ~10 µm diameter wide‑field illumination, to ensure uniform coverage around the pump focus ("pump-in-center" scheme). In this way the charge carriers or thermal perturbations are localized while probing a sufficiently large area for spatial‑profile analysis.

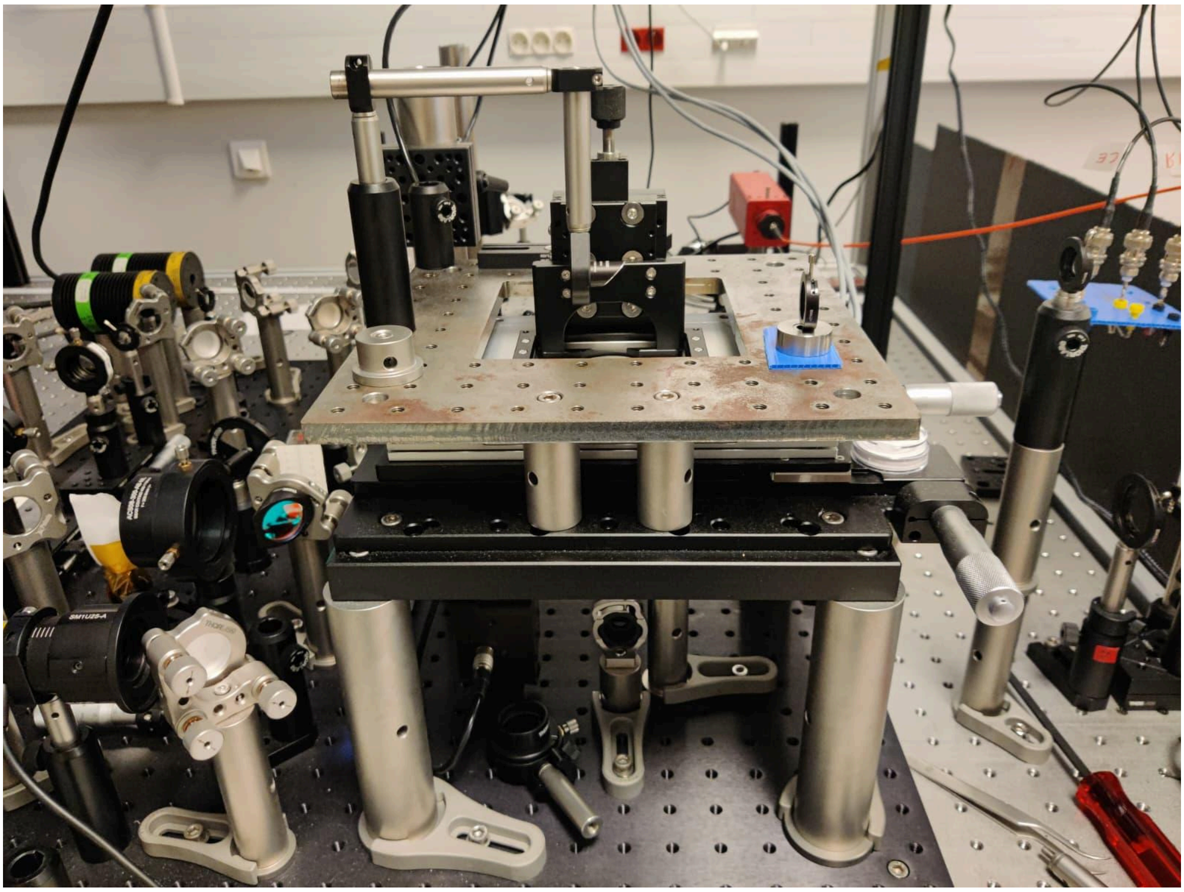

Figure 13. Objective in the inverted microscope configuration used as part of stroboSCAT optical layout. At the top of the objective turret is a 3D piezoelectric stage used for sample movement.

2.8.3 Mechanical and Environmental Stability

All optics are mounted on a compressed-air damped table to reduce vibrations that could be harmful during long exposure measurements. The sample is mounted on top of the inverted microscope, and it can be moved relative to the objective with manual micrometer translation stages. For finer adjustments we use piezo-actuated micrometric stages to control each axis from their dedicated software.

The choice of having both the pump and probe in a common‑path geometry and collecting both beams through a single high‑NA objective maximizes phase stability and interferometric gain—critical for detecting fractional scattering changes as small as 10^{-5}–10^{-4} in $\Delta R/R$ [29].

2.8.4 Light Sources and Control Systems

stroboSCAT microscopy achieves high temporal resolution through the generation and precise synchronization of ultrafast pump and probe pulses. We employ fast pulsed diodes and a digital delay system to achieve <25 ps jitter and flexible pump–probe delays up to several microseconds.

2.8.5 Pulsed Diode Lasers

For all data shown in the text, we use PicoQuant LDH laser diodes as light sources at fixed wavelengths 405 nm, 635 nm and 775 nm (LDH-D-C-405, LDH-D-C-640, LDH-D-C-780, PicoQuant (Fig. 14). Each laser diode emits pulses shorter than 100 ps. For spectrally-resolved measurements, a Fianum supercontinuum (broadband 500-800 nm, 50 ps pulses) is used for the probe. Coupled to the Fianum, an acousto-optic tunable filter (SuperK Varia) selects narrow spectral bands if desired.

Each laser is operated by drivers from PicoQuant to control the pump-probe time delay.

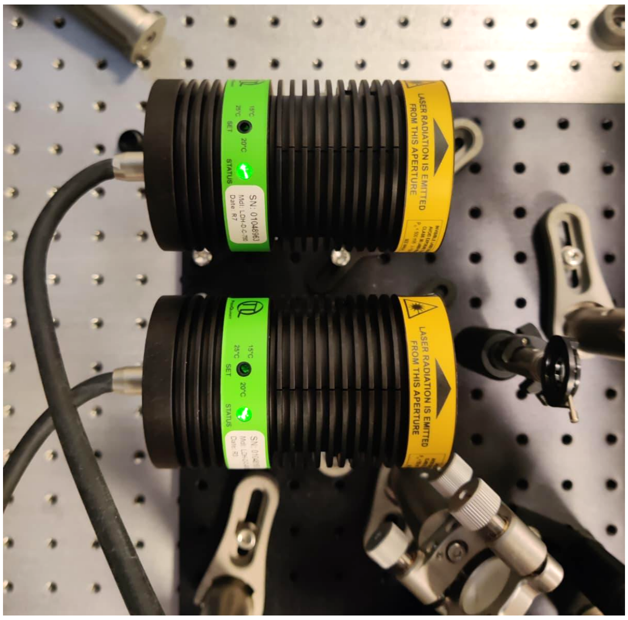

Figure 14. Two examples of the laser diodes used for pump–probe measurements.

The diode lasers can be set to operate at different repetition rates to balance relaxation in the sample with sufficient signal averaging per frame. For the experiments described later, we use laser repetition rates of 500 kHz, 1 MHz and 2 MHz depending on the material with the pump diode modulated at 660

Hz using the PicoQuant driver. This on–off modulation is the reference for lock‑in subtraction: every other camera frame is “pump‑off,” to get direct background for computing $\Delta R/R$.

The choice of the lasers to be used for each experiment is important. The pump laser source must provide enough energy to excite the material, thus higher than the bandgap of the semiconductor. In the next chapters we will see how the tuning of the pump wavelength–and thus lattice thermalization–and fluence can be used to control the nature of the dominant phenomena observed in stroboSCAT measurements. To choose which probe wavelength to use, we need to identify the electronic resonances of the material that will enhance the transient signal and allow a higher SNR. In the presence of many resonances, the probe energy should be selected in order to be more sensitive to the excited state of choice.

2.8.6 Delay Generation

In the case when the PicoQuant lasers are used for both the pump and probe, the laser driver operates both lasers with a built in oscillator and delay control. When using the supercontinuum laser as the probe, we synchronize the laser sources electronically by triggering the PicoQuant laser diode driver with a pulse train synchronization signal from the supercontinuum laser). In that case the trigger signal is first delayed with a digital delay generator (DG645, Stanford Research Systems) and then feedbacked to the CMOS camera to synchronize the image capture.

2.8.7 Fluence Control and Calibration

The pump fluence is calculated by measuring the power arriving at the sample position and measuring the pump spot size by imaging and fitting its reflection. To measure the power we use a microscope slide format power sensor and power meter . The fluence can be controlled using neutral density filters before entering the microscope.

One aspect that needs to be carefully accounted for when doing stroboSCAT experiments, is related to the choice of laser diode power. Together with sample damage, afterpulsing requires special care when studying fast dynamics (less than ~500 ps). When the current powering these laser diodes is too high, they show a second light pulse 100-200 ps after the principal one[22]. If working with very short delays, this second unwanted light pulse can overlap to the probe, affecting the results of the measure keeping the material under excitation.

2.8.8 Detection and Imaging

stroboSCAT contrast relies on measuring small changes in reflected intensity $\Delta R/R$. A scientific CMOS camera is required to image those changes.

The light transmitted through the beamsplitter is isolated with a band-pass filter and focused onto the CMOS detector triggered at 660Hz by the laser driver (Fig. 15). The camera is equipped with a global shutter, avoiding rolling-shutter mode to capture all the pixels at the same time. The pixel calibration was done using a 1951 USAF Pattern resolution target , giving 28nm/pixel.

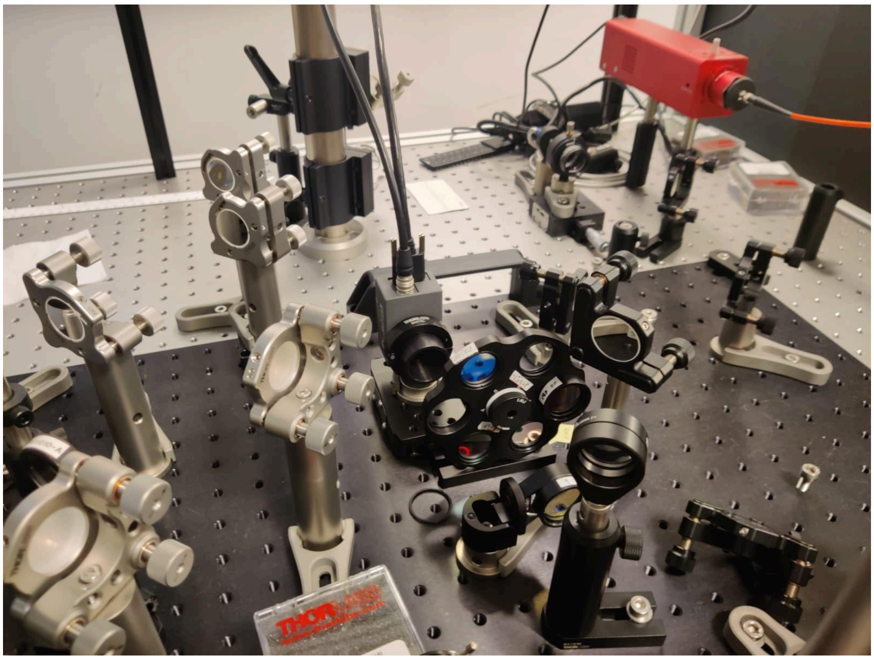

Figure 15. Section of the optical layout of stroboSCAT experiment, showing the CMOS camera used for detection. In front, a filter wheel is used to selectively block out the pump beam

2.8.9 Data Acquisition

Data acquisition is implemented in LabVIEW 2022 64-bit, the data analysis and plotting will be explained in detail in the next sections.

In LabVIEW, a routine subtracts each pump-off frame I_{off} from the subsequent pump-on frame I_{on} and divided by I_{off}, yielding

$$\Delta R/R = \frac{I_{on} - I_{off}}{I_{off}}$$

(4.1)

By storing both raw and differential frames, we get more flexibility for post-processing, drift correction, and noise analysis.

As it will be shown better later, to obtain the relaxation and mean-squared expansion curves, each transient reflection image ($\Delta R/R = \frac{I_{on} - I_{off}}{I_{off}}$) of a given stroboSCAT time series is fitted to a normalized Gaussian profile function with a common center and floating amplitudes and widths. By normalizing the Gaussian function, the amplitude represents the spatially-integrated amplitude (related to the change in the complex refractive index), thereby giving the population decay traces. The width of the Gaussian σ versus *t* is used to get information on the energy carrier diffusion in time with precision down to tens of nanometers, $\sigma^2(t) - \sigma^2(t_0)$.

This wide-field transient reflection detection provides maps of refractive-index dynamics with sub-nanosecond temporal resolution, which is ideal for capturing transport and spatial heterogeneity in nanomaterials, which is what this work aims to do in the next chapters.

2.8.10 Time-Resolved Pump–Probe Spectrometer

Pump–probe microscopy measurements of carrier diffusion offer a power approach for local, optical measurements of transport properties, however, they are limited to probing one wavelength at a time. Spectrally-resolved pump–probe measurements, which have been around much longer, offer complementary information about the transient energetic dynamics. However, in order to directly compare transient spectroscopy measurements to the excitation conditions of carrier diffusion measurements, we needed to implement transient spectroscopy capabilities into the same microscope used for stroboSCAT. As part of the study described in Chapter 3, we added on such a capability.

The experimental setup for transient reflection spectroscopy measurements was built with inspiration from a previously described instrument developed by the Delor Lab[30] with some modifications. To get the probe pulses, we use white-light pulses with ≈50 ps pulse width obtained from a Fianium supercontinuum laser. For spectroscopy measurements, we use a broadband wavelength window of about 500-800 nm. The pump pulses are generated with the same laser diodes introduced previously (405, 635, 520, or 775 nm). The pump laser diode is controlled by the same PicoQuant laser driver as used for stroboSCAT. The two lasers are synchronized by triggering the PicoQuant laser diode driver using a pulse train synchronization signal from the supercontinuum laser after being delayed with the delay generator (DG645 from Stanford Research Systems). The pump is modulated at different frequencies with the PicoQuant driver as done in the stroboSCAT setup. The pump and the probe beams are overlapped using a dichroic mirror. They are then directed into the same home-built inverted microscope used for stroboSCAT. Both the pump and probe reflected from the sample are collected through the same objective, pass through the 50/50 beam splitter and an optical fiber coupled to the high-speed linear CMOS-based single grating spectrometer from Ultrafast Systems that was calibrated using a mercury lamp.

Transient reflection spectra are generated by taking the difference between pump-on and pump-off pixel intensities, which is normalized to the raw pump-off intensities and yields $\Delta R/R$ spectra. Pump-on and pump-off spectra can be distinguished as the pump is spectrally separated from the wavelength range of interest.

This dual-mode functionality—wide-field imaging and point-spectroscopy on the same platform—provides a comprehensive toolkit for correlating spatially resolved transport maps with spectrally resolved dynamic signatures, with the possibility to have identical excitation conditions.

2.8.11 StroboSCAT Data-Analysis Workflow

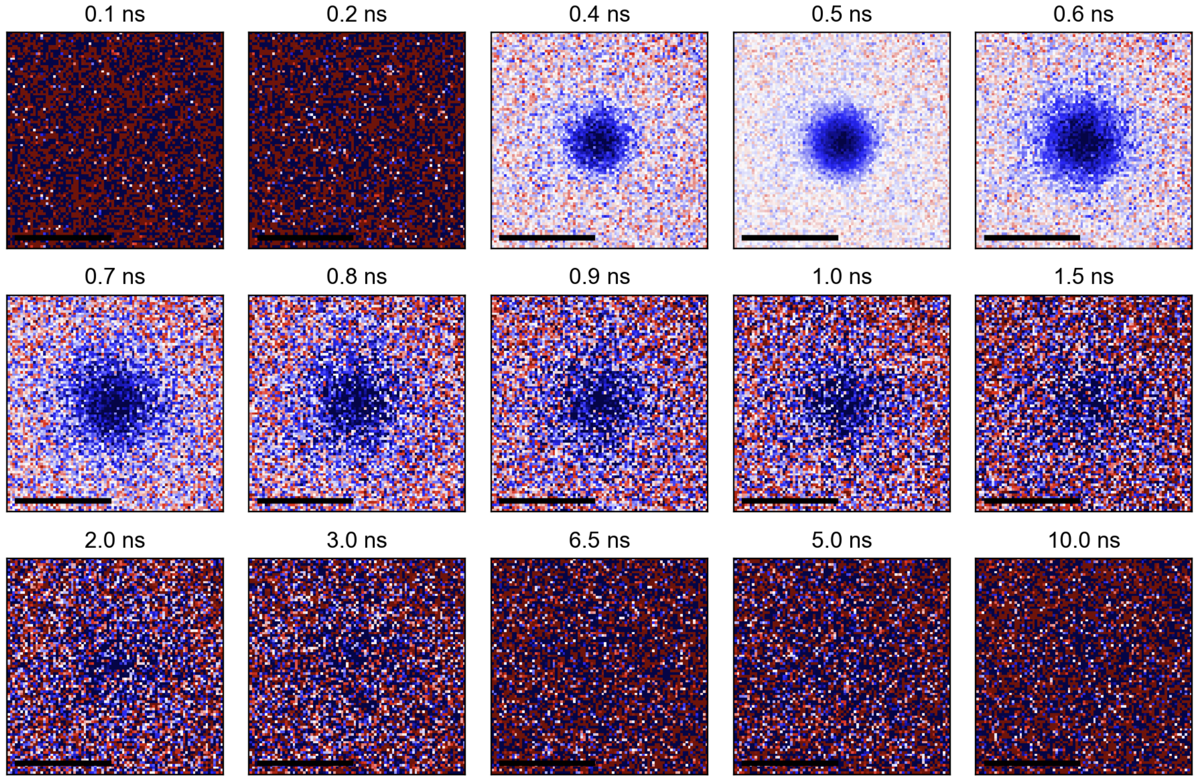

Figure 16. Example of stroboSCAT image of a WSe2 flake with 640 nm pump and 780 nm probe at 500 kHz repetition rate

When we analyse the raw stroboSCAT images–the transient reflection signal (Fig. 13) We extract two types of information which are important to describe the properties of the semiconductor. First of all we get the relaxation in time of the excited carriers in the transient reflection images–to report the carrier recombination lifetime or the thermal relaxation kinetics. This is done by finding the spatially-integrated amplitude of the carrier profile as a function of time. Second, the stroboSCAT data can be used to quantitatively measure the broadening of the excited-spot profile, which is used to get microscopic diffusion coefficients and the mean squared displacements (MSD). In this section I am providing a quick overview on the analysis steps needed to go from raw detector frames to kinetic rates and diffusivities.

2.8.12 LabView experimental setup interface

To control the different components of the setup, we use a Labview interface. It communicates with the laser driver software, with the mechanical shutter, with the piezo-stages and with the Camera software.

In the Labview GUI you can choose the amount of scans to be taken (the higher is the amount of scans, the better is the quality of the measures–they will be averaged by LabView)and the list of pump–probe time delays.
There are some feedback display interfaces which allow you to do a quick unsaved test image before performing the measure, to check if there's pump–probe signal and to do finer adjustments; you can also monitor the measurements on the go to check for focus changes. he pump and probe laser powers and repetition rates can be controlled. Through the camera preview it is also possible to image and fit the excitation spot, to check if it has the right shape–it should be gaussian as the pump laser beam–and intensity.

The averaged acquired scans are accessed by a Python code, and manipulated into an array which maps the intensity of the $\Delta R/R$ to the x and y coordinates and the corresponding time delay of the image.

A graphical interface allows an initial rough choice of the region of interest (ROI) to be fitted. Usually the ROI is chosen so that it includes the excitation spot and its maximum extension in time as shown in Fig. 17.

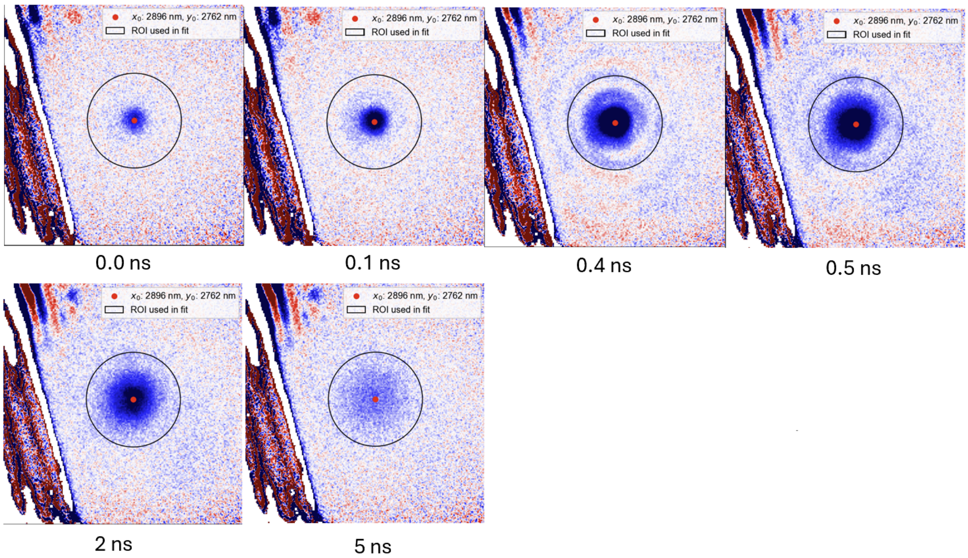

0.0 ns 0.1 ns 0.4 ns 0.5 ns

2 ns 5 ns

Figure 17. Example of the ROI selection on △R/R signal at different time steps

We typically fit a two-dimensional Gaussian function to each time step in the averaged dataset from stroboSCAT.

$$G(x,y) = \frac{A}{\sqrt{2\pi\sigma}} exp(- (\frac{(x-x_0)^2+(y-y_0)^2}{2\sigma^2})) + h$$

(4.2)

The Gaussian fit can be chosen to be isotropic or anisotropic (as in Fig. 18); this is important when the diffusion of the energy carriers depends on the geometry of the system. Through this thesis we will always deal with isotropic diffusion phenomena, thus isotropic gaussian fits.

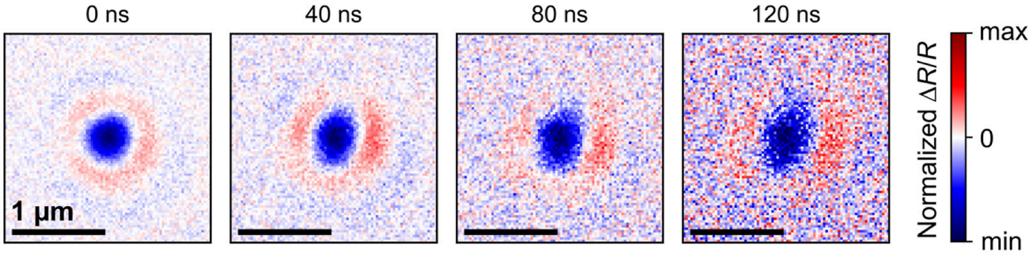

Figure 18. Example of R/R signal due to anisotropic heat diffusivity [31]

The code uses an algorithm developed by Matias Feldman to find the best center for the Gaussian fit and the other fitting parameters for each time point of the measurement (i.e amplitude, sigma, major and minor axes for anisotropic fits).

Concerning the spectroSCAT data analysis, the Labview program works the same way as for stroboSCAT experiments. The difference stands in the type of data obtained–several time and wavelength dependent spectra deltaR/R profiles– which are background-subtracted, averaged and later plotted. What we look for in time-resolved spectra is shifts and broadenings in the resonance frequencies of the material.

2.8.13 Data Analysis

Once having fit the Gaussian curves for all the time points, the amplitude in time can be tracked to resolve the decay of the transient reflection signal. By tracking the variance of the Gaussian fits in time, we can compute the change of the diffusion coefficient in time, that is called "mean squared displacement (MSD)".

In Fig. 19, several amplitude time dependent profiles are shown–which physically represent the relaxation of the material in time. Such decay curves can in principle have a share of decay kinetics and functional forms due to relaxation mechanisms. They can be fitted with either power laws or exponential decay laws depending on the relaxation process dominating at each timescale. In both cases the relaxation allows the extraction of the lifetime of the energy carriers involved. Sometimes the relaxation kinetics shows multiple behaviors at different timescales, usually caused by different decay processes.

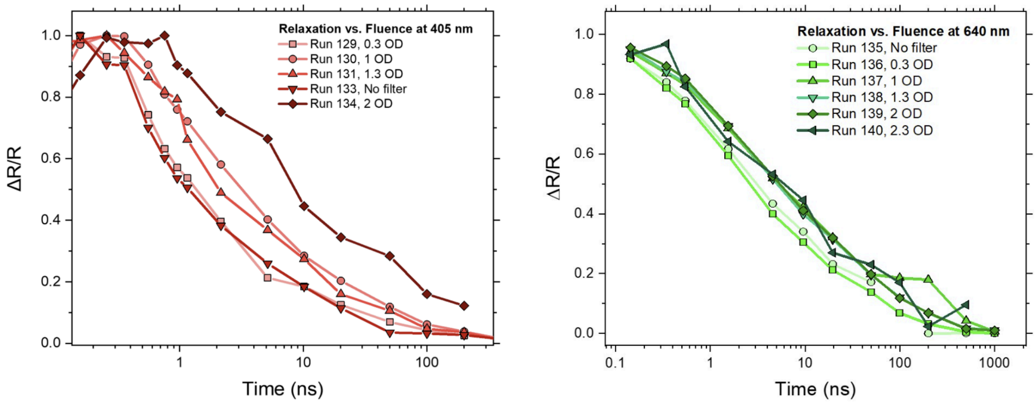

Figure 19. Examples of relaxation kinetics in CdSe nanocrystal film for 405 nm and 640 nm excitations

To accurately extract information about the fast decay components, we can convolute the instrument-response function (IRF) with an exponential–or multiexponential–decay function. The IRF describes how a pulse of finite duration keeps contributing to the photoexcited population even after the maximum peak; in the case of stroboSCAT the IRF is approximated by a Gaussian. For instance below an example of a multi-exponential fit function convoluted with the Gaussian IRF.

$$C(t) \;=\frac{1}{2}[1 + erf(\frac{\frac{t-\mu}{\sigma}-\sigma\lambda}{\sqrt{2}})](exp(-\,(t\,-\,\mu)\lambda + \frac{(\sigma\lambda)^2}{2}))$$

4.3

Fitting this more function not only we get a good approximation of the relaxation from early time (see Fig. 20), but we can also obtain the time-zero of the excitation. The time zero represents the peak of the finite excitation pulse. An example of such a fit is given below.

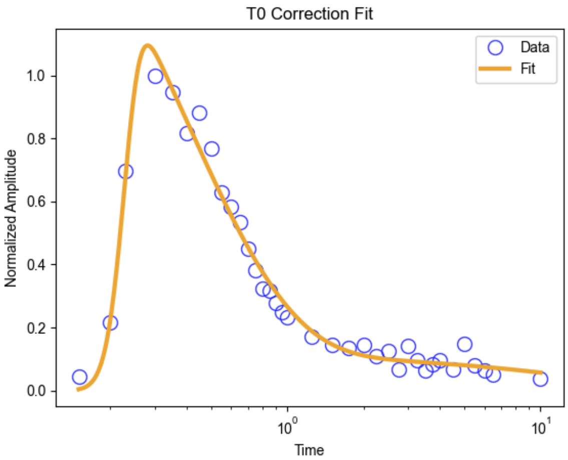

Figure 20. Example relaxation experimental data fitted with IRF-Multiexponential convolution function

The time zero variance does not typically align with the true experimental time zero—when the pump and the probe pulses coincide—but it is instead set just after the excitation peak's maximum to minimize artifacts from the instrument response function. At the peak of intensity, excitation remains incomplete and multiple overlapping processes render the data unreliable. To obtain a clearer picture, we wait until the sample's relaxation phase begins.

By tracking the width change of the Gaussian in time we can obtain information about the transport of the excited carriers. We compute the variation in the variance with respect to the value at time-zero, t_0.

$$MSD(t) = \sigma^2(t) - \sigma^2(t_0) = 2Dt \tag{4.4}$$

Table 32.

Here D is the diffusion coefficient.

In some cases transport is nondiffusive. An advantage of performing stroboSCAT is that it offers access to such dynamical transport behavior. The instantaneous diffusion coefficient can be found by looking at the slope of a linear fit of the experimental MSD plot in log-linear scale.

Transport can often be characterised as subdiffusive, diffusive or diffusive: $MSD = Kt^\alpha$. On a log-log scale, a power law can be fitted to the experimental points with a straight line and slope given by α.The α coefficient is what we observe to deduce the type of transport–i.e diffusive ($\alpha = 1$), subdiffusive ($\alpha < 1$), superdiffusive ($\alpha > 1$), as in Fig. 21. This subject is treated more in detail in Chapter 3.

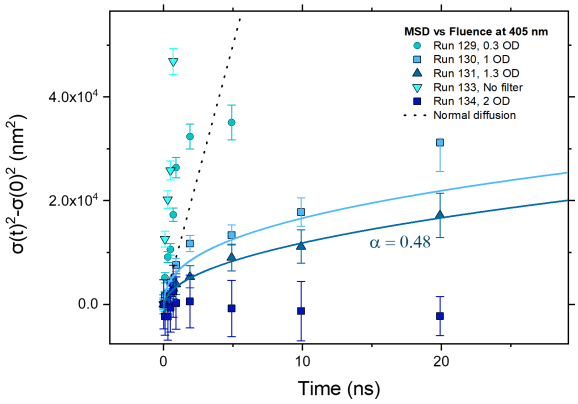

Figure 21. Examples of expansion curves at different fluences with power law fits to show different diffusion regimes

While optimizing the fit parameters of the gaussian functions, the code stores the error at each time step. This allows easy removal of inaccurate measured points by inspection and to determine the overall quality of the stroboSCAT measures.

Chapter 3

Pump-Probe Experiments on Semiconductor Nanocrystal Films

Adapted from De Bellis et al. "Simultaneous Electronic and Thermal Signatures in Pump–Probe Spectroscopy of Semiconductor Nanocrystal Films", Nano Letters, 2025, 25, 18, 7317-7325

In this chapter we describe stroboSCAT experiments on colloidal nanocrystal (NC) films. The principal study described in this chapter is about how both electronic excitation and transient heating contribute to the pump–probe signals of semiconductor NC films and how one can investigate the relaxation and transport dynamics of both. While NC systems were introduced in Chapter 1, we give some more general information on their optical and electronic features, why they induce quantum confinement of charge carriers, and what this implies for electronic transport. We also briefly investigate the Auger nonradiative recombination process and its role in lattice heating. The study of both thermal and electronic transport properties of NCs can be leveraged to improve the efficiency and performance of NC-based optoelectronic devices.

3.1 Colloidal NCs and Synthesis

Films of colloidal CdSe and PbS NCs were chosen as a starting point for this fundamental study since these materials are well known in literature and the carrier transport remains interesting for optoelectronics applications. Quantum dots (QDs) exhibit size-dependent quantum phenomena with absorption and emission spectra depending on particle size due to quantum confinement effects when the size is on the order and smaller than the Bohr exciton radius. In that regime, the continuous bands of the bulk semiconductor turn into discrete states similar to a particle-in-a-box model. As the size of the NC gets smaller, the energy levels separate, increasing the band gap.

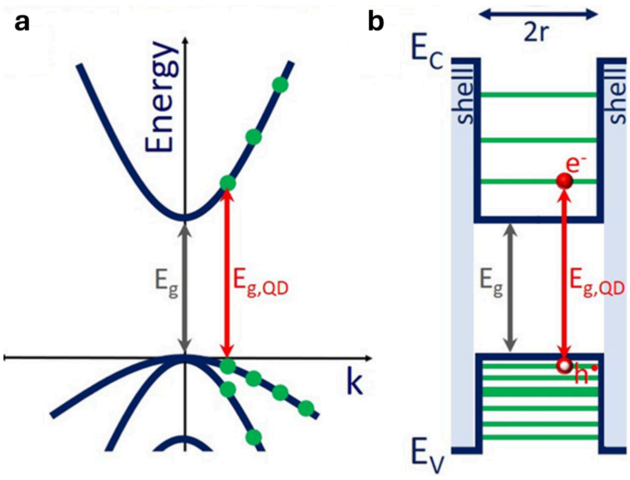

Figure 22. (a) E vs k band structure of a bulk semiconductor. (b) E vs k diagram of a QD of radius r [32]

The chemical synthesis conditions and reagents can be used to tune the sizes and shapes of the NCs, allowing control over the bandgap; thus, the QDs can be "designed" to absorb and emit light over a wide frequency range. These systems have narrow photoluminescence bands compared to molecular chromophores and broad absorption spectra. Briefly, a colloidal QD solution is obtained by introducing the precursors into a growth solution containing *organic ligands* which modulate the growth rate and enable colloidal stability. They can be later exchanged to other molecules to obtain the desired transport properties, for example to shorter ligands that give stronger electronic coupling by decreasing the NC–NC distance.

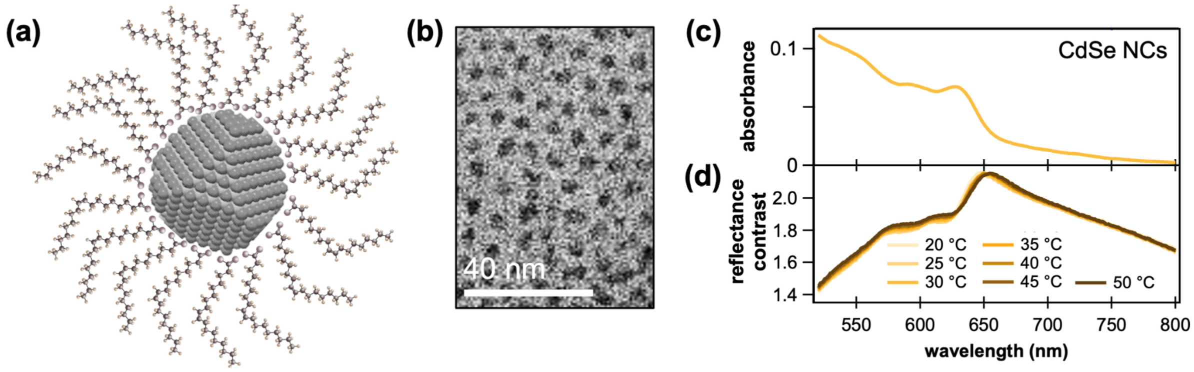

Figure 23. (a) Cartoon of nanocrystal with wurtzite crystal structure (such as CdSe) with common native ligands—oleate ligands. (b) TEM image of CdSe nanocrystals. (c) Absorption spectrum and (d) reflectance contrast spectrum of CdSe nanocrystal film, featuring a band gap around 640 nm.

3.2 Theoretical Models for Charge Transport in NCs

To understand how these films could allow efficient transport, it is necessary to study the diffusion of the excited carriers in a film of QDs and the dominating transport mechanisms [33]. NCs like CdSe and PbS QDs from colloidal solution form disordered assemblies where the distance between the neighboring NCs determines the strength of the electronic coupling. When these semiconductor NCs are photoexcited, an electron gets promoted to the conduction band and a hole is generated in the valence band. Then, they can relax through electron-hole radiative recombination and several non-radiative pathways–for example, trapping to localized defect states, Auger recombination and phonon emission. With stroboSCAT, we can study radiative recombination processes, but also the "side effects" of non-radiative processes like lattice heating.

We can use the equation 4.5 to describe the diffusion and recombination of the energy carriers

$$\frac{\partial n(x,t)}{\partial t} = D(t)\frac{\partial^2 n(x,t)}{\partial x^2} - k(t)n(x,t)$$

4.5

Where $n(x,t)$ is the energy carrier density distribution, $D(t)$ is the diffusion coefficient relative to the transport mechanism and $k(t)$ is the decay rate specific to the excited species. In case of constant diffusivity and decay rate with an instantaneous source $n(\tilde{x}, 0)$ the normalized solution of the Eq. 4.5 is

$$n(x,t) \propto n(\tilde{x},\ 0)\ *\ G(x,t)$$

4.6

Where $G(x,t) = \frac{1}{\sqrt{4\pi Dt}} exp(-\frac{x^2}{4Dt})$. Thus, we can define the density of excited carriers as by the convolution of the initial distribution profile and a Gaussian function which is used to represent the spread of the carriers as they undergo relaxation.

Due to the fact that the irradiation profile is that of a Gaussian laser pulse, we can assume the initial distribution of carriers will be evolving as a Gaussian too. To be more precise, during this relaxation phase, the diffusion profile can be well approximated by the convolution of two Gaussian distributions, giving $\frac{1}{\sqrt{4\pi Dt}} exp(-\frac{x^2}{2(\sigma^2(0) + 2Dt)})$. Still, we analytically describe the excited spot by using a broadening Gaussian as shown in Chapter 2.

Scattering processes affect charge transport in both bulk and NCs semiconductors, which manifests as a random walk that looks diffusive at sufficiently large length scales (Fig. 21). In bulk materials, carriers propagate in a band-like regime that can be modeled as a quasi-ballistic motion of energy carriers randomly scattered. Therefore the diffusivity can be expressed as follow

$$D = \frac{1}{3} v \lambda_p$$

4.7

Thus, diffusivity is determined by the average velocity *v* of the excited-state carriers and their mean free path λ between successive collisions in the crystalline structure. The resulting diffusion length is given by

$$L_D = \sqrt{2D\tau} = \sqrt{\frac{2}{3} v \lambda_P \tau}$$

4.8

Where τ is the lifetime of the carrier.

In NC films, there are several transport mechanisms and charge-transfer mechanisms, but in most cases a hopping regime dominates. One example is incoherent Förster hopping of excitons where excitons (both the electron and hole together) move between one site to a near one with a transition rate that is given by the relation:

$$k_{ET} = (\frac{R_0}{r})^6 \frac{1}{\tau_D}$$

4.9

Where R is the Förster radius of the exciton, *r* is the separation distance of the sites and τ is the exciton lifetime. In the case of hopping transport, the diffusivity is given by:

$$D = k_{ET} d^2$$

5.0

With *d* used to indicate the distance between neighboring sites. The diffusion length becomes:

$$L_D = \sqrt{2k_{ET}d^2\tau}$$

5.1

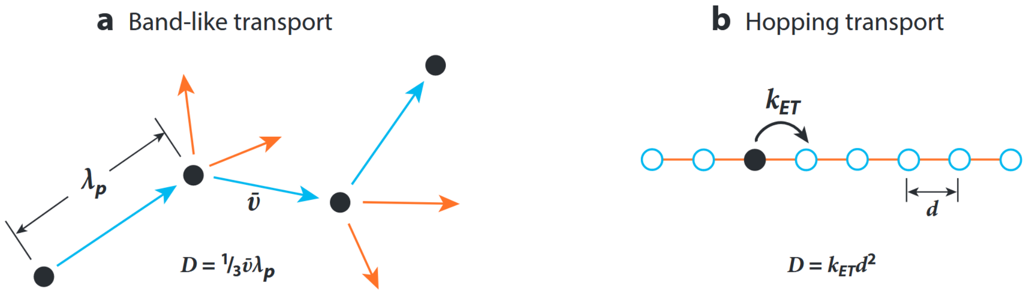

Figure 24. Schematic representation of the two transport mechanisms [6]

Another example of charge transport in NC assemblies is phonon-assisted charge transfer or polaron hopping. In this case the charge carriers tunnel through the ligand barriers. The ligands used during the synthesis not only stabilize the NCs in a colloidal state, but they influence the charge transport phenomena through their length and chemical composition [10]. To understand this mechanism, Nuri Yazdani and Samuel Andermatt and coworkers carried out DFT studies on single PbS NCs and clusters of up to 125 NCs, capped with iodine ligands. They showed that when an extra electron resided in the NC, the Pb–iodine at its surface undergoes expansion or contraction, whereas the Pb–S bonds on the NC surface keep the same lengths. This localized lattice distortion—driven by the Coulomb interaction between the charge carrier and the nuclei—defines the polaron. The energy required to reorganize these surface atoms is the *reorganization energy.* Their calculation of electronic coupling between neighboring NCs revealed it to be more than an order of magnitude smaller than this reorganization energy, indicating that carrier transport in these films is dominated by a weak coupling regime with ligand vibration-assisted hopping[6].

Quantitatively, the hopping rate of free carriers is well described by:

$$k_{ct} = N_p \frac{2\pi}{\hbar} V_{ct}^2 \sqrt{\frac{1}{4\pi\lambda k_B T}}\, exp[-\frac{(\Delta E+\lambda)^2}{4\lambda k_B T}]$$

5.2

Here, V represents the electronic coupling between neighboring NCs, which depends on the center-to-center distance between NCs for weak coupling. Np is the number of degenerate product states due to the number of neighboring NCs that can accept a charge. The λ coefficient is the reorganization energy, the energy required by the structures to adapt for charge transfer between NCs as discussed above. ΔE is the energy difference between the initial and final sites, which is null in an isoenergetic NCs sample with no electrostatic applied field. In contrast, it can capture the impact of energetic disorder of the sample. Variation in NC size, for instance, contributes to this heterogeneity. Diffusivity also depends on factors such as NC geometry (ligand length and shell thickness), the presence of voids, and the system's energetic landscape[10].

To quantify how a photoexcited carrier distribution broadens over time and space—across different pump wavelengths and fluences—we fit pump–probe data with a Gaussian profile. In conventional diffusion, carriers undergo a random walk scattering process whose variance increases linearly with time: In 1D, $\sigma^2(t) - \sigma^2(0) = 2Dt$. However, in QDs films like ours, we often see a sub-diffusive behavior. This is often described empirically by the power law:

$$\sigma^2(t) - \sigma^2(0) = At^{\alpha} \tag{5.3}$$

where α is the power-law exponent and A is a proportionality factor. For $\alpha = 1$ we recover the normal diffusion case. The transport is sub-diffusive when $\alpha < 1$ with a time dependent diffusivity:

$$D(t) = \frac{1}{2At^{\alpha-1}} \tag{5.4}$$

In a sub-diffusive regime (Fig. 22), the excited species initially spread rapidly after excitation, then gradually slow down at later times, settling into a quasi-static diffusivity state. This behavior arises from asymmetric site-to-site hopping rates in a disordered energy landscape [10]. As the excitons move energetically downhill due to energy transfer from high-energy sites to low-energy sites, the rate of hopping lowers as the carrier energy approaches the landscape energy. The width of the Gaussian distribution grows is proportional to diffusivity—which in NCs films depends on the transition rates and thus, on the specific carrier type.

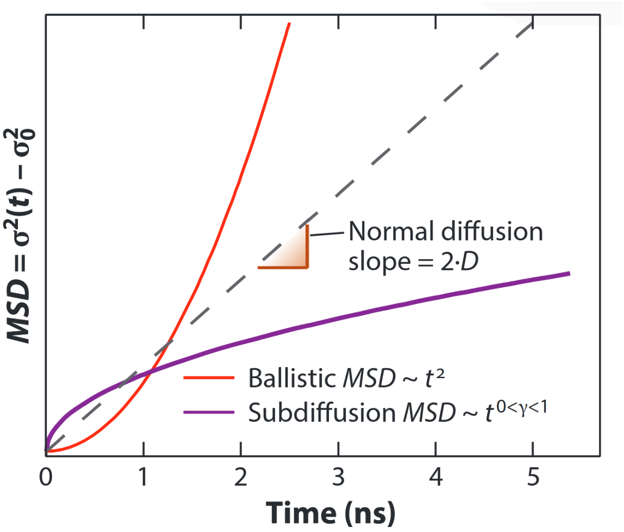

Figure 25. Deviations from normal diffusive behavior can be revealed through MSD analysis in time [6]

3.3 Auger Non-Radiative Recombination in NCs Films

The relaxation of photoexcited charges in semiconductor NCs exhibits a strong power dependence on a sub-ns timescale. As the pump power increases—thus increasing fluence—the normalized amplitude relaxation gets faster, due the presence of Auger recombination. In both bulk and nanostructured semiconductors, electron and hole pairs can recombine radiatively (emitting photons) or non-radiatively. Auger recombination is a non-radiative pathway for recombination, that involves at least three carriers: an exciton plus an additional electron or hole, forming a trion or a biexciton. In this process, an electron and a hole recombine, and instead of emitting a photon the energy is conserved by exciting the third carrier to a higher-lying excited state. In a negative trion, for instance, the exciton recombines non-radiatively while promoting a second electron that becomes a "hot" electron. In a "positive trion" the excess energy is transferred to a hole instead, producing a "hot hole".

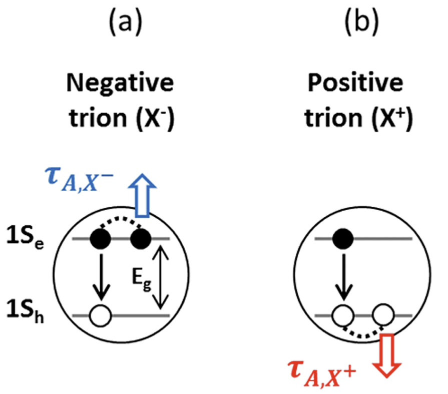

Figure 26. Schematic description of non-radiative Auger recombination of (a) a negative trion (X-), (b) a positive trion (X+) [34]

Quantum confinement in QDs forces a strong overlap of the carrier wavefunctions, leading to strong Coulomb coupling. Therefore, energy transfer from exciton decay to generate a hot electron or hole is highly efficient. Auger recombination dominates under high pump fluences when multiple carriers are generated per QD. We note that the Auger recombination rates in these nanostructures can be tuned through core/shell geometry "design", allowing the use of these dots further improve the efficiency of optoelectronic devices. In fact, Auger processes compete with hot-carrier harvesting—the key goal in many devices—managing these rates is critical for device optimization.

Beyond contributing to faster non-radiative recombination, Auger recombination raises the temperature because the third carrier is excited to a higher laying intraband state and that is followed by rapid thermalization back to the band edge, giving heat to the lattice in the process.

3.4 Distinguishing Electronic and Thermal Signatures in Pump-Probe Spectroscopy of Semiconductor Nanocrystal films

People often overlook thermal effects in optical spectroscopy of semiconductor nanomaterials. Yet these effects are critical for correctly interpreting spectroscopy data. In this section of the manuscript, we pinpoint the signs of transient photoinduced heating in pump-probe measurements of colloidal semiconductor nanocrystal films. We show that lattice heating—wheather from excitation above the bandgap or from high fluences—produces a temperature-driven transient signal that affects three aspects of pump-probe experiments: the transient spectra, the relaxation kinetics and the spatiotemporal carrier diffusivity. These thermal signatures appear universally across different NC cores, but we focus specifically on both CdSe and PbS QD films as they are among the most studied and used in NC-based optoelectronic devices [35].

Accurate disentangling of these transient processes is key to improve energy-conversion efficiencies. Pump–probe spectroscopy at visible wavelengths has been used as go-to tool for mapping excited state dynamics for a long time[36,37], and in more recent years, spatiotemporally resolved variants have proven to be valuable non-invasive alternative windows into carrier diffusion [38,39]. These methods rely on properly linking each transient signal to the right species. In this section we will show that laser-driven heating can generate transient spectral features in semiconductor nanocrystal films even though pump-probe signals are usually credited to electronic energy carriers (i.e., electrons, holes, excitons)[29,40–43]. Such photoinduced heating can arise through several paths including above-bangap excitation followed by lattice cooling, and non-radiative paths such as Auger-mediated heating [6,35,44–46]. As briefly explained in Chapter 1, from the physical point of view the thermal changes in optical absorption and reflection spectra can be explained by looking at phenomena like thermal expansion and electron-phonon coupling[23,41,47]. We have already mentioned that temperature rise in semiconductors typically causes a slight red-shift and broadening of electronic resonances [23], leading to maximum spectral change near the corresponding peaks of the ground-state spectrum [41,42,48,49]. That overlap blurs the line between charge-related and heat-related signals. Hence, further study is essential to better distinguish the fingerprints of transient heating in pump-probe data, to control them experimentally and to extend such knowledge to more materials. Being able to provide this precise distinction is especially important in colloidal semiconductors NC solids where the confinement enhances Auger processes [35,50] and ligands often slow down heat dissipation due to their poor thermal conductivity [51]. In this Chapter, we show how we can probe heat-induced effects on three fronts: transient spectra, decay kinetics and spatiotemporally resolved carrier diffusivity measurement. We demonstrate that differential spectra heating closely resembles the shape and magnitude of the ground state bleach associated with excited charge carriers in transient reflection measurements. We correlated spatially-resolved transient reflection spectroscopy with AFM characterization to show that heat transport produces long-lived relaxation kinetics that are related to the film thickness. Through our pump-probe experiments, we also noted an anomalous excitation wavelength dependence: higher-energy excitation appears to slow transport, consistent with a sizable, slowly spreading thermal profile after hot-carrier cooling. All these results show how important it is to consider thermal artifacts in pump-probe spectroscopy, so we discuss how they can be tracked and mitigated.

3.4.1 Spectral contributions of transient heating

Throughout this section we consider films of colloidal CdSe (bandgap around 635 nm) and PbS (bandgap around 990 nm) quantum dots (Figure 27a,b) and we first show how heat can appear in pump-probe signals in the visible range of wavelengths.

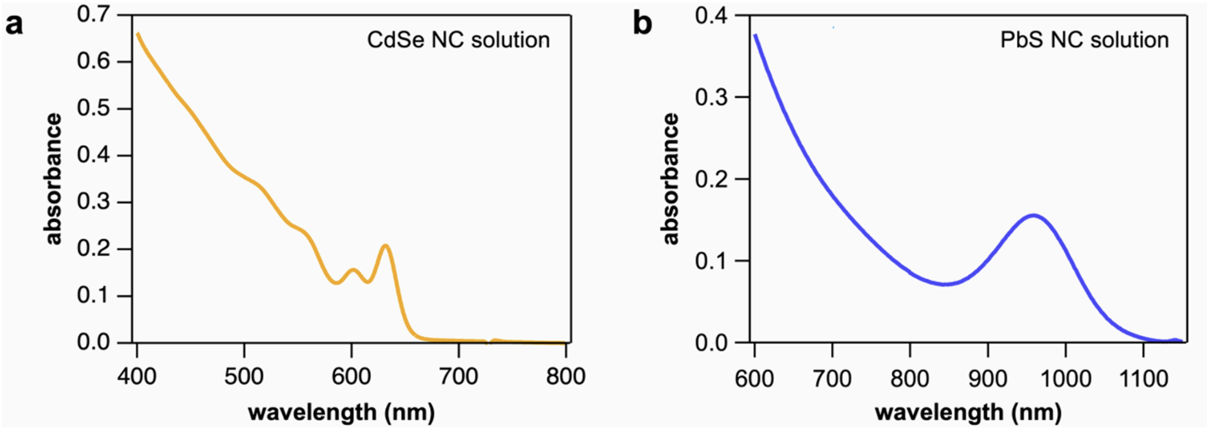

Figure 27. Absorption spectra of colloidal nanocrystal solutions. (a) CdSe nanocrystals with oleate ligands in toluene. (b) PbS nanocrystals with oleate ligands in toluene.

A research engineer at the institute prepared all the samples. A glass coverslip is spin-coated with a CdSe ink. To prepare the ink, 1 mL of CdSe solution is added to an exchange solution (30 mg $HgCl_2$ + 2 ml mercaptoethanol + 18 ml DMF). The solution is vortex-stirred and then sonicated for 3 minutes. Toluene is added and centrifuged. This step precipitates the QDs, then the supernatant is removed. The product is dried with N_2 and dispersed in 300 µl of DMF. The suspension is again sonicated and centrifuged. Before spin-coating, remaining aggregates are removed with mini-vortex and mini centrifuge.

To quantify how heating alters the spectrum (see Chapter 1), we measure the ground-state reflectance contrast spectrum R of the NC films versus the temperature T in steady state conditions (Figure 25 c,d) and compute the room-temperature-referenced change (Figure 28 e,f): $\Delta R/R_{thermal}[R(T_0 + \Delta T) - R(T_0)]/R(T_0)$, where $T_0 = 20\,°C$. The temperature increase produces a small redshift and broadening of the ground state spectral features (Figure 28 c,d). Accordingly, $\Delta R/R_{thermal}$ peaks (Figure 25 e,f) near the electronic resonances (Figure 28 a,b). This is seen clearest in the case of the CdSe NC film, whose band gap transition lies in the measured window (Figure 25a,c). At the largest peak—corresponding to the band gap transition of CdSe NCs—the heating-induced reflectance slope is around $d(\Delta R/R)/dT = -8 \times 10^{-4}\,K^{-1}$ [47]. The PbS NCs show a similar but broader response at visible wavelengths (above its band edge), so its temperature signature is less sharp and weaker (Figure 1b,d,f). Its maximum slope is only $d(\Delta R/R)/dT = -2 \times 10^{-4}\,K^{-1}$. Crucially, these differential temperature spectra strongly mimic standard transient reflection/absorption traces. To test this connection, we collected transient reflection spectra from the same films (Figure 28 g). The signal initially decays with few-ns half-life has an initial decay component with a few-ns half-life [36,52,53] while the spectrum red-shifts and narrows (Figure 28g, inset). In PbS, broader features dominate (Figure 28h) since its band gap lies in the near-infrared, outside the measured window. Here the decay half-life spans tens of nanoseconds, matching carrier relaxation in carrier relaxation for PbS NCs with ethanethiol ligands (Figure 28h, inset) [54]. Strikingly, both transient spectra match their respective temperature-induced difference spectra in Figure 28e,f.

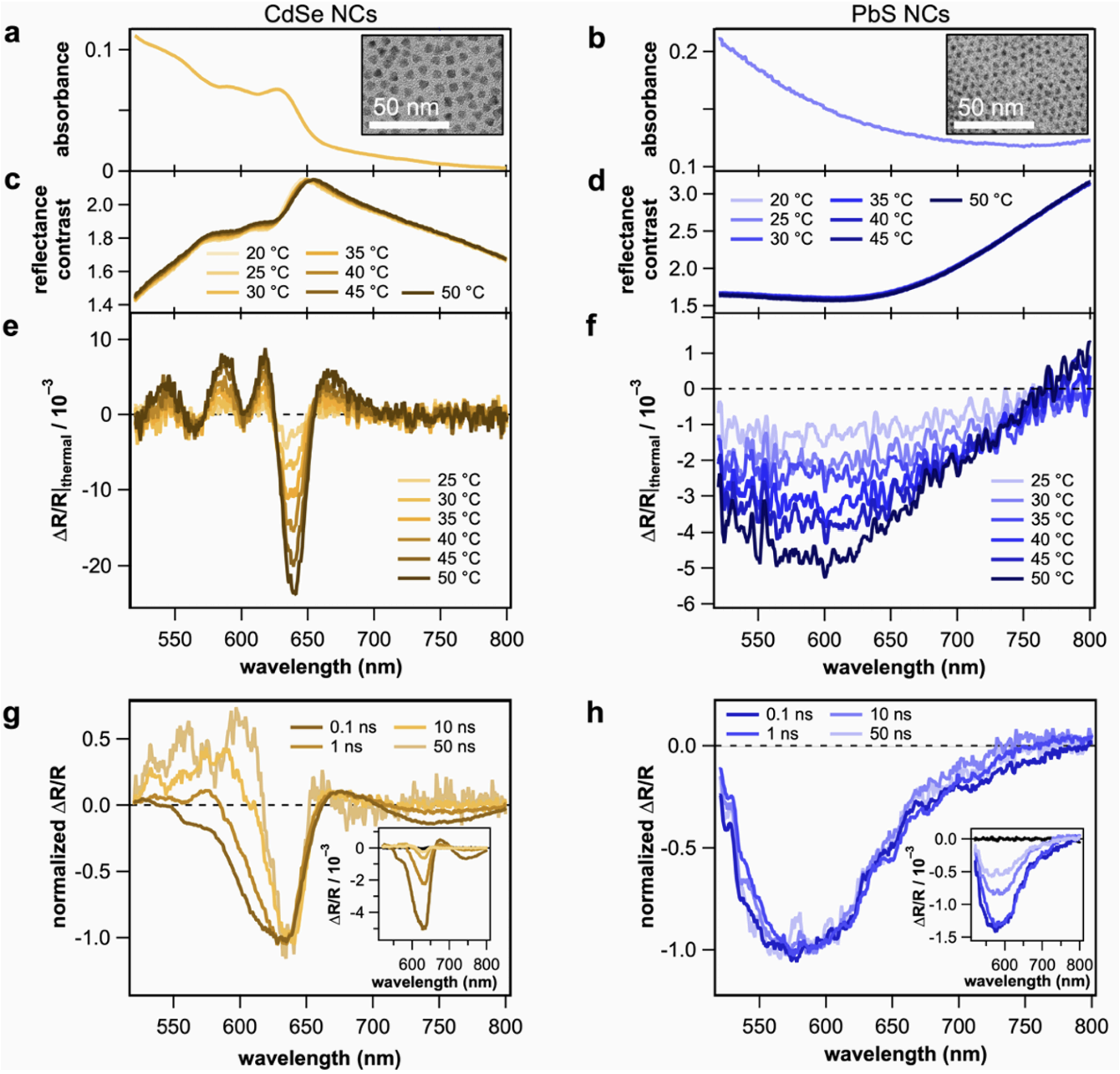

Figure 28. Spectral signatures of heating and electronic excitation in nanocrystal films. (a,b) Steady-state absorption spectrum of (a) CdSe and (b) PbS nanocrystal films at 20°C. Insets: Transmission electron micrographs of nanocrystal samples with native ligands. (c,d) Temperature-dependent reflectance contrast spectra of (b) CdSe and (c) PbS nanocrystal films. (e,f) Steady-state change in reflection spectrum as a function of temperature relative to 20°C for (e) CdSe and (f) PbS nanocrystal films. (g,h) Pump-probe transient reflection spectra of (g) CdSe and (h) PbS nanocrystal films after excitation with 405 nm light pulses at the indicated time delays, normalized to the peak amplitudes for comparison of spectral shapes over time.The pump fluence was about 100Jcm-2, resulting in estimated temperature rise of about 1 and 4K for the CdSe and PbS nanocrystal films, respectively

The idea is that photoexcited transient spectra can contain both electronic and thermal contributions. Assigning pump-probe signals to excited-state charge carriers is well established, at least for times shorter than the band-edge lifetime [36,55,56]. Yet a share of the trace can arise from transient heating. For CdSe and PbS NCs, the reflection spectra resembles the temperature-induced differential spectra for delays that exceed 10 ns. In this time window we expect that many electronic carriers have already relaxed. Because heat diffuses slowly (see below), the rapid carrier decay reveals a long lived transient heating signal. Thus, the early signal is charge-dominated, while the late signal is heat-dominated. We just qualitatively compare the shapes of the electronic and thermal transient signals, as the steady-state temperature dependent spectra were obtained with a macroscopic spot size and incoherent lamp; on the other hand the pump–probe data was collected with a microscopic laser spot. Another aspect to be taken into account is that pump–probe measurements are sensitive to focal position and thickness of the film—both can change the sign of the stroboSCAT signal [29,57]. Typical electronic bleach amplitudes in NC and other thin films are ~10^{-3}. As we measure the $d(\Delta R/R)/dT$, even a change in temperature of 1 K can supply a considerable heat contribution to the transient reflection signal, considering that our detection limit is about an order of magnitude lower than this. In this work we do not get a direct measure of the absolute temperature change, but we can estimate that excitation above the band gap at 405 nm at our fluences should heat the CdSe and PbS by roughly 1 K and 4 K, respectively (Figure 29)

We have previously stated that lattice heating can be caused by both above-band-edge excitation or by Auger non-radiative recombinations—which we refer to as Auger-mediated heating. To roughly estimate Auger-mediated heating, compute the fraction of dots that absorb two or more photons ($P_{N\geq}$ 2) in the excited volume. We assume unity Auger efficiency; the released energy equals E_g; all of it converts to heat; and electrons and holes warm the lattice, whose heat capacity dominates. QDs absorbing ≥ 2 photons are treated as if they took exactly two, for simplicity. We first find the mean absorbed photon count per dot, $\langle N\rangle = J_0(1 - e^{-\alpha L})/E_{ph} nL$—where n is the NC number density per unit volume, then use a Poisson distibution to extract P_N. The Auger energy density is $U_{Auger} = E_g P_{N\geq 2n}$, yielding a temperature jump $\Delta T_{Auger} = U_{Auger}/C$.

From this model we expect Auger heating to add ≈0.5 K for CdSe and ≈0.02 K for PbS under the Figure 29 conditions. These values are compatible with earlier electron-diffraction work by Guzelturk at al [35].

	E_g (eV)	E_{ph} (eV)	J_0 at peak (μJ cm^{-2})	Fraction of energy exceeding bandgap, $\frac{E_{ph} - E_g}{E_g}$	α^{-1} (nm)	U_{excess} at peak (J m^{-3})	C (J m^{-3} K^{-1})	ΔT_{ph} at peak (K)	$\langle N \rangle$	$P_{N\geq2}$	n (nm^{-3})	U_{Auger} at peak (J m^{-3})	ΔT_{Auger} at peak (K)
CdSe 405 nm pump	1.94	3.06 (405 nm)	100	0.37	5×10^2	3×10^6	2.8×10^6	1	0.9	0.22	5×10^{-3}	1.5×10^6	0.5
PbS 405 nm pump	1.25	3.06 (405 nm)	100	0.59	3×10^2	2×10^6	2.2×10^6	4	0.2	0.02	3×10^{-2}	5×10^5	0.02

Figure 29. Estimated temperature jump due to photoexcited hot carrier cooling in Figure 28

3.4.2 Thickness dependence of heat dissipation timescale

In this subsection we show how thickness-dependent relaxation rates in stroboSCAT experiments can be used to disentangle charge and thermal carriers. When we assume that the substrate is not electronically active and the film is multilayer—so that the hopping transport is not affected—the charge carrier recombination can be thought as independent by the thickness of the NC film [58]. Instead, heat diffuses through the substrate and its characteristic decay time will grow as the film gets thicker. We have used AFM to finely measure the local film thickness in several spots (Figure 28) and later we correlated these measures with the observed relaxation decays observed when stroboSCAT was performed in the same spots.

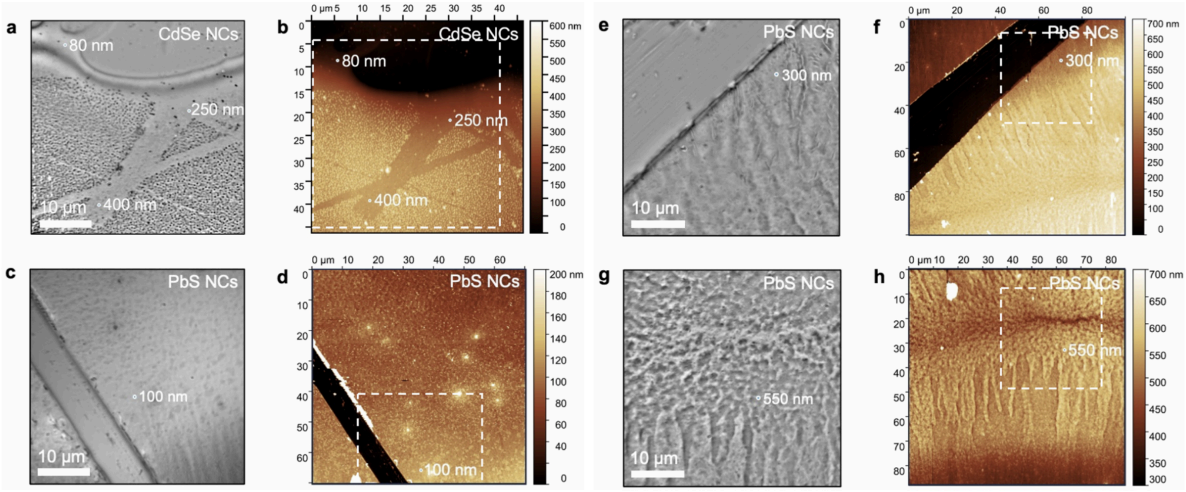

Figure 30. Correlated AFM and optical mapping of CdSe and PbS NC films for thickness dependence. (a) Optical reference image and (b) AFM of CdSe NC film, where regions with local thicknesses of 80, 250 and 400 nm are indicated. (c-h) Optical reflectance images (a,c,e,g) and AFM (b,d,f,h) collected for the same regions of a PbS NC film, with indicated locations for thicknesses of 100 nm (c,d), 300 nm (e,f) and 550 nm (g,h). The stroboSCAT measurements locations are marked with small circles

In Figure 32 we have compared several transient reflection time traces for different thicknesses in both CdSe and PbS; we have also observed the decays at different fluences, in near-band gap and above-band gap conditions. The time window we focus on goes from tens to hundreds of nanoseconds, where pump-probe spectra mimic the temperature-difference curves noted earlier and slower transport shows up, as detailed below. For both types of NCs, in near-gap pump condition, low fluence produces decay curves that do not vary with thickness (Figure 32a,b). Instead when we excite far above the gap with 405 nm light, the decay grows progressively longer as the film gets thicker (Figure 32c,d). The trend is stronger for PbS, since 405 nm sits even higher above its band gap than it does for CdSe. Exciting the sample near the gap but at high fluence shows a similar thickness effect, again showing relaxation in thicker films (Figure 32e,f). Such behavior is due to temperature-induced transient reflectance change caused by Auger-mediated heating and photoexcitation of hot carriers dominating at late-time. In Figure 31 it is possible to find our estimated temperature jumps under each set of conditions.

	E_g (eV)	E_{ph} (eV)	J_0 at 2σ (μJ cm^{-2})	Fraction of energy exceeding bandgap $\frac{E_{ph}-E_g}{E_g}$	α^{-1} (nm)	U_{excess} at 1σ (J m^{-3})	C (J m^{-3} K^{-1})	ΔT_{ph} at 1σ (K)	$\langle N\rangle$	$P_{N\geq2}$	n (nm^{-3})	U_{Auger} at 1σ (J m^{-3})	ΔT_{Auger} at 1σ (K)
CdSe 405 nm pump	1.95	3.06 (405 nm)	20	0.36	5×10^2	6×10^5	2.8×10^6	0.2	0.2	0.02	5×10^{-3}	3×10^4	0.05
CdSe 635 nm pump		1.95 (635 nm)	7	0	1×10^2	≈0		≈0	0.06	0.002		1×10^4	0.005
			1000			≈0		≈0	8	≈1		6×10^6	2.5
PbS 405 nm pump	1.25	3.06 (405 nm)	200	0.59	3×10^2	1×10^7	2.2×10^6	8	0.35	0.05	3×10^{-2}	1×10^6	0.6
PbS 775 nm pump		1.60 (775 nm)	24	0.22	8×10^2	3×10^5		0.1	0.09	0.004		1×10^5	0.04
			2000			2×10^7		10	3	0.82		2×10^7	10

Figure 31. Estimated temperature jump due to photoexcited hot carrier cooling in Figure 32

To test the time scale of heat dissipation through the NC film and the substrate, we assume the dissipation to be limited in between two extreme regimes: diffusion-controlled and interface-controlled dissipation. One metric that can be used to evaluate the regime of thermal dissipation is the ratio of interfacial to bulk thermal conductance hL/k, where h is the film–substrate interface conductance, L is the film thickness and k is the thermal conductivity. The NC film is physically in contact with the glass substrate through the ligand layer and we assume a layer conductance of $10\,MW\,m^{-2}K^{-1}$ based on polystyrene film-sapphire studies as a reference for organic-film/glass interfaces [59]. Our film thickness L spans 80 to 550 nm overall. Using an effective medium approximation model, we take the NC film thermal conductivity k around $0.2 - 0.3\, W\, m^{-2}\, K^{-1}$. This places hL/k in the range of 1–12. Thus the cooling kinetics falls between pure interface transfer and pure bulk diffusion. We estimate characteristic times in both limits, knowing that the real answer lies in-between. In the interface-limited case, the time constant is τinterface = $\rho C_p L/h$, where ρ is the NC film density, C_p its specific heat capacity, L the thickness of the film, and h the interfacial thermal conductance. If we roughly substitute numbers we get $\tau_{\text{interface}}$ ranges from 50 to 300 ns for NC film thicknesses of 80 to 550 nm. Under diffusion control instead, $\tau_{\text{diff}} = L^2/D$, where D is the thermal diffusivity. Assuming $D = 100\ \text{nm}^2\ \text{ns}^{-1}$, τ_{diff} runs from 100 ns up to 3 µs over the same thickness range.

These calculated times match the late-lime relaxation we observe after above-gap or high fluence pumping. The data then support a scenario in which heat induced via photoexcitation drains into the substrate, dominating after electronic carriers have recombined.

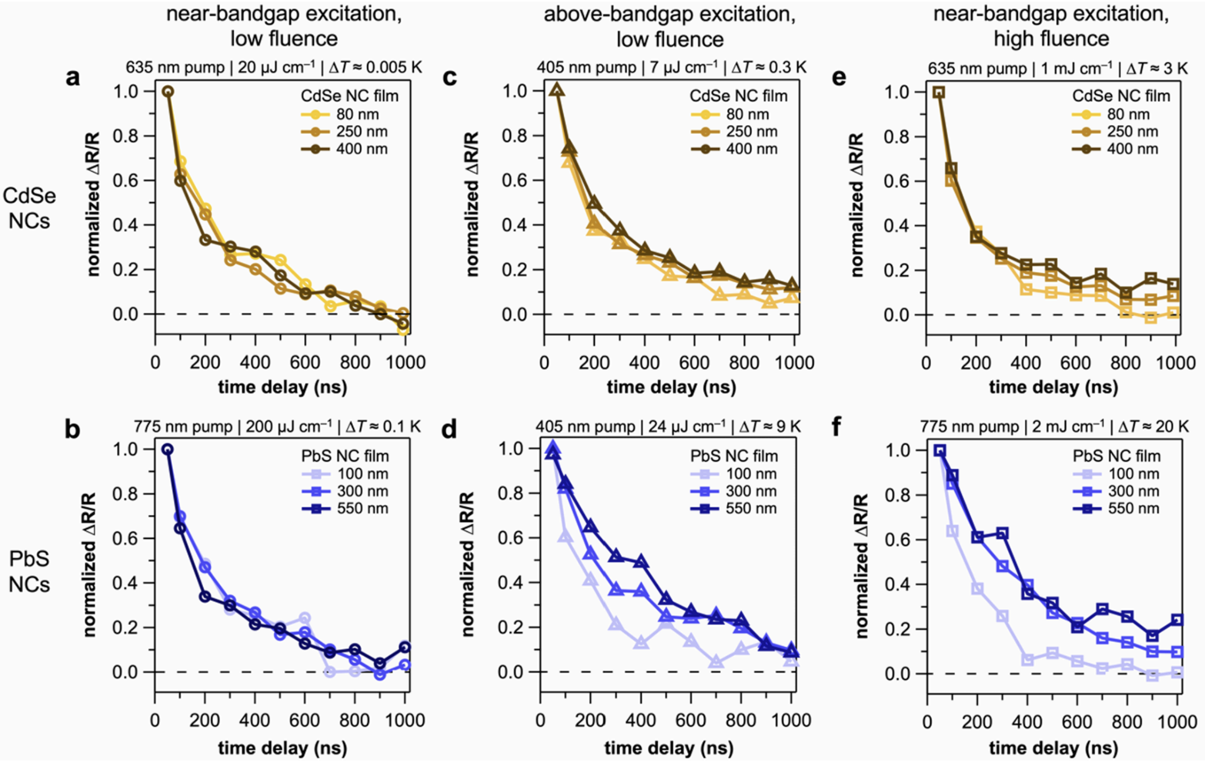

Figure 32. Thickness dependence of heat dissipation timescale. (a-f) Pump–probe relaxation profiles for (a,c,e) CdSe and (b,d,f) PbS nanocrystal films collected in locations of known thickness. We also compared different pump excitations (a,b) with photon energies near the band gap at low fluence, (c,d) with photon energies near the band gap at high fluence (the combinations are indicated for each figure). The estimated temperature increases are detailed in Figure 28

3.4.3 Dual signals in transient microscopy of carrier diffusion

We use stroboSCAT technique (described more in detail in chapter 2) to resolve the carrier diffusion in our NC films [29,60]. Pump-probe techniques such as stroboscopic scattering microscopy had already been adopted to separately track electronic and thermal carrier transport in NC semiconductor assemblies [31,45,61–63]. In Chapter 2 we have described both the stroboSCAT experimental and the standard data analysis workflow. We generate a diffraction limited spot dense of excited energy carriers and by imaging its relative change in reflectance (ΔR/R) we study how it evolves spatiotemporally by probing the carriers with a wide-field probe pulse. (Figure 33a,b). As mentioned earlier in the manuscript, we fit Gaussians to the datasets and follow their standard deviation σ and amplitude as a function of time t to obtain the MSD (Figure 33c,d) and relaxation traces. The first thing that emerged through the experiments is that the choice of the excitation wavelength strongly affects the nature of the observed transport. Indeed, near-band gap photons causes the excitation to spread quickly in the first few nanoseconds, showing subdiffusive mean-squared expansion $\sigma^2(t) - \sigma^2(t_0) \sim t^{\alpha}$ (with $\alpha < 1$), which is commonly related to electronic transport in disordered NC films [10]. Pumping well above the band gap instead produces much slower expansion; at late times—tens to hundreds of nanoseconds, matching the thickness-dependent decay regime in Figure 29—the growth turns diffusive ((linear mean-squared expansion, $\alpha = 1$) with a diffusion coefficient of $1–2 \times 10^2$ nm^2 ns^{-1}

To benchmark these numbers, we need to estimate the film's thermal diffusivity via the Hasselman Johnson Maxwell Euken (HJ-ME) effective medium approximation (EMA) proven for NC solids . In this case, the effective thermal conductivity of the composite medium, k_{eff}, is given by

$$k_{eff} = k_{ligand} \frac{\frac{k_{NC}}{k_{ligand}} + \frac{2k_{NC}}{rh_{NC-ligand}} + 2 + 2\phi_{NC}\left(\frac{k_{NC}}{k_{ligand}} - \frac{k_{NC}}{rh_{NC-ligand}} - 1\right)}{\frac{k_{NC}}{k_{ligand}} + \frac{2k_{NC}}{rh_{NC-ligand}} + 2 - \phi_{NC}\left(\frac{k_{NC}}{k_{ligand}} - \frac{k_{NC}}{rh_{NC-ligand}} - 1\right)} \tag{4.3}$$

where k_{ligand} is the ligand thermal conductivity, k_{NC} the NC core thermal conductivity, r the NC core radius, $h_{NC-ligand}$ the NC–ligand interfacial conductance, and ϕ_{NC} the NC volume fraction. We calculate the effective diffusivity of the medium as $D_{eff} = k_{eff} / \rho C_p$, where ρ is the density and C_P the mass-weighted average specific heat capacity results to be appropriate for NC arrays as shown by Malen and coworkers. Malen and coworkers showed that, specifically, C_p.[10] Using bulk values and

$h_{NC-ligand} = 200\, W\, m^{-2} K^{-1}$ typical for dense thiolate shells plus FCC packing with 0.5 nm core-core gaps, we get for CdSe $\rho = 3900\, kg\, m^{-3}$, $C_p = 720\, J\, kg^{-1}\, K^{-1}$, and ϕ_{NC}= 0.58, and for the PbS NC film $\rho = 4100\, kg\, m^{-3}$and $C_p = 520\, J\, kg^{-1} K^{-1}$, and ϕ_{NC} = 0.47. Both sets point to $D_{eff} \approx 100\, nm^2 ns^{-1}$.

The late time D we measure therefore aligns with the predicted thermal diffusivity ($100\, nm^2 ns^{-1}$) and earlier reports for similar films [31,51,64,65]. Being the features common to both the materials under study we understand they come from a common mechanism (Figure 33c,d)

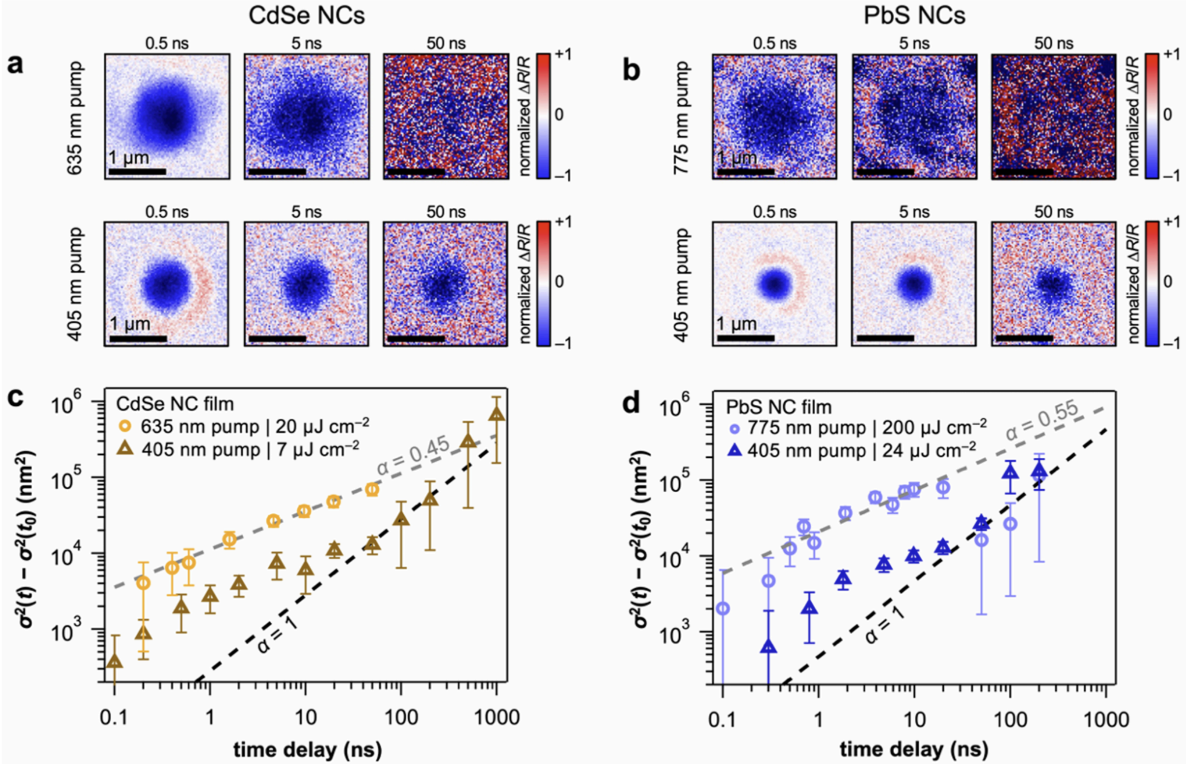

Figure 33. Thermal artifacts in transient microscopy of carrier diffusion. (a,b) stroboSCAT time series for (a) CdSe and (b) PbS nanocrystal films at the indicated wavelengths and time delays. (c,d) Mean-squared displacement curves for (c) CdSe and (d) PbS nanocrystal films at the indicated pump wavelengths and fluences. The corresponding estimated temperature rises are indicated in Figure 31. All CdSe data sets were collected using probe pulses with a wavelength as of 775 nm. All PbS data sets were collected using probe pulses with a wavelength of 635 nm.

The pump-wavelength dependent carrier diffusion we observe can be attributed to photoinduced heating participating in the signal. Near-gap, low-fluence pumping barely warms the lattice (Figure 34), so the signal tracks pure electronic transport until carriers vanish. On the other end, above-gap pumping produces more hot carriers which heat up the lattice (Figure 34), which means that the transient signal will arise from both electronic and thermal contributions.

	E_g (eV)	E_{ph} (eV)	J_0 at 2σ (μJ cm^{-2})	Fraction of energy exceeding bandgap $\frac{E_{ph} - E_g}{E_g}$	α^{-1} (nm)	U_{excess} at 1σ (J m^{-3})	C (J m^{-3} K^{-1})	ΔT_{ph} at 1σ (K)	$\langle N \rangle$	$P_{N\geq2}$	n (nm^{-3})	U_{Auger} at 1σ (J m^{-3})	ΔT_{Auger} at 1σ (K)
CdSe 405 nm pump	1.95	3.06 (405 nm)	20	0.36	5×10^2	6×10^5	2.8×10^6	0.2	0.2	0.02	5×10^{-3}	3×10^4	0.05
CdSe 635 nm pump		1.95 (635 nm)	7	≈0	1×10^2	≈0		≈0	0.06	0.002		1×10^4	0.005
PbS 405 nm pump	1.25	3.06 (405 nm)	200	0.59	3×10^2	1×10^7	2.2×10^6	8	0.35	0.05	3×10^{-2}	1×10^6	0.6
PbS 775 nm pump		1.60 (775 nm)	24	0.22	8×10^2	3×10^5		0.1	0.09	0.004		1×10^5	0.04

Figure 34. Estimated temperature jump due to photoexcited hot carrier cooling in Figure 33

The profile we measure with stroboSCAT results from the overlapping of both components, each spreading with its own diffusivity; thus the effective rate of diffusion of the signal lies in between the two true populations. Once the electronic carrier-induced change in the transient reflectance signal starts to fade the experimental curves mainly report heat flow. To illustrate this, we build synthetic profiles spanning all-electronic to all-thermal starting ratios (Figure 35 a-c). By summing the generated profiles (Figure 35 d) and fitting them to a single Gaussian we get synthetic transport curves (Figure 35 f) and decay traces (Figure 35 e) that closely mimic the experimental results. A dramatic shrinkage of the squared variance appears when a weak but long-lived thermal tail outlives the fast electronic front (Figure 35 f); we reproduce this by pumping at the gap with enough fluence to trigger Auger heating and observe a milder version for low-fluence above-gap pumping.

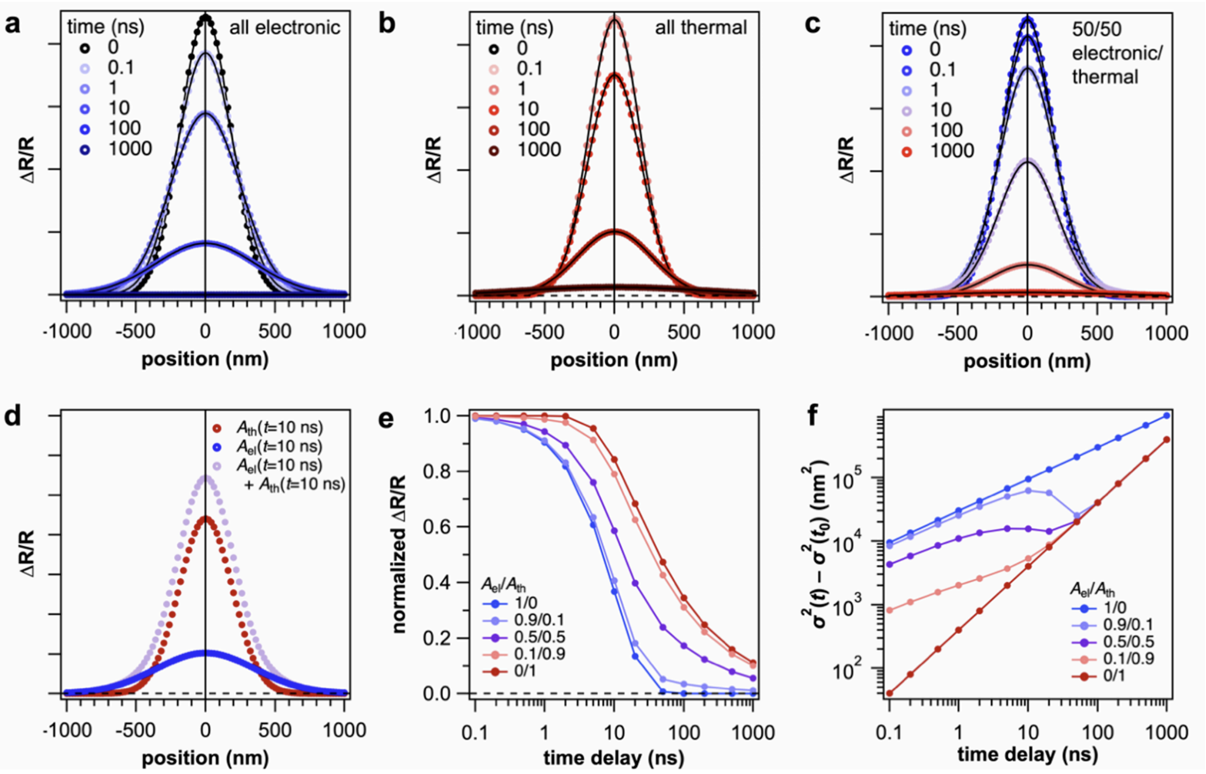

Figure 35. Simulation of effect of two carrier populations underlying carrier diffusion measurements. Simulated ΔR/R profiles for (a) electronic carriers only, (b) transient thermal signal only, and (c) equal initial amplitudes for both electronic and thermal signals. (d) Case with 50/50 electronic/thermal initial amplitudes, showing the effect of underlying thermal and electronic carrier profiles. (e) Extracted amplitude time trace and (f) mean-squared expansion curve obtained by fitting profiles to a single Gaussian function. The indicated A0,el and A0,th are the input initial amplitudes of the electronic and thermal components. The electronic decay is a single exponential within 10 ns, the thermal signal has a 50 ns with half-life power-law tail. The purely-electronic reference is subdiffusive with α=0.5 while the thermal profile is diffusive with Dth=200 nm2 ns-1.

Here the broad, short-lived charge carriers recombine, revealing the slowly diffusing heat profile beneath it (Figure 35d) [39,66,67]. These conditions are especially interesting as they show that electronic and thermal transport regimes can be distinguished with a single measurement (Figure 36). Another interesting note we can extrapolate from these results is that the time-dependent thermoelectric behaviour of the NC films would require further studies for its important performance implications, since the time-dependent charge carrier diffusivity and thermal diffusivity in these samples have a ratio of ≈100 at 100 ps that falls to <10 approaching 100 ns.

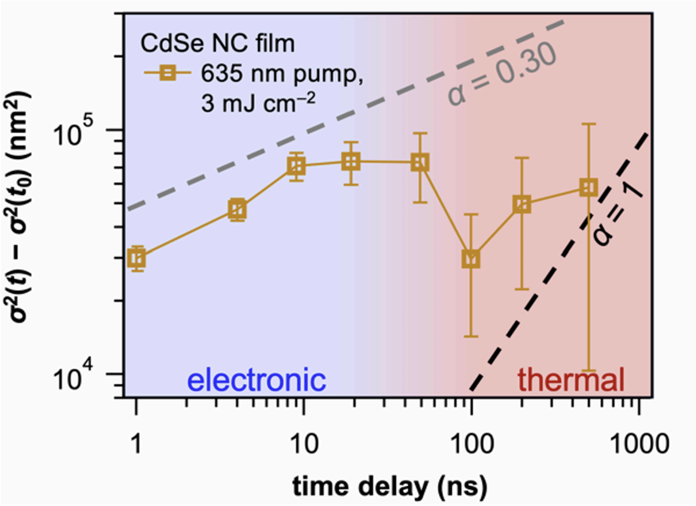

Figure 36. Mean-squared displacement curve at high fluence band gap excitation. Mean-squared expansion curve of a CdSe NC film excited near the band gap with 635 nm light pulses and probed at 775 nm. The pump fluence was 3 mJ cm-2 per pulse—much higher than the fluence of 20J cm-2 used for the data presented in Figure 30. The dashed lines are the references for subdiffusive (grey line with = 0.30) and diffusive regimes (black line with =1).

3.4.4 Implications of dual electronic and thermal signatures

Our findings have proven to be common to both CdSe and PbS as previously anticipated, but it would be reasonable to expect similar mixed regimes due to electronic and thermal processes in other pump-probe studies of nanomaterials. In fact, phenomena like photoinduced heating and temperature-dependent spectral shifts are quite general among these classes of materials. Yet the relative contributions of the electronic and heat carriers will be varying according to the properties of each material. Although we worked in transient reflection, one should expect similar features in transient absorption (with different weighting) since the two are lined through Kramers-Kronig relations. Our emphasis has been on transients but the temperature induced spectral changes can be observed in steady-state pump–probe measurements as well.Usually the pump–probe spectra and decay curves of NC semiconductors are solely associated with electronic events, ignoring that heat can lead to misinterpretations. Thus we foresee heat as an alternative explanation for phenomena showing slow transport and long-lived signals, which are usually labeled as trap-limited. Yet thermal relaxation can share those timescales and non-exponential decays, so one must avoid mixing them up. Some of our results could be fitted by trapping, but traits like longer lifetimes in thicker films and late-time transport equal to the thermal diffusivity point clearly to heat. Both trapping and heating should be at least weighted as parallel explanations for pump–probe behavior. In this sense, in this study we offer practical tips for spotting and tuning the electronic-thermal balance in pump–probe work. Three factors boost the transient heat term: (1) above-band gap pumping that provokes lattice heating; (2) high fluences that leads to Auger heating—worsen by the high confinement offered by

NCs; (3) thick films that hinder heat flow to the substrate. Depending on the goal, one can suppress these conditions to isolate charges or maximize them to probe heat. An additional degree of freedom in the design of NC based devices could be the leveraging of selected substrates to tune the heat losses. Pump–probe techniques like transient absorption or reflection allows us to access nanoscale thermal transport properties of NC assemblies, which are important for their implementation in all kinds of devices either to generate heat on purpose or as a byproduct. Here we measured local thermal diffusivity and cooling times in the two NC films directly, a task normally requiring a transducer layer and lacking spatial resolution [51]. This opens the door to repurposing standard visible pump-probe setups, usually aimed at charge motion, for thermal studies too, having a method that tracks both charge and heat transport.

3.4.5 Simulation of Overlapping Electronic and Thermal Contributions to Carrier Diffusion Measurements

In this section we provide some insights, the methods and reasoning behind Figure 35 of the previous paragraph. We generate synthetic data and perform the usual analysis to show the effect of two carrier populations on the stroboSCAT transient-reflection profile. We imagine a Gaussian photoexcitation that creates both a charge-carrier population and a transient temperature rise, each starting with the same spot size. We write the measured signal $\Delta R/R$, as the weighted sum of two normalized Gaussians in position x and time t::

$$\frac{\Delta R}{R}(x,t) \;=\; A_{el}(t)\,\frac{exp[-\frac{x^2}{2\sigma_{el}(t)}]}{\sqrt{2\pi\sigma^2_{el}(t)}} + A_{th}(t)\,\frac{exp[-\frac{x^2}{2\sigma_{th}(t)}]}{\sqrt{2\pi\sigma^2_{th}(t)}}$$

4.3

where A_{el} and A_{th} are the time-dependent amplitudes of the electronic and thermal components, respectively, and σ_{el} and σ_{el} are the time-dependent standard deviations of the Gaussian profiles for the electronic and thermal components, respectively. This formulation is meant to be an empirical representation of the linear relative reflectance change broken down into differential components for each transient species,

$$\frac{\Delta R}{R}(x,t) = \frac{1}{R_0}\left[\left(\frac{\partial R}{\partial T}\right)\Delta T(x,t) + \sum_i\left[\left(\frac{\partial R}{\partial n_i}\right)\Delta n_i(x,t)\right]\right] \tag{4.3}$$

where T is temperature and n_i is the carrier density in state *i*. To get realistic parameters we let the electronic amplitude decay as a single exponential with a 10 ns lifetime. Then we assign a 50 nm half-life plus a power-law tail to the thermal dissipation to capture slow, substrate-limited cooling. We assume charge carriers undergo subdiffusive transport, $\sigma^2_{el} = \sigma^2_0 + Kt^{\alpha}$, where K is an empirical prefactor taken to be $32,000\ nm^2 ns^{-1/2}$ such that the mean-squared expansion is $1\times10^4\ nm^2$ at 0.1 ns for $\alpha = 0.5$ to approximate the CdSe NC data after bandgap excitation in Figure 3. The thermal signal instead, is assigned diffusive transport with $\sigma^2_{th} = \sigma^2_0 + 2D_{th}t$ with $D_{th} = 200\ nm^2 ns^{-1}$ to reflect the diffusivity found at late times. The common width is $\sigma_0 = 180\ nm$ to approximate the real data. Noise-free synthetic traces are generated for three starting amplitude ratios: all-electronic $A_{o,el} = 1$ and $A_{o,th} = 0$ (Figure 35a, "all electronic"); $A_{o,el} = 0$ and $A_{o,th} = 1$ (Figure 35b, "all thermal"); $A_{o,el} = A_{o,th} = 0.5$ (Figure 35c, "50/50 electronic/thermal"). Each set is fitted at every delay to a single Gaussian to extract decay curves (Figure 35d) and mean-squared expansion curves (Figure 35e). The pure electronic and pure thermal references reproduce the fast, sub-diffusive carrier motion and slow, diffusive heat flow. When both species contribute, the extracted mean-squared expansion curve lies between the two limits and matches the thermal transport curve at late times when the slowly-decaying thermal signal dominates the signal amplitude. We observe an apparent contraction of the mean-squared expansion curve as the electronic profile decays, which is what the experimental carrier diffusion data looks like under different pump conditions. One might try to fit the data to a sum of two Gaussians to separate the species, but if they are overlapping with a common center and similar widths they cannot be uniquely disentangled. In principle one component might be constrained—for instance, the thermal diffusivity to its late-time value—helping the other component track electronic motion while its amplitude stays significant. The use of PCA or machine learning could make this process easier in the future.

Chapter 4

Energy Transport in Transition Metal Dichalcogenides

4.1 Overview on Transition Metal Dichalcogenides for Optoelectronics

Transition metal dichalcogenides (TMDs) such as MoS_2, $MoSe_2$, WS_2 and WSe_2 have been paving the way for the next generation materials for optoelectronic device applications. Their appeal comes from their layered structure that can be reduced to atomically thin monolayers through mechanical exfoliation techniques due to weak interactions between the layers. Approaching low-dimensionality the material transitions from indirect to direct band gap, giving tunable and strong optical absorption due to strong excitonic effects [11]. The absence of dangling bonds makes this class of material chemically stable and allows less defective interfaces in heterostructures which makes them even more promising for efficient device design [68]. In contrast to graphene which lacks a bandgap, TMDs have a gap that can be in the visible to near-infrared range.

From the engineering standpoint, their atomically thin nature can be leveraged to get active layers highly sensitive to strain, electric fields and dielectric environment—different ways to engineer their optical and transport properties and functionalities [69] [70]. Studies show that their optical features can be tuned to allow charge conduction, paving the way for TMD-based field-effect transistors (FETs), which is a needed step towards the 2D semiconductor integration into electronic devices. When working towards device integration, the presence of interfaces between materials and interface-related effects strongly influences the behavior of excitons, free carriers and thermal propagation and thus the device efficiency. Techniques such as X-ray photoemission usually lack the spatial resolution to investigate interface-related effects; other near-field microscopy techniques such as scanning tunneling microscopy or electron microscopy do not allow mesoscale time range of observation. Mastrippolito et al. have shown that high-resolution soft X-ray photoemission spectroscopy can be used to characterize the energy landscape of TMDC-based devices, even in operando conditions [71].

Transient reflectance microscopy on the other hand measures the dynamics of energy carriers with sub-micrometer spatial resolution and nanosecond time resolution. In the following sections we will describe what makes these materials special, its structure and its main properties, focusing specifically on WSe_2. Viscoelastic transfer of WSe_2 on glass will be introduced together with the materials optical and electronic properties useful for energy carrier dynamics study.

4.1.2. Crystal structure and Chemistry and Preparation Methods

TMDs respond to the general formula MX_2, where M is the transition metal (i.e. W, Mo) and the X is the chalcogen (i.e. Se, S). Each layer consists of a hexagonally packed plane of transition metal atoms sandwiched between chalcogen atoms, forming a trilayer X-M-X. Each M atom is bounded to six X atoms in a trigonal geometry (Fig. 37).

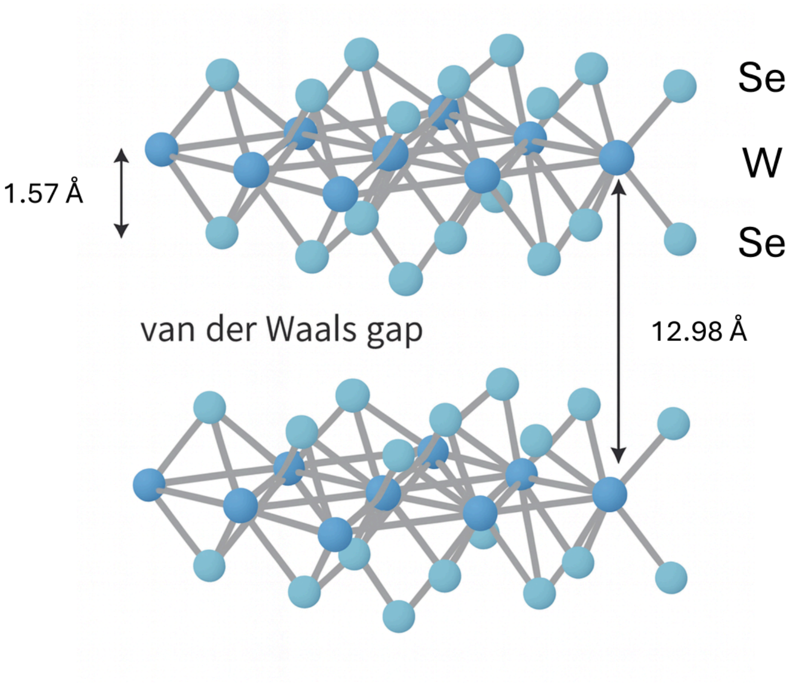

Figure 37. Simple representation of WSe_2 layer structure

This work focuses on tungsten diselenide (WSe_2), which is one of the most studied TMDs; its properties though can be extended to the whole material family as they all possess similar optoelectronic properties.

Mechanical exfoliation is one of the most common techniques used to produce WSe_2 flakes from bulk crystals [72]. These are layered materials, which means their bulk structure is formed by a large number of layers kept together by van der Waals interactions. These bonds are generally known as “weak interactions” and allow exfoliation of TMDs crystals down to single layers—which is a consolidated technique firstly introduced to fabricate graphene-based devices. Scotch tape mechanical exfoliation technique is used to produce atomically-thin flakes of material from bulk crystals, which are then transferred on the substrate of interest [72]. In the work described in this Chapter, we use "blue tape" to exfoliate the crystals, then transfer them on PDMS—already positioned on a second glass carrier to ease manipulation. PDMS polymer is chosen because of its viscoelastic properties: it strongly holds on the crystals when pressed against the blue tape and firmly pulled, allowing the separation of the layers. Optical microscope inspection is done to identify flakes of the right thickness and size, then the PDMS is pressed against the final substrate and slowly pulled away so it gently releases the flakes without damaging them (Fig. 38,39). This approach allows deterministic deposition of thin flakes with minimal structural defects, as the blue tape adhesion is not strong enough to break surface atomic bonds; a range of thicknesses down to monolayers can be reached by repeating the mechanical exfoliation procedure several times. It is a slow process—the preferred one for fundamental optical and transport studies like ours—with relatively low throughput but high flake quality and stability. Alternatively, chemical vapor deposition (CVD) has been used since the 1960s to grow bulk crystals by putting together the precursor elements in precise stoichiometric ratios and mixing them with a transport agent. The temperature of the mixture allows controlled crystal growth. Here we only study exfoliated TMDs.

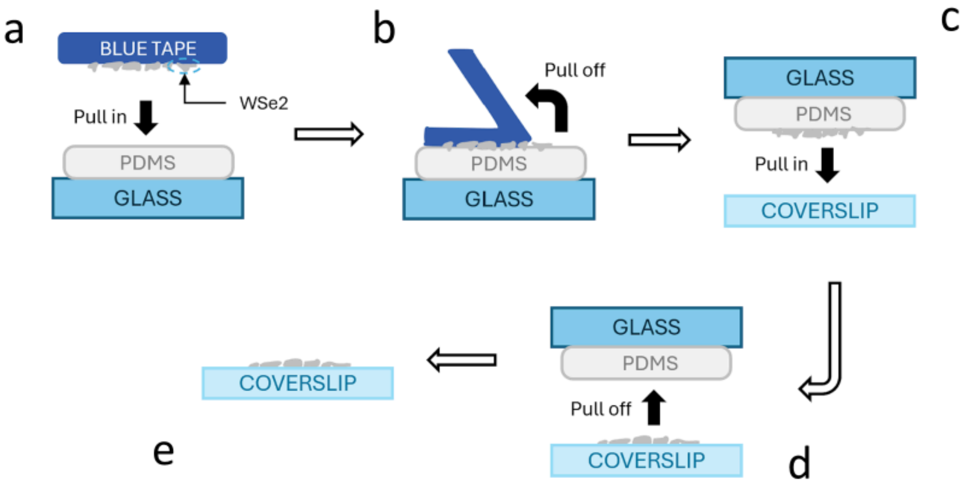

Figure 38. Mechanical exfoliation and viscoelastic transfer process. (a) bulk crystals are exfoliated with the blue-tape and pressed on the PDMS polymer to transfer. (b) the tape is pulled off, leaving the exfoliated flakes on the PDMS support. (c) the selected flake is transferred to the final substrate (glass). (d) the PDMS is pulled off with the help of substrate cooling. (e) exfoliated flakes on glass coverslip ready for analysis.

The flake transfer procedure is done using a micropositioning transfer station to get precise alignment and transfer on substrate. Once the final position is chosen, the substrate is pre-heated and the PDMS carrier is pressed against it to begin the transfer. The sample analysed in this manuscript was obtained by heating the substrate at around 120 °C with a Peltier heater to ease flake adhesion. The PDMS stamp is gradually contacted with the substrate and once pressed, the temperature is gradually lowered. The thermal contraction and the mechanical retraction of the PDMS allow gentle transfer of the flake (Fig. 40 reports a flake before and after the transfer without any noticeable damage).

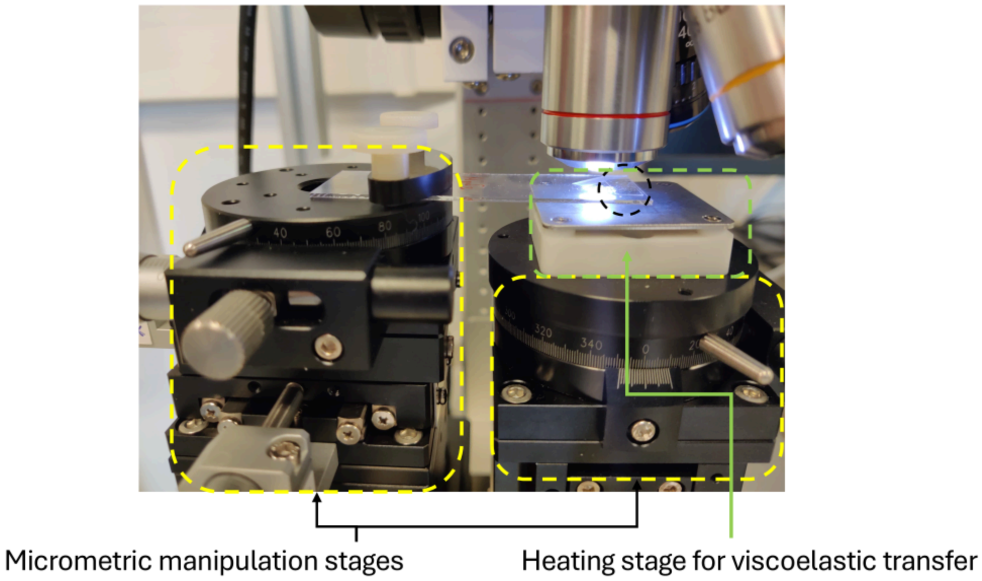

Figure 39. Custom micropositioning transfer station used for flake transfer on substrate. The green selection shows the Peltier heating stage which hosts the substrate. Vacuum is used to hold the substrate position during the transfer. On the left side, the turret used to manipulate the glass carrier with PDMS polymer. Each turret allows several degrees of freedom.

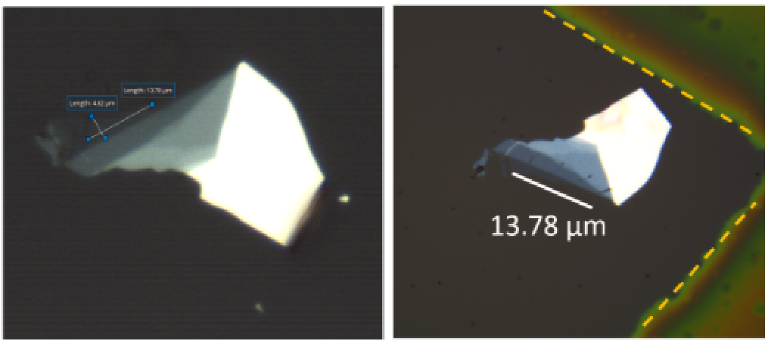

Figure 40. Optical microscopy image of the flake before transfer. The flake is characterized by regions with different thicknesses. Image on the left: the flake is precisely transferred using the micromanipulators close to a previously marked spot on the glass coverslip; the reference will be used to easily find the sample on stroboSCAT objective.

At the end of the transfer process, the sample is still not perfect. PDMS and blue tape glue residuals might still be on the surface of the flakes, so acetone bath, isopropanol rinsing and N_2 drying is required to deep clean the samples. The flake surface and its adhesion to the substrate might not be perfect due to the presence of air gaps and bubbles. The sample shows folds and residual mechanical strain after exfoliation and transfer (Fig. 41, right). These factors worsen the optical quality of the sample and alter its optoelectronic properties, thus the sample is annealed in nitrogen atmosphere at 110 °C for 60 min in a glovebox (Fig 41, left).

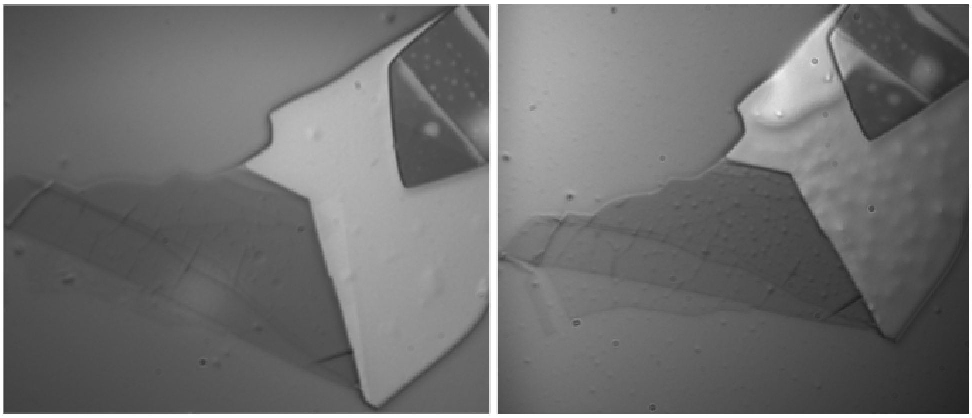

Figure 41. Image on the right: optical microscopy image of the selected flake before annealing shows numerous bumps, bubbles and folds across the whole surface. Image on the left: optical microscopy image of the same flake after annealing shows optically smoother surface.

4.1.2 Thickness-Dependent Optical and Excitonic Properties

TMDs approaching the few-layers thickness regime experience strong changes in the electronic band structure due to interlayer coupling and quantum confinement. In 2D materials, the electron and hole wavefunctions are highly confined and their electrostatic interactions are weakly screened by the empty space around the material, resulting in stable excitons even at room temperature—in bulk structures the surrounding material screens these interactions by itself [6].

The TMDCs electronic band structure changes depending on the number of layers, showing a transition from indirect to direct band gap as the monolayer thickness is approached (Fig. 42). DFT calculations and photoluminescence measurements have already been used to prove that strain can also cause the direct and indirect gaps to shift in $MoSe_2$ and WSe_2 monolayers [73].

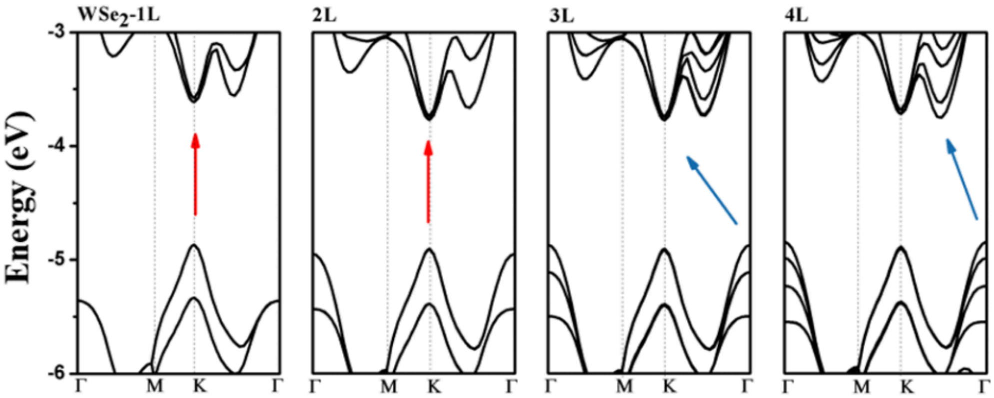

Figure 42. Band structure evolution of WSe2 in the Brillouin zone as function of the layer thickness [73]

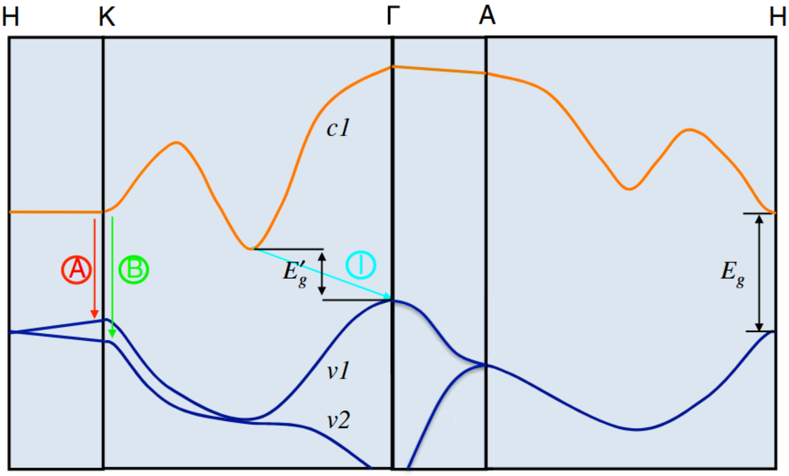

Figure 43. MoS_2 monolayer band diagram showing the lowest conduction band c1 and the highest split valence bands v1 and v2. A and B marks show the direct gaps and I is the indirect gap transition. [11]

Semiconducting TMDCs all show a similar set of spectral features between 1 and 6 layers (1L–6L); they all originate from exciton generation at different allowed electronic transitions.

The A-exciton peak is the closest to the absorption band edge of the semiconductor (1.6 eV for WSe_2 monolayer at room temperature, Fig. 43), it corresponds to the direct transition at the K point of the Brillouin zone from the highest valence band v1 to the lowest energy conduction band c2 (Fig. 43 shows it for MoS_2); this transition produces the most intense photoemission also because of the high monolayer confinement.

The B-exciton peak for 1L samples corresponds to higher energy direct transitions from a degenerate valence band v2 at the K point towards the lowest conduction band (Fig. 43) (2 eV for WSe_2 monolayer at room temperature, Fig. 44). The B peak's position evolves with thickness due to interlayer interactions and spin-orbit coupling. The C-exciton peak is also an interesting spectral feature for applications in the optical detector field. It is a broader excitonic resonance situated at higher energies 2.4 eV in WSe_2 monolayer [74], but its position relative to the other excitonic resonances can vary going from 1L to 6L samples, which enables it to serve as a spectral fingerprint for layer-number identification. It is a broad resonance due to transitions happening in what is called the "$\Gamma - Q$" or Λ region, where "band nesting" happens [75].

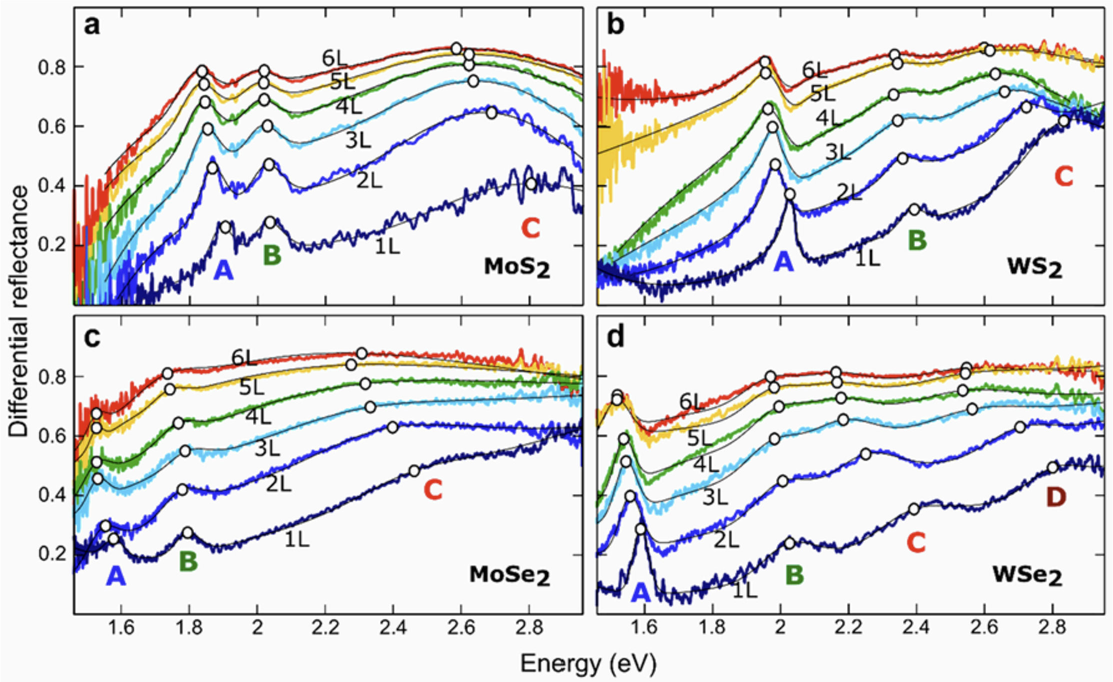

Figure 44. Differential reflectance spectra with thicknesses varying between 1L and 6L for some TMDCs [74]

Section 4.3 of this chapter will show how the excitonic landscape is important when selecting probe wavelengths in stroboSCAT experiments, as it directly affects the sensitivity to different carrier species and transport dynamics.

4.2 Thermal transport in TMDs

4.2.1. Thermal conductivity and thermal dissipation in TMDs on Substrates

This section of the thesis aims to demonstrate how stroboscopic scattering microscopy can be used as a powerful tool to directly investigate the thermal properties of TMDs with high temporal and spatial resolution. Pump–probe techniques such as the one discussed here allow us to predominantly photoinduce heat under specific excitation conditions. We show that such conditions can be found in high fluence or photoexcitation at above-band gap wavelengths. Both can produce localized heating via several mechanisms, including excitation above the band gap followed by lattice thermalization as well as nonradiative pathways such as Auger-mediated heating [76]. We observe that heat-dominated profile expansion curves with their slow diffusion match the diffusion simulations of pure heat transport. We perform measurements in several regions of a WSe_2 flake—each corresponding to different thicknesses (see terraces in Fig. 40); the amplitude of the signal decays shows a thickness dependence when exciting at high fluence at a wavelength above the band gap. That behavior as well is consistent with thickness-dependent heat dissipation to the substrate.

4.2.2. Evidence of heat-dominated stroboSCAT signal under high fluence conditions or above-band gap excitation

We first excite the WSe_2 flake with 640 nm pump pulses, above the band gap of the material (around 750 nm). The pump power for each experiment has been measured with a silicon-based sensor and power meter mounted on the microscope objective. Knowing the repetition rate of the pulse emission we computed the energy incident on the sample, and we measured the size of the pump spot and used its area to compute the fluence. To deterministically vary the pump fluence and get power dependent experiments, we kept the power of the laser diode steady, while stacking neutral density filters in the pump optical path. All the results (Fig. 47 a, b) are obtained with probe pulses at 780 nm.

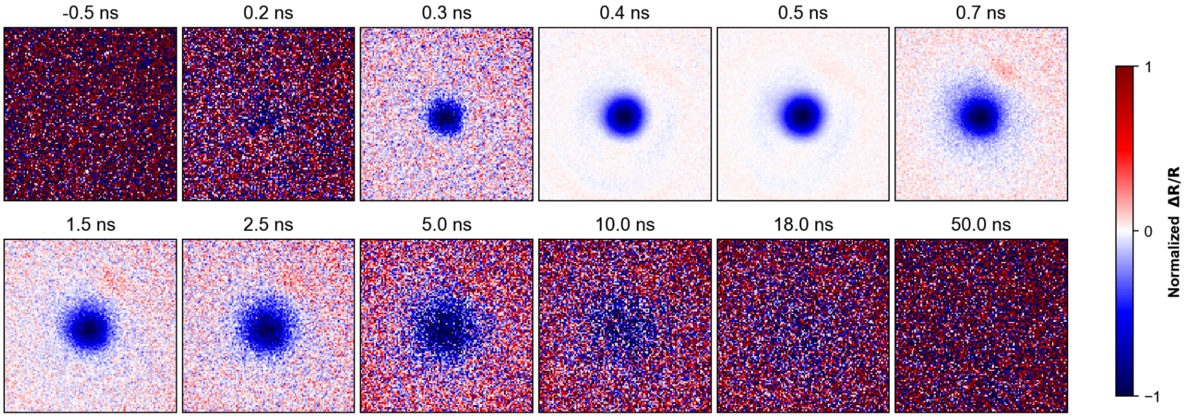

Figure 45. Transient reflectance images at several time delays, 640 nm pump, 780 nm probe and a fluence of 0.27 mJ cm^{-2}

Exciting the sample with different fluences and fitting the pump-probe images with Gaussians, we get the diffusion coefficient of the energy carriers by tracking the standard deviation of the gaussian (Fig. 45 shows the expanding gaussian excitation spot). In the Fig. 47 a,b each trace shows the variation in time of the Gaussian fit variance (the mean-squared displacement), measured for fluences in the $8.5\ \mu J\ cm^{-2}$ - $270\ \mu J\ cm^{-2}$ range. The MSD curves show a fluence dependence in the first 1-2 ns that become less strong after. To get a clearer idea of the origin of the measured signals, COMSOL finite element simulations have been used to reproduce the effects of purely thermal relaxation in WSe_2 films supported by glass substrate. The simulations were tuned by using thickness values in the ranges observed from AFM data of WSe_2 flakes under analysis (Fig. 46). The thermal conductivities—both in-plane and cross-plane—and the interfacial thermal conductivities were already known in literature [77–79]. For the high fluence MSD traces that are presumably predominantly reporting on heat transport, we observe a good match with heat diffusion simulations, which by itself suggests the thermal nature of the observed energy carriers transport in the 1-100 ns time window. The early time nonmonotonic nature of the mean-squared displacements is a subtle sign that several processes are affecting the excitated state profile propagation in the first few nanoseconds. We suspect that simultaneous contributions from charge carriers and temperature changes must be more carefully discerned. The exciton lifetime is generally considered to be several hundreds of nanoseconds. A transition of the signal from having dual electronic and thermal signals to being dominated by thermal may therefore be expected on ~1 ns time scale. Hence the strong agreement between the transport data and simulations of thermal transport for times beyond ~1 ns. These phenomena need further study to be correctly addressed.

The above observations are general across the various thicknesses we came across in the sample 1–6L as identified by AFM (Fig. 46).

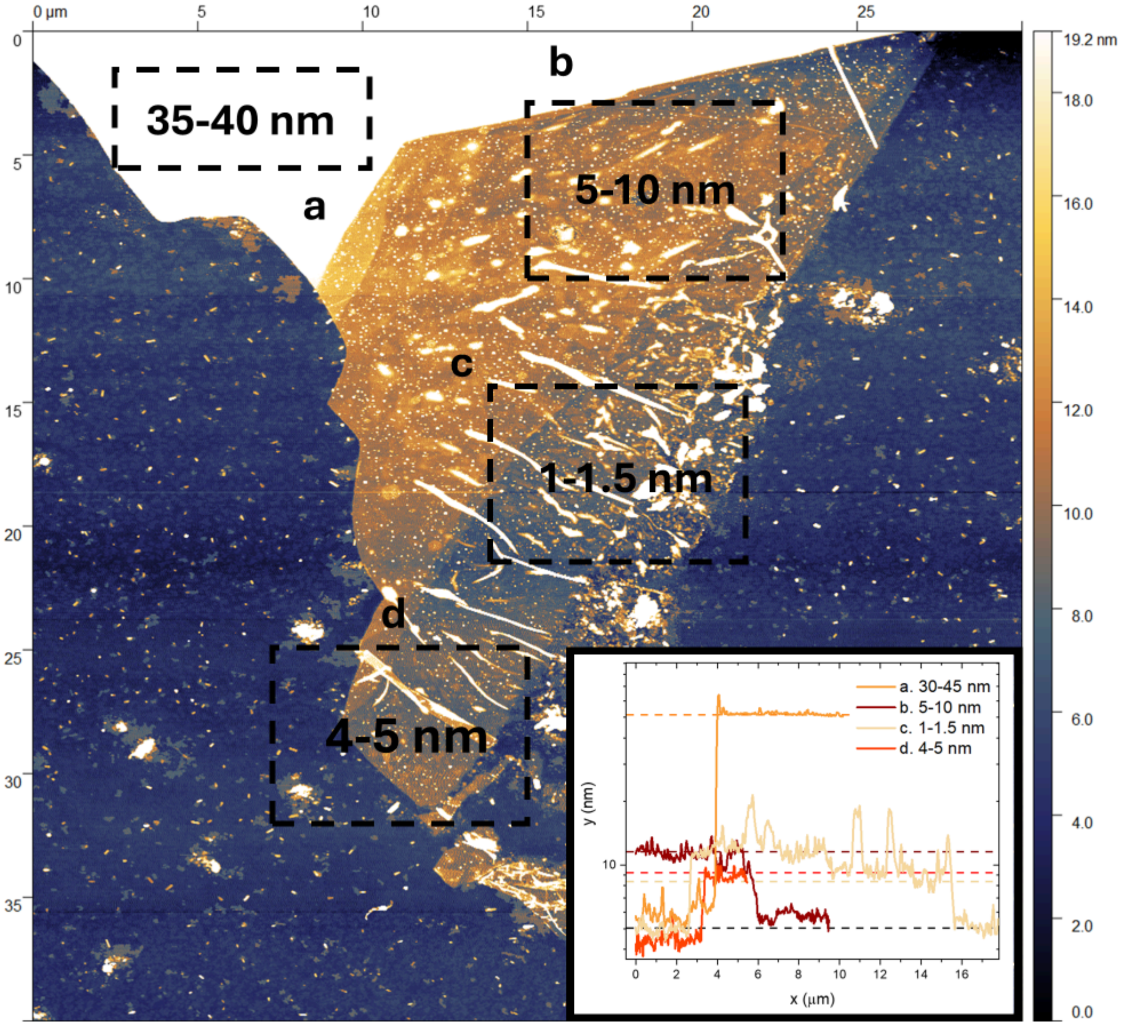

Figure 46. Atomic force microscopy image (AFM) of a WSe2 flake with regions of interest of various thicknesses (a,b,c,d). (a) 40-45 nm region. (b) 6-7 nm region. (c) 1-1.5 nm region. (d) 4-5 nm region. The inset shows the measured thickness profiles in each region of the flake.

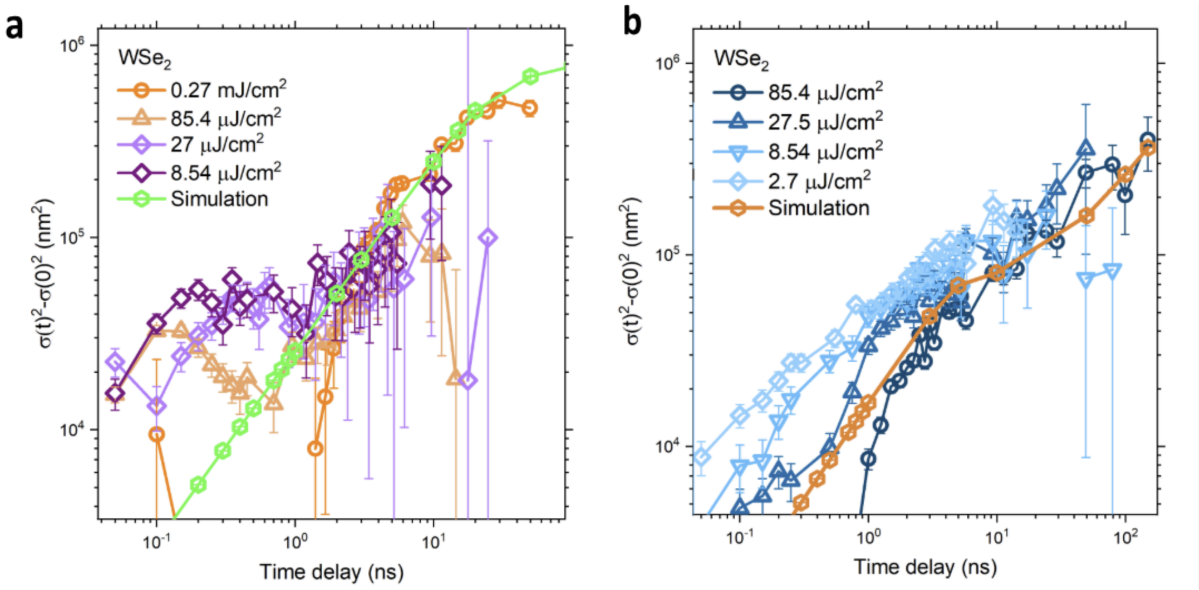

Figure 47. Mean squared displacement tracks in log-log scale for several pump fluence values with overlapped purely heat diffusion simulation (a) 35-40 nm thick region, k//=35 W m^{-1}K^{-1}, k = 0.05 W m^{-1}K^{-1}, $k_{interf(WSe2/glass)}$ = 4 MW m^{-2}K^{-1}. (b) 6-10 nm thick region, k//=20 W m^{-1}K^{-1}, k = 0.05 W m^{-1}K^{-1}, $k_{interf(WSe2/glass)}$ = 4 MW m^{-2}K^{-1} . 76–78

Lattice heating occurs when the material is excited with a pump wavelength above the band gap as previously shown at 640 nm, but we also get similar signatures when the pump wavelength is near the band gap but at high fluences. When we excite the sample at 780 nm, the mean squared displacement as a function of the fluence shows that we are still able to match the experimental traces with heat relaxation simulations when the fluence is in the order of $0.3\ mJ\ cm^{-2}$ over the 2-100 ns time range (Fig. 48 b). When we compare the near-band gap curves with those obtained at 640 nm (above gap with consequently higher lattice heating), we don't see any noticeable late time fluence dependence—especially for larger thickness (around 30-45 nm, Fig. 48 b). Also at lower thicknesses (Fig. 48 a) this pump wavelength allows us to distinguish a clearly faster transport across the entire 1 ns window with diffusivity: $D = 1.48\ cm^2\ s^{-1}$ for low fluence that will be discussed in section 4.3.1, and a slower transport with diffusivity $D = 0.023\ cm^2\ s^{-1}$ which is probably due to thermal transport [78]. This pump wavelength—reducing further heating due to the relaxation of hot carriers—allows a more selective carrier excitation now only based on the fluence used to excite the flake. These last remarkable results suggest that at 780 nm pump and fluences up to hundreds of $\mu J\ cm^{-2}$, we are able to resolve energy carriers of thermal and electronic nature in WSe$_2$, with even clearer distinction at lower thickness regimes.

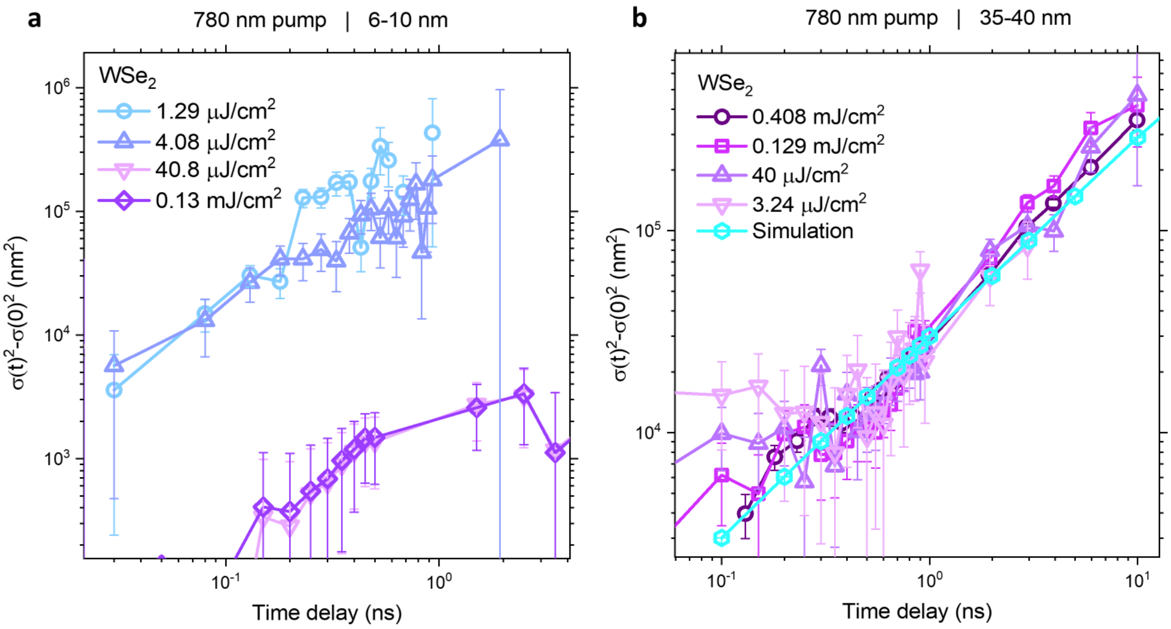

Figure 48. Mean squared displacement curves at 780 nm pump and 640 nm probe with ND filters in a 6-10 nm thickness range (a) and 35-40 nm thickness range (b)

4.2.3 Thickness-dependent studies and AFM correlation

The amplitude evolution in time of the pump-probe signal allows us to investigate the properties and the mechanisms underlying the energy carrier relaxation. Here, we perform stroboSCAT measurements under varying excitation conditions and across three different distinct film thicknesses (1.5, 6-10 and 30-35 nm) to evaluate how above and near-band gap conditions, combined with different fluences, influence the lifetime and decay behavior of the excited carriers.

By fitting the spatially-integrated amplitude of the stroboSCAT signal to a power law after around 1 ns, we observe that for above-band gap and high fluence excitation (Fig. 49 a), the decay becomes progressively slower as the WSe$_2$ thickness increases. The thickest region (~30-35 nm) in log-log scale shows a slope close to –0.5, which is consistent with the analytical solution for one-dimensional heat diffusion into a semi-infinite substrate, where the surface temperature decays proportionally to $t^{-1/2}$. This can be indicating a thermally dominated relaxation regime—especially after 1 ns, which is also coherent to what we have observed with finite-element heat diffusion simulations presented in Section 4.2.4.

This behavior is consistent with strong lattice heating and Auger-mediated heating, both of which are enhanced under above-band gap excitation at high fluence. In such cases the longer relaxation times in thicker regions can be explained by slower vertical heat dissipation through the WSe_2-substrate interface. This effect resembles the thickness dependence observed in nanocrystal films (Chapter 3).

In contrast, at lower fluences under above-band gap excitation (Fig. 49 b), the decay becomes significantly faster with a weaker or negligible thickness dependence. This may suggest a reduction of the thermal component, and increasing weighting of electronic recombination mechanisms. A similar fast and thickness-independent decay is also observed under near-band gap, low fluence excitation (Fig. 47 c) across the entire time window, suggesting the reduction of heat contribution even at later times.

Thin films consistently show faster relaxations across the varying pump conditions, with slopes s close or even higher than –1 ($s = -1.27$ in Fig. 49 a and $s = -0.97$ in Fig. 49 b). Strong quantum confinement and high exciton density at higher fluence provide enhanced nonradiative electronic recombination pathways—such as Auger and exciton-exciton annihilation (EEA) processes. Both nonradiative mechanisms are usually approximated to bimolecular processes and the solution of their rate equations lead to slopes similar to our findings.

The results obtained at near-band gap excitation and low fluence (Fig. 49 c) show unexpected trends and require further investigation. In that case, the decay slope remains close to –0.5 for thicknesses of 1-1.5 nm, again resembling heat-related effects. The thicker regions exhibit slower decays ($s = -0.27$) that may be explained as a pre-asymptotic regime

While in the NC study thickness dependence of the decay can be an effective strategy to distinguish heat from electronic transport, in TMDs this distinction is much less clear. Thickness-dependent decay kinetics can provide insights into the dominant relaxation mechanisms, but they should be interpreted with care—particularly in the low-fluence, near-band gap regime, where thermal and electronic contributions coexist and cannot be fully disentangled from amplitude decay alone.

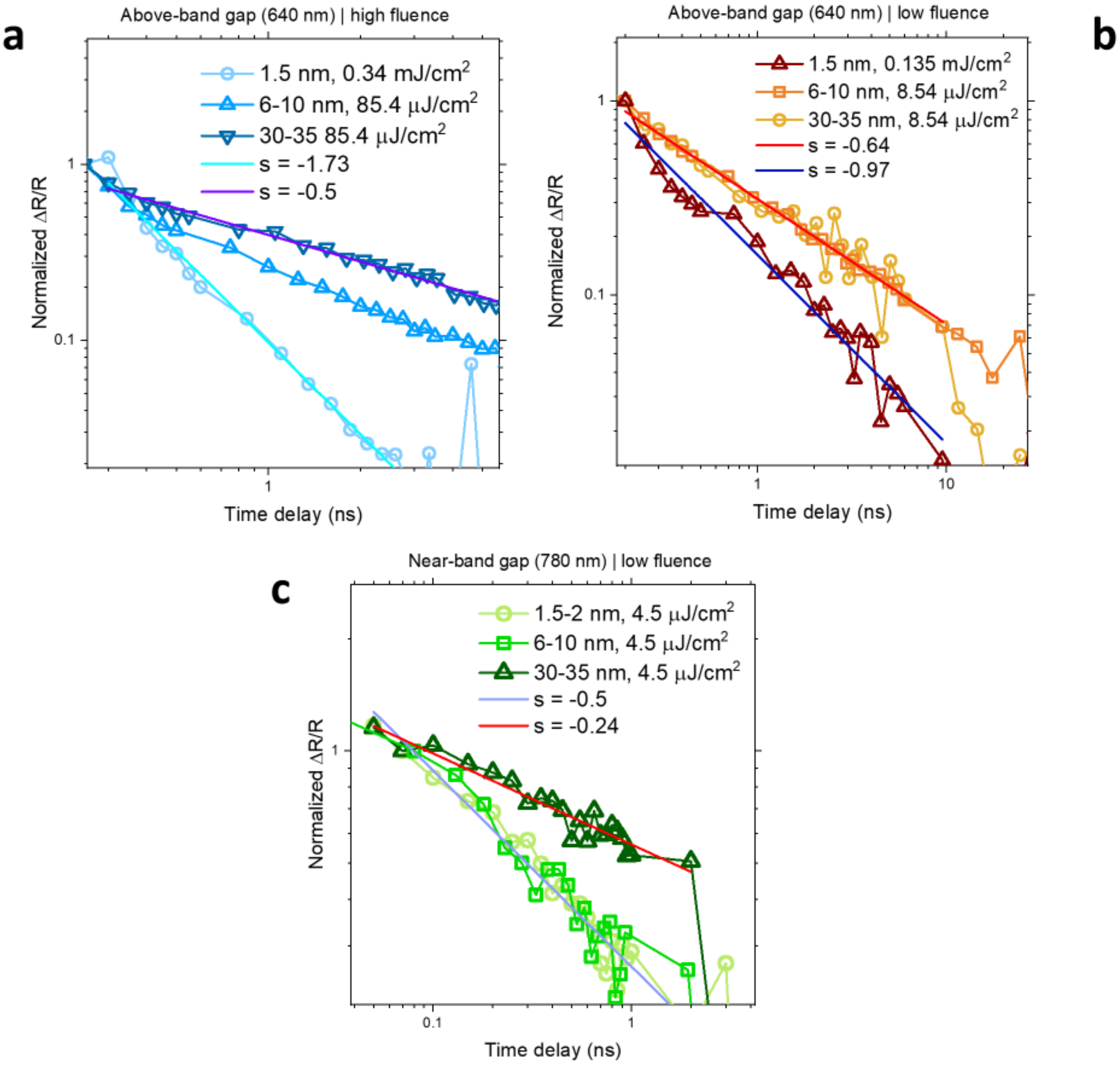

Figure 49. Pump-probe signal relaxation in time as a function of the thickness. (a) Above-band gap (640 nm pump) and high fluence. (b) Above-band gap and low fluence. (c) Near-band gap and low fluence.

4.2.4 Study of Thermal Transport in TMD Heterostructures Through Finite Element Simulation

The understanding of thermal transport at nanoscale in more complex TMD-based structures is central in the development of more efficient optoelectronic devices. All the experiments described above were done on simple WSe_2/SiO_2 tandems, but researchers are currently coupling other 2D materials like hexagonal boron nitride (hBN) with TMDs such as WSe_2 to form heterostructures [79].One interest in these stacks lies in their highly increased efficiency in heat dissipation. These structures require complex thermal characterization as the interfaces in between each layer can strongly affect the way heat propagates through the structure. To this day, optothermal Raman techniques are used to study thermal transport transport properties in 2D material heterostructures and at the interfaces of different materials [80]. Here we use finite element simulations of heat transport to show that in principle we can spatiotemporally resolve thermal transport in TMDs-structures: WSe_2 on glass (Fig. 51 a), WSe_2 on hBN (Fig. 51 b) and WSe_2 on a silicon substrate. These simulations output the lateral mean-squared expansion in time of an initial temperature profile as it is affected by the in-depth propagation through the materials of the device and their respective interfaces. In the case of WSe_2-glass tandem, the simulation results are compared with experimental stroboSCAT data obtained with above-band gap and high fluence excitation—the pump conditions that we know can generate Auger-mediated heating and lattice heating.

Even though further stroboSCAT experiments of WSe_2 on different substrates are required to make this study less speculative, in the previous chapter we have shown that COMSOL anisotropic heat diffusion simulations can reproduce in good approximation thermal transport behavior in WSe_2-on-glass systems in specific conditions. Assuming the same heat-dominated conditions, we simulate the spatiotemporal evolution of heat lateral diffusion in a 7 nm thick WSe_2, showing that we can in principle resolve how thermal transport is affected by the thermal properties of each substrate and interfacial coupling between the materials. In the simulations we analyse an heterostructure: WSe_2 on hexagonal boron nitride (hBN) and WSe_2 on silicon in addition to glass. The experimentally measured MSD curve is obtained by exciting the sample at 640 nm (with a fluence of $85.4\ \mu J\ cm^{-2}$) in a region 6-7 nm thick (see AFM measurements in Fig. 46). To simulate the WSe_2/glass system we used the same thickness as a simulation parameter; to model the WSe_2 layer we used a density of $7860\ kg\ m^{-3}$ and a heat capacity of $300\ J\ kg^{-1}K^{-1}$. We used an in-plane thermal diffusivity $k_{\parallel, WSe_2} = 20\ W\ m^{-1}K^{-1}$ [78], out-of-plane thermal diffusivity for a thin disordered WSe_2 $k_{\perp, WSe_2} = 0.05\ W\ m^{-1}K^{-1}$ [81] (might be higher for these samples), interfacial thermal conductivity of

WSe_2 on glass $k_{WSe_2/glass} = 3.45\, W\, m^{-2} K^{-1}$ [78]. We chose a glass substrate thickness of 10 μm so that it was much thicker compared to the TMDC film, the density of $2203\, kg\, m^{-3}$ and heat capacity $703\, J\, kg^{-1} K^{-1}$. The assumed isotropic glass thermal conductivity $k_{glass} = 1.38\, W\, m^{-1} K^{-1}$. To simulate the silicon substrate we used a density of $2329\, kg\, m^{-3}$and an isotropic heat capacity $700\, J\, kg^{-1}\, K^{-1}$; the thermal conductivity used is $131\, W\, m^{-1} K^{-1}$.

We notice that after 1-2 ns the simulated mean squared expansion curve relative to WSe_2 on the glass substrate closely matches the experimental one—which we found to be consistent with being heat dominated. Up to 5 ns, heat diffuses through the TMD layer—both the in-plane and cross-plane thermal conductivities of the material contribute to the anisotropic heat dissipation. After 5 ns the heat has propagated through the film and transfers into the glass substrate, which acts as an additional dissipation path for the excess heat (Fig. 51 a). This results in an apparent decrease in the instantaneous diffusion coefficient in the MSD curve. Both the traces relative to WSe_2/hBN and WSe_2/silicon stacks show an opposite increase in the lateral expansion of heat (Fig. 50). In the case of silicon substrate we observe an apparent acceleration in the MSD due to silicon having a higher thermal conductivity than that of glass. If the film is thin enough, the higher thermal diffusivity of silicon helps in pulling laterally the heat away from the initial excitation spot. The hBN substrate brings this effect to its extreme because of its high thermal diffusivity, and the anisotropic nature of the thin layer brings additional dynamics[77]. Once heat has reached the hBN layer, it propagates parallel to the WSe_2/hBN interface due to the high in-plane thermal conductivity of hBN. This highly efficient pathway for dissipation pulls even more the heat laterally in the TMD layer, causing the apparent acceleration in the lateral diffusion (Fig. 51 b). At late time, heat transfers into the glass substrate causing again the MSD decrease.

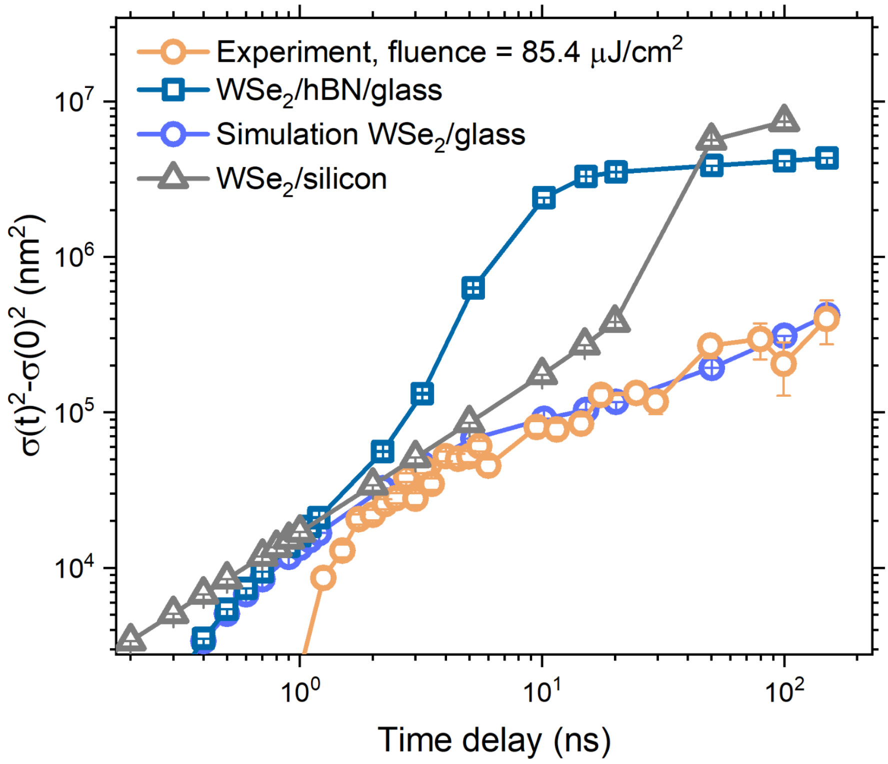

Figure 50. Experimental MSD measured in a 7 nm thick region at 85.4 J cm-2 compared with purely heat diffusion simulations in WSe_2/glass, WSe_2/hBN/glass and WSe_2/silicon stacks.

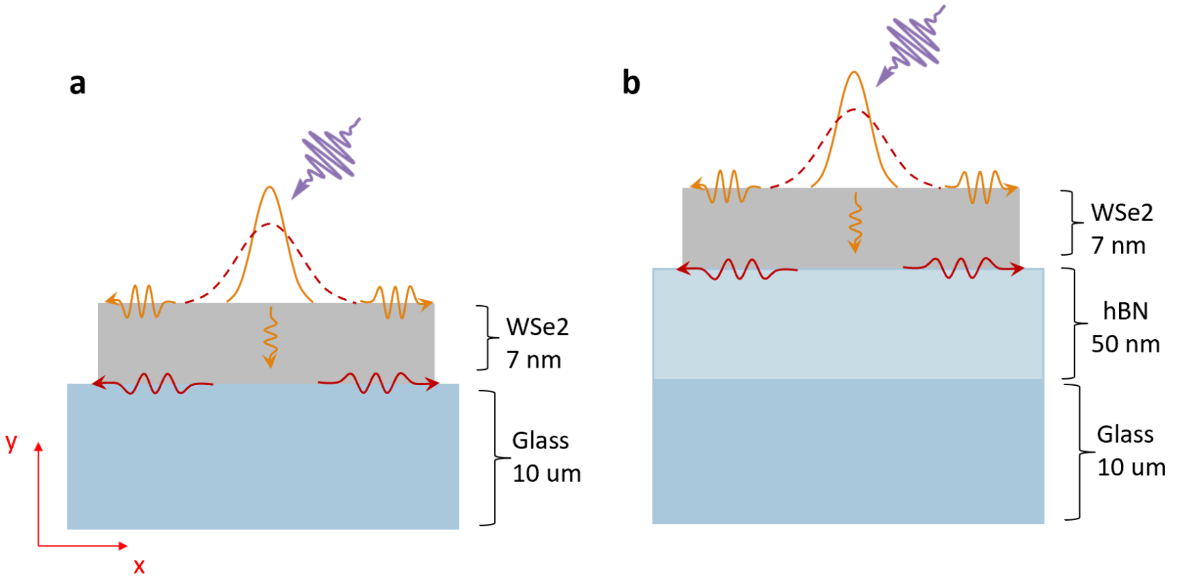

Figure 51. Cartoons showing purely thermal excitation of a TMD thin layer with consequent thermal transport in (a) WSe_2/glass stack and (b) WSe_2/hBN heterostructure on glass

Although these simulations have not been compared to stroboSCAT experiments on heterostructures yet, it would be interesting to further investigate heat propagation in suspended WSe_2 and fully-encapsulated TMDs in hBN layers.

Systematic variation of the substrate material, including anisotropic conductors such as hBN, can enable direct control over interfacial heat dissipation, introducing new strategies for thermal management in 2D optoelectronic devices. In principle, transient reflectance microscopy can be used to noninvasively probe heat transport across complex structures and substrates, providing time-resolved and in-situ diffusivity measurements.

4.3 Charge Transport in TMDs

4.3.1 Low Fluence and Wavelength-Dependent Study of Electronic Transport with StroboSCAT

In Section 4.2, we have found evidence that by combining near and above-gap wavelengths, fluence and thickness-dependent stroboSCAT measurements—correlated with heat diffusion simulations and AFM thickness data—we can control whether our pump-probe measurements are heat dominated.

In contrast, we observed that when the excitation wavelength is tuned close to the band gap (780 nm), lattice heating is significantly reduced and the power-dependent MSD curves align more closely with heat-diffusion simulations only at late times. At shorter timescales, we observe faster transport and a pronounced fluence dependence, which we attribute to regimes increasingly dominated by electronic transport as the fluence decreases. Under 780 nm excitation in thicker regions, thermal and electronic transport can be distinguished by timescale—electronic transport dominating before 1 ns and thermal transport prevailing at longer delays (Fig. 48 b). For the same pump wavelength but in thinner regions (Fig. 48 a), the transport dynamics are even more distinct across the entire 1 ns time window.

This brought us to further investigate these last conditions, with the aim of measuring electronic transport diffusivity in a flake of WSe_2 via transient reflection microscopy and with the background knowledge we now have.

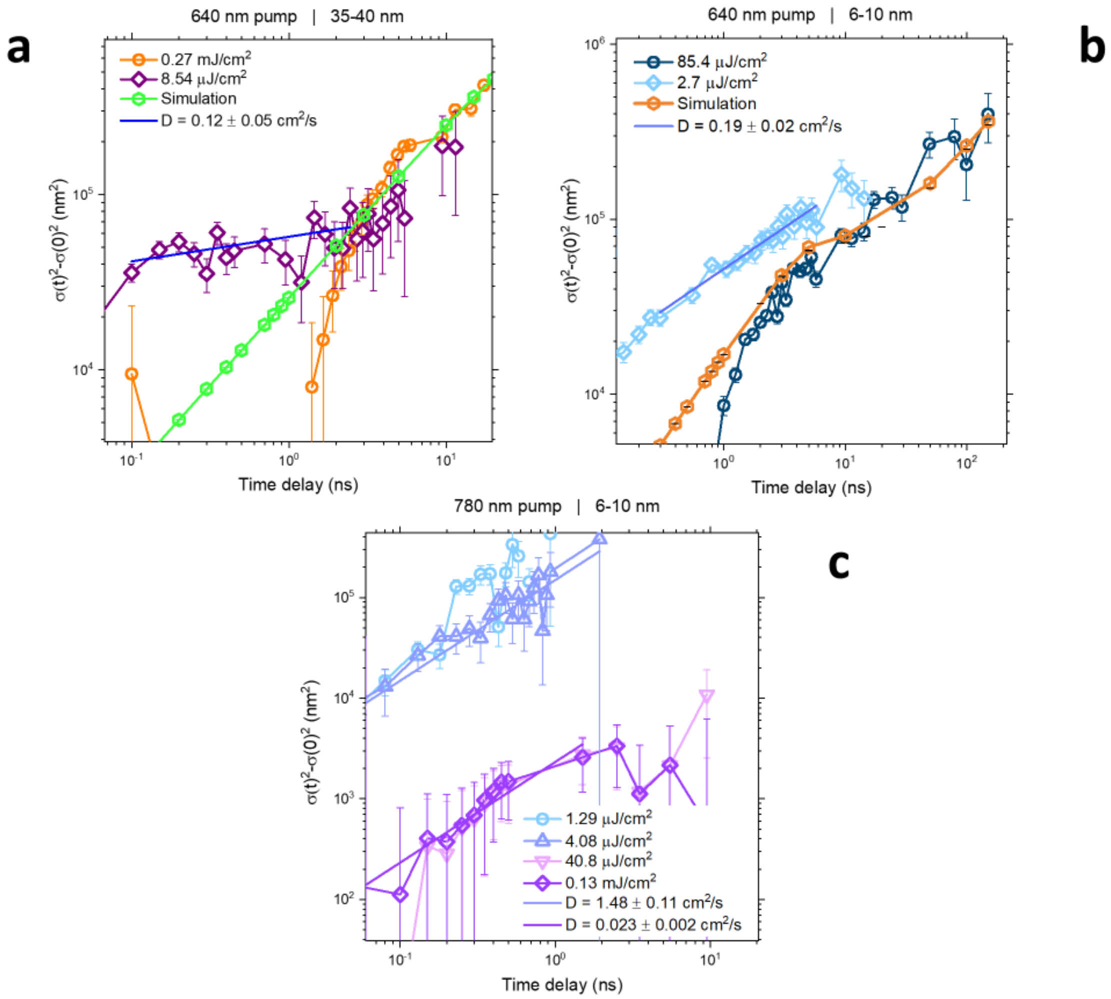

Figure 52. The MSD in linear-log scale are fitted with linear functions, whose extracted slope measures the microscopic diffusivity in the fitted time interval. (a,b) linear fit of low fluence, above-gap MSD traces, (c) linear fit of low and high fluences in near-gap conditions

Using a linear fit on the mean squared expansion curves obtained above-band gap at lowest fluences (few $\mu J\ cm^{-2}$) we measure $D = 0.12\ cm^2/s$ in the 35-40 nm thickness range (Fig. 52 a) and similar value, $D = 0.19\ cm^2/s$, in the 6-10 nm thickness range (Fig. 52 b). These values are in the range of thermal conductivities reported in literature—converted in terms of diffusivity they range between $0.21\ cm^2/s$ and $0.085\ cm^2/s$. Electronic transport in nonencapsulated WSe_2 can have a diffusivity of several $cm^2\ s^{-1}$, Cui at al. reported a value of $9 \pm 3\ cm^2/s$ for excitons in bulk WSe_2 [82]. At these probe wavelengths, our measured values therefore do not match purely electronic or purely thermal transport, suggesting that the observed dynamics likely arise from a combination of both. This means further efforts will be required to disentangle the two.

When we repeat the measurements on 6-10 nm flake and we extract the diffusivity before 1 ns at low fluence and with a 780 nm pump (Fig. 52 c), we obtain $D = 1.48\ cm^2/s$. Compared to the purely thermal traces with $D = 0.023\,cm^2/s$ and the diffusivities obtained at 640 nm excitation, this indicates a clear reduction in the heat contribution to the carrier expansion, with excitons and free charges being predominant.

Although further investigation is needed to fully identify the processes governing the MSD kinetics and dynamics at ultrafast timescales under high-energy pump conditions, our results indicate that near-gap excitation and fluences in the $\mu J\ cm^{-2}$ range provides a suitable starting point for observing electronic transport in TMDs.

Up to this point the probe wavelength for carrier detection was selected to ensure a qualitatively strong pump–probe SNR for high-quality measurements. Energy carriers in TMDs originate from multiple excitonic transitions (see section 4.1.2) with free carriers such as electrons and holes contributing over sub-nanosecond to few nanosecond timescales. Disentangling their roles in transport remains challenging, but excitons are expected to play a major role—especially in the few-nanometer thick samples—due to quantum confinement. While techniques such as time-resolved photoluminescence could help isolating each contribution, here we use transient reflection spectroscopy to map sample's electronic landscape and select probe wavelengths that maximize stroboSCAT sensitivity to electronic carriers. StroboSCAT detects transient changes in the complex refractive index, the choice of pump and probe wavelengths relative to A, B and C excitonic resonances determines the sensitivity to different carrier species and to thermal effects.

The transient spectra reported in Fig. 53 were measured in a thin flake region (1-1.5 nm) using a 640 nm pump at moderate fluence ($\sim 29\ \mu J\ cm^{-2}$) over a 10 ns time window. The data reveal the C resonance of WSe_2, centered at 540 nm for this thickness, and were collected at moderately high diode power—so a thermal contribution is expected. Around 590 nm, we observe a spectral feature of opposite sign and fast decay that still needs to be addressed.

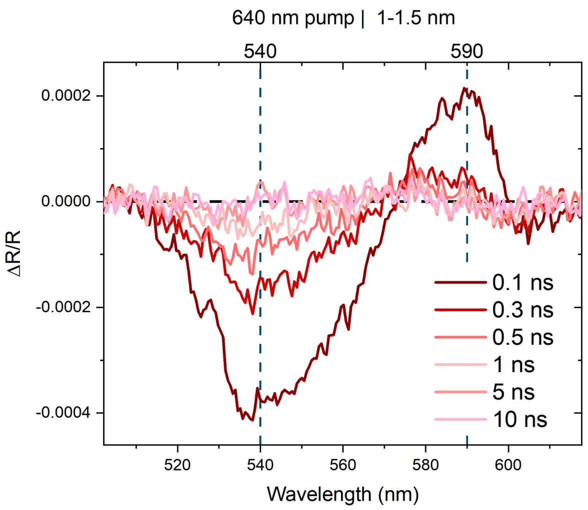

Figure 53. Transient reflectance spectra measured with 640 nm pump at 1.22 mJ cm-2 showing the C peak at 540 nm and a secondary feature at 590 nm between 0.1 and 10 ns time delays.

Probe wavelength-dependent pump–probe measurements (Fig. 54) show that we can measure diffusivities of of $2.94\ cm^2/s$ at 520 nm and $1.24\ cm^2/s$ at 640 nm probe, with under near-gap, low fluence excitation. These values fall within the range of reported electronic diffusivities for WSe_2, particularly those associated with free charge carriers [83]. Close to resonance probe wavelengths (520 nm or 640 nm) allow strong and reliable transient reflectance measurements, mostly due to excitons and free charges probing.

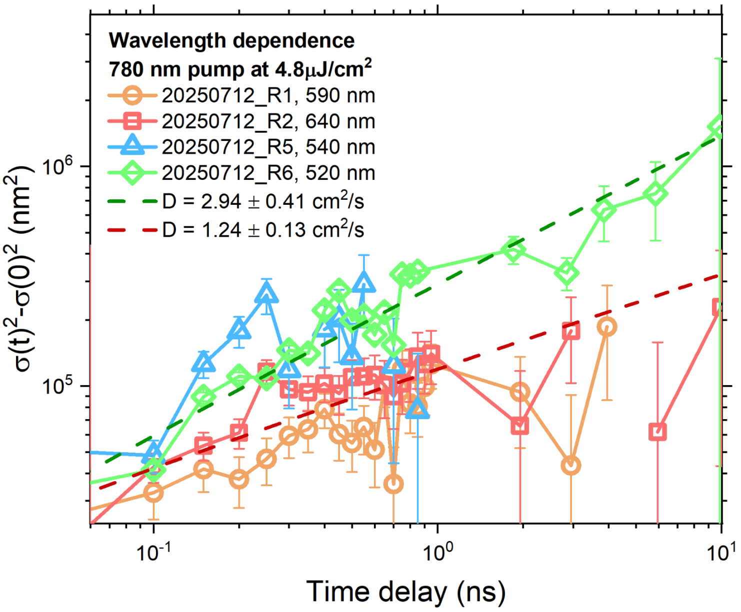

Figure 54. Mean squared displacement measured in a 1.5-3 nm thick region, with 780 nm pump at 4.8 mJ cm-2 and probe at 520 nm, 540 nm, 590 nm and 640 nm

In this chapter, we investigated the general properties of TMDs—with particular focus on WSe_2. We showed how bulk crystals can be mechanically exfoliated and reduced to atomically thin films with peculiar electronic properties strongly related to the thickness. Following the methodology used in the characterization of NCs films, we similarly combined spatiotemporal pump–probe microscopy with AFM profiling and finite-element simulations to prove that in certain excitation conditions the interplay between thermal and electronic transport can be disentangled also in these layered semiconductors.

The results show that the balance between heat dissipation and charge transport is strongly dependent on excitation wavelength and fluence, but the thickness of the film doesn't allow us a consistent heat-charge regime separation as observed in NCs. At high fluences or above-gap excitation, the stroboSCAT signal is dominated by lattice heating, while under near-gap, low-fluence excitation, electronic carriers can be selectively probed. Careful tuning of the experimental parameters is important to isolate the desired transport channel. Moreover, the consistency between experimental observations and COMSOL simulations has been used to investigate the idea that pump–probe techniques as stroboSCAT can hypothetically be used to non-invasively probe the thermal properties of TMD-based complex structures.

We further demonstrated that probe wavelength selection—with best results at 520 nm—provides an additional lever to further improve the electronic response of the material to near-gap, low fluence excitation.

Chapter 5

Conclusion and Perspectives

This thesis has explored the capabilities and the potential of stroboscopic scattering microscopy (stroboSCAT) as a high spatio-temporal resolution tool for mapping energy transport in low-dimensional semiconductors. We have shown that this characterization technique can be used to simultaneously track electronic and thermal transport on a wide range of timescales, even in structurally and energetically disordered systems.

In nanocrystal solids, we were able to identify conditions where transient reflectance signals are dominated by electronic carriers—such as excitons and free charges—and others where lattice heating and Auger-mediated processes prevail. We showed that thickness-dependent relaxation trends as well as mean-squared displacement and transient spectra analysis can be used to clearly distinguish thermal and electronic contributions. These observations were benchmarked against finite-element simulations, and local thermal diffusivity was quantified without invasive transducers.

In WSe_2 flakes, we extended the concepts learnt through the study on NCs to 2D materials, revealing the influence of excitation wavelength, fluence and thickness on the balance between electronic and thermal contributions to the pump-probe signal. Through correlation of stroboSCAT data with AFM mapping and COMSOL simulations, we provided experimental evidence for heat-dominated transport signals at high fluence/above-gap excitation, and identified the conditions that favor electronic transport signature isolation.

NCs and TMDs are just two material systems but the technique, the methodology and the analysis described in the chapters of this manuscript can be generalized to a broad class of novel otoelectronic materials, including persovskites, organic semiconductors and heterostructures. As demonstrated for both materials, the versatility of this label-free microscopy technique comes with the necessity of methods to disentangle overlapping energy transport processes at the nanoscale. The observation and characterization of electronic and thermal transport with high spatiotemporal resolution opens many paths for optimizing device design, improving charge collection and thermal management.

In conclusion, this work establishes that stroboSCAT, together with COMSOL simulations and the other correlated techniques, is a versatile platform for fundamental transport studies.

Abstract

The efficiency of silicon-based optoelectronic devices has greatly improved due to the growing knowledge of the material, yet the increasing miniaturization and performance demand is pushing research towards fundamental physical limits. At nanometer scales, carrier mobility is degraded, recombination rates affect operation speed, and thermal management becomes a challenge. Low-dimensional semiconductors such as colloidal nanocrystal (NC) films and transition metal dichalcogenides (TMDs) are therefore investigated as promising candidates for next-generation optoelectronics.

The objective of this thesis is to characterize the energy transport mechanisms in these nanomaterials and identify the factors that impact on their behavior. To simultaneously access electronic and thermal carriers with sub-micrometer spatial and nanosecond temporal resolution, we employ stroboscopic scattering microscopy (stroboSCAT). In this pump–probe technique, a focused laser pulse generates localized excited energy carriers, while a delayed wide-field probe pulse detects refractive index perturbations, enabling direct reconstruction of diffusion profiles, lifetimes, and diffusivities.

Experiments on CdSe and PbS NC films reveal that pump–probe signals contain overlapping electronic and thermal components that need to be correctly addressed. Near-gap, low-fluence excitation produces subdiffusive transport consistent with hopping-mediated dynamics, whereas above-gap or high-fluence excitation enhances Auger recombination and hot-carrier cooling, leading to significant transient heating. Thickness-dependent relaxation time, comparison with simulations and timescale analysis confirm the thermal origin of late-time signals, allowing thermal and electronic regimes to be correctly distinguished.

The methodology is extended to WSe_2 flakes mechanically exfoliated up to atomically thin films. High-fluence, above-gap excitation produces heat-dominated signals which have been correlated to heat relaxation finite element simulations (COMSOL). While near-gap, low-fluence excitation allows us to selectively measure electronic transport within the first nanoseconds. Probe-wavelength dependent studies near the excitonic resonances further enhance selectivity, yielding diffusivities of 1–3 cm^2/s, consistent with literature values. Correlation with AFM profiling and COMSOL simulations shows that stroboSCAT can also access interfacial heat dissipation in layered structures.

In conclusion, stroboSCAT emerges as a versatile platform to disentangle electronic and thermal transport in nanomaterials, providing mechanistic insight and quantitative parameters for the design of efficient and stable optoelectronic devices.

References

1. Woditsch P, Koch W. Solar grade silicon feedstock supply for PV industry. *Sol Energy Mater Sol Cells*. 2002;72(1-4):11-26. doi:10.1016/S0927-0248(01)00146-5

2. Kaiser W. Kinetic Monte Carlo Study of Charge and Exciton Transport in Organic Solar Cells.

3. Ashcroft NW, Mermin ND. *Solid State Physics*. Holt, Rinehart and Winston; 1976.

4. Le D, Barinov A, Preciado E, et al. Spin–orbit coupling in the band structure of monolayer WSe2. *J Phys Condens Matter*. 2015;27(18):182201. doi:10.1088/0953-8984/27/18/182201

5. Surana K, Singh PK, Rhee HW, Bhattacharya B. Synthesis, characterization and application of CdSe quantum dots. *J Ind Eng Chem*. 2014;20(6):4188-4193. doi:10.1016/j.jiec.2014.01.019

6. Ginsberg NS, Tisdale WA. Spatially Resolved Photogenerated Exciton and Charge Transport in Emerging Semiconductors. *Annu Rev Phys Chem*. 2020;71(1):1-30. doi:10.1146/annurev-physchem-052516-050703

7. Talapin DV, Lee JS, Kovalenko MV, Shevchenko EV. Prospects of Colloidal Nanocrystals for Electronic and Optoelectronic Applications. *Chem Rev*. 2010;110(1):389-458. doi:10.1021/cr900137k

8. Ahn S, Vazquez-Mena O. Measuring the carrier diffusion length in quantum dot films using graphene as photocarrier density probe. *J Chem Phys*. 2022;156(2):024702. doi:10.1063/5.0071119

9. Pinna J, Pili E, Mehrabi Koushki R, et al. PbI_2 Passivation of Three Dimensional PbS Quantum Dot Superlattices Toward Optoelectronic Metamaterials. *ACS Nano*. 2024;18(29):19124-19136. doi:10.1021/acsnano.4c04076

10. Akselrod GM, Prins F, Poulikakos LV, et al. Subdiffusive Exciton Transport in Quantum Dot Solids. *Nano Lett*. 2014;14(6):3556-3562. doi:10.1021/nl501190s

11. Mak KF, Lee C, Hone J, Shan J, Heinz TF. Atomically Thin ${\mathrm{MoS}}_{2}$: A New Direct-Gap Semiconductor. *Phys Rev Lett*. 2010;105(13):136805. doi:10.1103/PhysRevLett.105.136805

12. Geim AK, Novoselov KS. The rise of graphene. *Nat Mater*. 2007;6(3):183-191. doi:10.1038/nmat1849

13. Thakur N, Kumar P, Kumar S, et al. A review of two-dimensional inorganic materials: Types, properties, and their optoelectronic applications. *Prog Solid State Chem*. 2024;74:100443. doi:10.1016/j.progsolidstchem.2024.100443

14. Wang Y, Nie Z, Wang F. Modulation of photocarrier relaxation dynamics in two-dimensional semiconductors. *Light Sci Appl*. 2020;9(1):192. doi:10.1038/s41377-020-00430-4

15. Mak KF, Lee C, Hone J, Shan J, Heinz TF. Atomically Thin ${\mathrm{MoS}}_{2}$: A New Direct-Gap Semiconductor. *Phys Rev Lett*. 2010;105(13):136805. doi:10.1103/PhysRevLett.105.136805

16. Xing Y, Yazdani N, Lin WMM, Yarema M, Zahn R, Wood V. Effect of Positional Disorders on Charge Transport in Nanocrystal Quantum Dot Thin Films. *ACS Appl Electron Mater*.

2022;4(2):631-642. doi:10.1021/acsaelm.1c01011

17. Gilmore RH, Lee EMY, Weidman MC, Willard AP, Tisdale WA. Charge Carrier Hopping Dynamics in Homogeneously Broadened PbS Quantum Dot Solids. *Nano Lett*. 2017;17(2):893-901. doi:10.1021/acs.nanolett.6b04201

18. Introduction. In: *Absorption and Scattering of Light by Small Particles*. John Wiley & Sons, Ltd; 1998:1-11. doi:10.1002/9783527618156.ch1

19. Classical Theories of Optical Constants. In: *Absorption and Scattering of Light by Small Particles*. John Wiley & Sons, Ltd; 1998:226-267. doi:10.1002/9783527618156.ch9

20. Jackson JD. *Classical Electrodynamics*. 3rd ed. Wiley; 2021. Accessed June 28, 2025. https://www.perlego.com/book/3865737/classical-electrodynamics-pdf

21. Burstein E. Anomalous Optical Absorption Limit in InSb. *Phys Rev*. 1954;93(3):632-633. doi:10.1103/PhysRev.93.632

22. Weaver H. *On Light Scattering from Photoexcitations: Making Movies of Nanoscale Energy Transport in Emerging Semiconductors*. UC Berkeley; 2023. Accessed July 1, 2025. https://escholarship.org/uc/item/1bv7m5j0

23. Varshni YP. TEMPERATURE DEPENDENCE OF THE ENERGY GAP IN SEMICONDUCTORS.

24. Wei L, Anyi CL, Li H, Nie H, Wen B, Ling T. Fast 3D localization of nano-objects in wide-field interferometric scattering microscopy via vectorial diffraction model-derived analytical fitting. *Npj Nanophotonics*. 2025;2(1):21. doi:10.1038/s44310-025-00068-3

25. Ortega Arroyo J, Cole D, Kukura P. Interferometric scattering microscopy and its combination with single-molecule fluorescence imaging. *Nat Protoc*. 2016;11(4):617-633. doi:10.1038/nprot.2016.022

26. Ginsberg NS, Hsieh CL, Kukura P, Piliarik M, Sandoghdar V. Interferometric scattering microscopy. *Nat Rev Methods Primer*. 2025;5(1):23. doi:10.1038/s43586-025-00391-1

27. Lasers. In: *Fundamentals of Photonics*. John Wiley & Sons, Ltd; 1991:494-541. doi:10.1002/0471213748.ch14

28. Ashoka A, Gauriot N, Girija AV, et al. Direct observation of ultrafast singlet exciton fission in three dimensions. *Nat Commun*. 2022;13(1):5963. doi:10.1038/s41467-022-33647-5

29. Delor M, Weaver HL, Yu Q, Ginsberg NS. Imaging material functionality through three-dimensional nanoscale tracking of energy flow. *Nat Mater*. 2020;19(1):56-62. doi:10.1038/s41563-019-0498-x

30. Su H, Xu D, Cheng SW, et al. Dark-Exciton Driven Energy Funneling into Dielectric Inhomogeneities in Two-Dimensional Semiconductors. *Nano Lett*. 2022;22(7):2843-2850. doi:10.1021/acs.nanolett.1c04997

31. Feldman M, Vernier C, Nag R, et al. Anisotropic Thermal Transport in Tunable Self-Assembled Nanocrystal Supercrystals. *ACS Nano*. 2024;18(50):34341-34352. doi:10.1021/acsnano.4c12991

32. Kagan CR, Bassett LC, Murray CB, Thompson SM. Colloidal Quantum Dots as Platforms for

Quantum Information Science. *Chem Rev*. 2021;121(5):3186-3233. doi:10.1021/acs.chemrev.0c00831

33. Colloidal Quantum Dots as Platforms for Quantum Information Science | Chemical Reviews. Accessed July 4, 2025. https://pubs-acs-org.ezproxy.biblio.polito.it/doi/full/10.1021/acs.chemrev.0c00831

34. Park YS, Bae WK, Pietryga JM, Klimov VI. Auger Recombination of Biexcitons and Negative and Positive Trions in Individual Quantum Dots. *ACS Nano*. 2014;8(7):7288-7296. doi:10.1021/nn5023473

35. Guzelturk B, Cotts BL, Jasrasaria D, et al. Dynamic lattice distortions driven by surface trapping in semiconductor nanocrystals. *Nat Commun*. 2021;12(1):1860. doi:10.1038/s41467-021-22116-0

36. Klimov VI. Spectral and Dynamical Properties of Multiexcitons in Semiconductor Nanocrystals. *Annu Rev Phys Chem*. 2007;58(Volume 58, 2007):635-673. doi:10.1146/annurev.physchem.58.032806.104537

37. Knowles KE, Koch MD, Shelton JL. Three applications of ultrafast transient absorption spectroscopy of semiconductor thin films: spectroelectrochemistry, microscopy, and identification of thermal contributions. *J Mater Chem C*. 2018;6(44):11853-11867. doi:10.1039/c8tc02977f

38. Huang L, Cheng JX. Nonlinear Optical Microscopy of Single Nanostructures. *Annu Rev Mater Res*. 2013;43(1):213-236. doi:10.1146/annurev-matsci-071312-121652

39. Vazquez GDB, Morganti GLG, Block A, van Hulst NF, Liebel M, Tielrooij KJ. Spatiotemporal Microscopy: Shining Light on Transport Phenomena. *Adv Electron Mater*. 2024;10(2):2300584. doi:10.1002/aelm.202300584

40. Hayes D, Hadt RG, Emery JD, et al. Electronic and nuclear contributions to time-resolved optical and X-ray absorption spectra of hematite and insights into photoelectrochemical performance. *Energy Environ Sci*. 2016;9(12):3754-3769. doi:10.1039/c6ee02266a

41. Cooper JK, Reyes-Lillo SE, Hess LH, Jiang CM, Neaton JB, Sharp ID. Physical Origins of the Transient Absorption Spectra and Dynamics in Thin-Film Semiconductors: The Case of $BiVO_4$. *J Phys Chem C*. 2018;122(36):20642-20652. doi:10.1021/acs.jpcc.8b06645

42. Weaver HL, Went CM, Wong J, et al. Detecting, Distinguishing, and Spatiotemporally Tracking Photogenerated Charge and Heat at the Nanoscale. *ACS Nano*. 2023;17(19):19011-19021. doi:10.1021/acsnano.3c04607

43. Wang L, Nughays R, Rossi TC, et al. Disentangling Thermal from Electronic Contributions in the Spectral Response of Photoexcited Perovskite Materials. *J Am Chem Soc*. 2024;146(8):5393-5401. doi:10.1021/jacs.3c12832

44. Kambhampati P. Hot Exciton Relaxation Dynamics in Semiconductor Quantum Dots: Radiationless Transitions on the Nanoscale. *J Phys Chem C*. 2011;115(45):22089-22109. doi:10.1021/jp2058673

45. Guzelturk B, Utterback JK, Coropceanu I, et al. Nonequilibrium Thermodynamics of Colloidal Gold Nanocrystals Monitored by Ultrafast Electron Diffraction and Optical Scattering Microscopy. *ACS Nano*. 2020;14(4):4792-4804. doi:10.1021/acsnano.0c00673

46. Guzelturk B, Portner J, Ondry J, et al. Ultrafast Symmetry Control in Photoexcited Quantum

Dots. *Adv Mater*. 2025;37(4):2414196. doi:10.1002/adma.202414196

47. Dai Q, Song Y, Li D, et al. Temperature dependence of band gap in CdSe nanocrystals. *Chem Phys Lett*. 2007;439(1-3):65-68. doi:10.1016/j.cplett.2007.03.034

48. Utterback JK, Ruzicka JL, Hamby H, Eaves JD, Dukovic G. Temperature-Dependent Transient Absorption Spectroscopy Elucidates Trapped-Hole Dynamics in CdS and CdSe Nanorods. *J Phys Chem Lett*. 2019;10(11):2782-2787. doi:10.1021/acs.jpclett.9b00764

49. Liang Y, Diroll BT, Wong KL, et al. Differentiating Thermal Conductances at Semiconductor Nanocrystal/Ligand and Ligand/Solvent Interfaces in Colloidal Suspensions. *Nano Lett*. 2023;23(9):3687-3693. doi:10.1021/acs.nanolett.2c04627

50. Quantization of Multiparticle Auger Rates in Semiconductor Quantum Dots | Science. Accessed July 16, 2025. https://www.science.org/doi/10.1126/science.287.5455.1011

51. Ong WL, Rupich SM, Talapin DV, McGaughey AJH, Malen JA. Surface chemistry mediates thermal transport in three-dimensional nanocrystal arrays. *Nat Mater*. 2013;12(5):410-415. doi:10.1038/nmat3596

52. Peterson MD, Cass LC, Harris RD, Edme K, Sung K, Weiss EA. The Role of Ligands in Determining the Exciton Relaxation Dynamics in Semiconductor Quantum Dots. *Annu Rev Phys Chem*. 2014;65(1):317-339. doi:10.1146/annurev-physchem-040513-103649

53. Knowles KE, McArthur EA, Weiss EA. A Multi-Timescale Map of Radiative and Nonradiative Decay Pathways for Excitons in CdSe Quantum Dots. *ACS Nano*. 2011;5(3):2026-2035. doi:10.1021/nn2002689

54. Xu F, Gerlein LF, Ma X, Haughn CR, Doty MF, Cloutier SG. Impact of Different Surface Ligands on the Optical Properties of PbS Quantum Dot Solids. *Materials*. 2015;8(4):1858-1870. doi:10.3390/ma8041858

55. Burda C, Link S, Mohamed M, El-Sayed M. The Relaxation Pathways of CdSe Nanoparticles Monitored with Femtosecond Time-Resolution from the Visible to the IR: Assignment of the Transient Features by Carrier Quenching. *J Phys Chem B*. 2001;105(49):12286-12292. doi:10.1021/jp0124589

56. Zhu H, Yang Y, Wu K, Lian T. Charge Transfer Dynamics from Photoexcited Semiconductor Quantum Dots. *Annu Rev Phys Chem*. 2016;67(1):259-281. doi:10.1146/annurev-physchem-040215-112128

57. Ashoka A, Gauriot N, Girija AV, et al. Direct observation of ultrafast singlet exciton fission in three dimensions. *Nat Commun*. 2022;13(1):5963. doi:10.1038/s41467-022-33647-5

58. Lee EMY, Tisdale WA. Determination of Exciton Diffusion Length by Transient Photoluminescence Quenching and Its Application to Quantum Dot Films. *J Phys Chem C*. 2015;119(17):9005-9015. doi:10.1021/jp512634c

59. Zheng K, Sun F, Tian X, et al. Tuning the Interfacial Thermal Conductance between Polystyrene and Sapphire by Controlling the Interfacial Adhesion. *ACS Appl Mater Interfaces*. 2015;7(42):23644-23649. doi:10.1021/acsami.5b07188

60. Schnedermann C, Sung J, Pandya R, et al. Ultrafast Tracking of Exciton and Charge Carrier Transport in Optoelectronic Materials on the Nanometer Scale. *J Phys Chem Lett*. 2019;10(21):6727-6733. doi:10.1021/acs.jpclett.9b02437

61. Yoon SJ, Guo Z, Dos Santos Claro PC, Shevchenko EV, Huang L. Direct Imaging of Long-Range Exciton Transport in Quantum Dot Superlattices by Ultrafast Microscopy. *ACS Nano*. 2016;10(7):7208-7215. doi:10.1021/acsnano.6b03700

62. Liu M, Verma SD, Zhang Z, Sung J, Rao A. Nonequilibrium Carrier Transport in Quantum Dot Heterostructures. *Nano Lett*. 2021;21(21):8945-8951. doi:10.1021/acs.nanolett.1c01892

63. Utterback JK, Sood A, Coropceanu I, et al. Nanoscale Disorder Generates Subdiffusive Heat Transport in Self-Assembled Nanocrystal Films. *Nano Lett*. 2021;21(8):3540-3547. doi:10.1021/acs.nanolett.1c00413

64. Ong WL, Majumdar S, Malen JA, McGaughey AJH. Coupling of Organic and Inorganic Vibrational States and Their Thermal Transport in Nanocrystal Arrays. *J Phys Chem C*. 2014;118(14):7288-7295. doi:10.1021/jp4120157

65. Hasselman DPH, Johnson LF. Effective Thermal Conductivity of Composites with Interfacial Thermal Barrier Resistance. *J Compos Mater*. 1987;21(6):508-515. doi:10.1177/002199838702100602

66. Seitz M, Meléndez M, Alcázar-Cano N, Congreve DN, Delgado-Buscalioni R, Prins F. Mapping the Trap-State Landscape in 2D Metal-Halide Perovskites Using Transient Photoluminescence Microscopy. *Adv Opt Mater*. 2021;9(18):2001875. doi:10.1002/adom.202001875

67. Baxter JM, Koay CS, Xu D, et al. Coexistence of Incoherent and Ultrafast Coherent Exciton Transport in a Two-Dimensional Superatomic Semiconductor. *J Phys Chem Lett*. 2023;14(45):10249-10256. doi:10.1021/acs.jpclett.3c02286

68. Ko K, Jang M, Kwon J, Suh J. Native point defects in 2D transition metal dichalcogenides: A perspective bridging intrinsic physical properties and device applications. *J Appl Phys*. 2024;135(10):100901. doi:10.1063/5.0185604

69. Hsu WT, Lu LS, Wang D, et al. Evidence of indirect gap in monolayer WSe2. *Nat Commun*. 2017;8(1):929. doi:10.1038/s41467-017-01012-6

70. Conley HJ, Wang B, Ziegler JI, Haglund RFJr, Pantelides ST, Bolotin KI. Bandgap Engineering of Strained Monolayer and Bilayer MoS2. *Nano Lett*. 2013;13(8):3626-3630. doi:10.1021/nl4014748

71. Mastrippolito D, Cavallo M, Borowski D, et al. Operando Photoemission Imaging of the Energy Landscape from a 2D Material-Based Field-Effect Transistor. *ACS Nano*. 2025;19(9):9241-9249. doi:10.1021/acsnano.5c00256

72. Castellanos-Gomez A, Buscema M, Molenaar R, et al. Deterministic transfer of two-dimensional materials by all-dry viscoelastic stamping. *2D Mater*. 2014;1(1):011002. doi:10.1088/2053-1583/1/1/011002

73. Sun Y, Wang D, Shuai Z. Indirect-to-Direct Band Gap Crossover in Few-Layer Transition Metal Dichalcogenides: A Theoretical Prediction. *J Phys Chem C*. 2016;120(38):21866-21870. doi:10.1021/acs.jpcc.6b08748

74. Niu Y, Gonzalez-Abad S, Frisenda R, et al. Thickness-Dependent Differential Reflectance Spectra of Monolayer and Few-Layer MoS2, MoSe2, WS2 and WSe2. *Nanomaterials*. 2018;8(9):725. doi:10.3390/nano8090725

75. Mennel L, Smejkal V, Linhart L, Burgdörfer J, Libisch F, Mueller T. Band Nesting in Two-Dimensional Crystals: An Exceptionally Sensitive Probe of Strain. *Nano Lett*. 2020;20(6):4242-4248. doi:10.1021/acs.nanolett.0c00694

76. Yu Y, Yu Y, Xu C, Barrette A, Gundogdu K, Cao L. Fundamental limits of exciton-exciton annihilation for light emission in transition metal dichalcogenide monolayers. *Phys Rev B*. 2016;93(20):201111. doi:10.1103/PhysRevB.93.201111

77. Ye F, Liu Q, Xu B, Feng PXL, Zhang X. Ultra-High Interfacial Thermal Conductance via Double hBN Encapsulation for Efficient Thermal Management of 2D Electronics. *Small*. 2023;19(12):2205726. doi:10.1002/smll.202205726

78. Easy E, Gao Y, Wang Y, et al. Experimental and Computational Investigation of Layer-Dependent Thermal Conductivities and Interfacial Thermal Conductance of One- to Three-Layer WSe2. *ACS Appl Mater Interfaces*. 2021;13(11):13063-13071. doi:10.1021/acsami.0c21045

79. Karak S, Paul S, Negi D, et al. Hexagonal Boron Nitride–Graphene Heterostructures with Enhanced Interfacial Thermal Conductance for Thermal Management Applications. *ACS Appl Nano Mater*. 2021;4(2):1951-1958. doi:10.1021/acsanm.0c03303

80. Hunter N, Azam N, Zobeiri H, Wang R, Mahjouri-Samani M, Wang X. Interfacial Thermal Conductance between Monolayer WSe2 and SiO2 under Consideration of Radiative Electron–Hole Recombination. *ACS Appl Mater Interfaces*. 2020;12(45):51069-51081. doi:10.1021/acsami.0c14990

81. Zhou WX, Chen KQ. First-Principles Determination of Ultralow Thermal Conductivity of monolayer WSe2. *Sci Rep*. 2015;5(1):15070. doi:10.1038/srep15070

82. cui-et-al-2014-transient-absorption-microscopy-of-monolayer-and-bulk-wse2.

83. Gauriot N, Ashoka A, Lim J, See ST, Sung J, Rao A. Direct Imaging of Carrier Funneling in a Dielectric Engineered 2D Semiconductor. *ACS Nano*. 2023;18(1):264-271. doi:10.1021/acsnano.3c05957